Site-Specific Modeling of Indoor Radio Wave Propagation

By

Ying Wang

A thesis
presented to the University of Waterloo
in fulfillment of the thesis requirement for
the degree of
Doctor of Philosophy
in
Electrical and Computer Engineering

Waterloo, Ontario, Canada, 2000

The University of Waterloo requires the signatures of all persons using or photocopying this thesis. Please sign below and give your address and date.

Abstract

Accurate characterization of the indoor radio propagation channel is an important requirement for the effective design, assessment, and installation of a radio network inside buildings. The thesis is concerned with the development of a cost-effective site-specific simulation tool of indoor radio propagation.

First a refined 3D ray tracing model is developed in this thesis, which is based on more accurate electromagnetic theories and incorporates polarization characteristics and antenna effects. Next, we propose the hybrid technique based on combining ray tracing method with FDTD method, which uses ray tracing to analyze wide areas and FDTD to treat areas close to complex discontinuities, where ray based solutions are not sufficiently accurate. Besides much improved accuracy, the hybrid method only applies FDTD to a small portion of the entire modeling environment, which ensures practicality in terms of computational resources. The proposed hybrid method enables the study of effects of generic indoor structural features, furniture, inhomogeneity inside walls, and any objects that may have significant effect on signal coverage and statistics inside buildings. Furthermore, the thesis provides solution to the problem of outdoor-indoor signal coupling in the presence of inhomogeneous walls by using the ray tracing — FDTD — ray tracing approach. The method makes it possible to study the effect of inhomogeneity inside walls more accurately without adding much to computational complexity, especially when the incident waves can be approximated to be plane waves and the wall structure is periodic. Examples are used to show that in the areas where the specular signal is blocked by metallic structures, the proposed method can accurately predicted signal coverage by taking into account the fields scattered by the inhomogeneity inside walls while the ray tracing method is not satisfactory. The ability of the developed method to analyze fading in signal strength, Doppler spread and time dispersion caused by multipath is also demonstrated in this thesis.

Acknowledgements

I would like to express my sincere gratitude and appreciation to my supervisors, Professor Sujeet K. Chaudhuri and Professor Safieddin Safavi-Naeini. Their continuous guidance, support and inspiration during my study have made this work possible.

I would also like to thank Hewlett-Packard for offering the measurement equipment and assistance in the experiments. Appreciation also goes to Mr. Ed Spike for making the antennas for the measurements.

I acknowledge the Ministry of Education and Training of Ontario and the Faculty of Engineering of the University of Waterloo for financially supporting me through the course of this study.

Last but not least, I would like to thank my husband, Yang Ling, and my parents, Wenbo Wang and Fengzhen Li, for giving me their love, support, and encouragement all the time.

Table of Contents

List of Figures

List of Tables

Chapter 1

Introduction

With the advent of Personal Communication Systems (PCS), there is a great deal of interest in characterizing indoor radio propagation. The indoor communication environment is very complicated because of the existence of walls, ceilings and other objects, that block direct path of wave propagation between transmitter and receiver. Due to reflection, refraction and scattering of radio wave, signal power is typically carried from the transmitter to the receiver by a multiplicity of paths. The received signal is a combination of signal components arriving through different paths. Strength of each multipath component depends on the attenuation caused by passage of the signal through, or reflection of the signal by, various objects and structures in the path. Thus, the channel characteristics depend largely on the operating environment. Whether a proposed communication technique is feasible is determined by the particular characteristics in a given operating environment. A reliable channel model should be able to accurately simulate the effects of typical indoor objects and structural features on the channel characteristics.

Accurate and detailed characterization of the radio propagation channel is one of the most important requirements for the effective design, assessment, and installation of a

radio network. It enables the designer or user of a wireless system to predict signal coverage, to determine the optimum location for installation of antennas, to analyze the interference between different systems, and to predict the performance of a system.

The objective of this Ph.D. research work is to develop a cost-effective site-specific simulation technique for the indoor radio propagation. Radio channel characterization obtained from the resulting simulation tool could be used as an aid for the design of wireless local area networks (LAN) or PCS inside buildings.

1.1 Literature Review

Researchers have developed a variety of experimentally or theoretically based models to predict radio propagation in various frequency bands, and for various types of environments. Generally, we may categorize these models into two types: statistical models [Has93][Pah95][Rap96] and deterministic models [Sch92][Yan93][Sei94][Per96] [Che97][Tar97][Yan98][Wan98a][Wan98b][Wan00a]. The approach studied in this thesis falls into the deterministic category. To provide the proper perspective and a comprehensive background for the thesis, recent work on indoor channel modeling using both deterministic models and statistical models will be described in this section.

1.1.1 Statistical model

Much work has been done to statistically characterize multipath propagation inside buildings, which is based on actual measurement in specific buildings. Statistical models have the advantage of being computationally efficient for the complicated environment encountered in indoor communication. They are much less demanding of computational power than the deterministic models.

The most commonly used statistical models for indoor radio propagation are the time-domain statistical modals. Originally suggested by Turin [Tur72] for modeling urban radio channels, these models assume that the channel is a linear filter with the impulse response given by:

$$h(t,\tau) = \sum_{k=0}^{N(\tau)-1} a_k(t)\delta[\tau - \tau_k(t)]e^{j\theta_k(t)}$$

where t and τ are the observation time and application time of the impulse, N is the number of multipath components and δ is the delta function. a_k and θ_k represent the amplitude and phase of the kth path arriving at delay τ_k. Based on analysis of measurement data, these models provide statistics for the amplitudes, delays, and phases of the arrival paths, respectively. Therefore it can involve a substantial effort to collect accurate database for different environments of interest. Extensive body of literature exists on measurement efforts and application of the impulse response approach in the indoor channel modeling. [Has93] gives a summary of different distributions of path amplitude, arrival time sequence and path phases reported by different investigators. As pointed out by Hashemi, there are a number of uninvestigated issues and inconclusive points. As an example, distribution of signal amplitude is still not conclusive. Different experimenters have arrived at different distributions.

At a macroscopic level, the indoor channel can be characterized using the large-scale path loss prediction models, which are often intended for prediction of signal coverage area or finding the optimum location for antennas. The most commonly used model is the log-distance model, in which the path loss PL is represented by

$$PL(d) = PL(d_0) + 10n\log(\frac{d}{d_0}) + X_\sigma$$

in dB when the separation distance between the transmitter and receiver is d. Typically, d_0 is chosen to be 1m for indoor channel. X_σ represents a random variable that follows a normal distribution with zero mean and standard deviation σ dB. n is called the path loss exponent, which equals 2 in free space. In the complicated indoor environment, n depends on the surroundings and building type and is usually determined empirically. After extensive measurement in different buildings, a number of researchers have reported their values of n, which ranges from less than 2 to 6. A list of typical values for different type of buildings can be found in [Rap96]. However, the dependence on the environment is not well established and the standard deviation σ is usually quite large. Reported standard deviations vary from 3 dB up to 14 dB.

On the whole, based on the measurement results and statistical analysis, we can have some general ideas about indoor channel character. However, buildings are different in size, shape, and in types of construction materials. Parameters in statistical models vary greatly from building to building. One can only make general conclusions related to the building type basing on measurements, which are usually costly and time-consuming. Furthermore, statistical modals cannot relate propagation characteristics to the exact locations of the transmitter and receiver. It is desirable to have more reliable, site-specific channel models, which is only feasible with deterministic radio propagation modeling approaches in which radio propagation is related to the physical layout of the building.

1.1.2 Deterministic models

In the deterministic modeling category, there are both relatively simple solution by ray tracing method, and numerical analysis methods, such as finite-difference time-domain (FDTD) method.

(1) Ray tracing Method

Based on a simplified layout of a building, the ray tracing algorithm provides a relatively simple approximate solution to indoor radio propagation. The paths between the transmitter and the receiver are determined through transmission, reflection, and diffraction mechanisms. The method has proven to be particularly suitable for modeling of a multipath channel encountered in indoor communication. This is because ray tracing method, by its nature accommodates fading and delay of the multipath components.

There are two general approaches that can be employed to calculate these paths in ray tracing method.

The first approach uses optical images of the transmitters and receivers [Ho93] [McK91][Rus91]. Reflections of the transmitted signal by objects in the indoor environment are described by images of the transmitter. Paths to the receiver are found by using these images. Reflection point on a given object is determined by the intersection between the object and the line from the image location to the receiver. Second order reflection paths can be determined by secondary images, which are created by considering primary images as sources. Similarly, multiple reflection paths can be determined by creating images recursively. The major drawback of this method is that it is difficult to determine all image points if many reflections of the transmitted signal have to be considered. Therefore, this approach is suited to environments with only a few dominant reflectors.

The second method is the ray shooting technique [Sch92][Yan93][Sei94][Tar97] [Yan98]. This method is an intuitively simple approach to the problem of multipath propagation and it is more popular than the imaging approach described earlier. A pincushion of rays is sent out from the transmitter, and the progress of each ray is traced through the environment. Whenever a ray intersects the receiving antenna, it contributes to the total signal at the receiver.

One potential problem with this method is that it does not ensure that every signal path between the transmitter and receiver is considered. It is impossible to send out infinite number of rays, since the computation time is proportional to number of rays to be traced.

Reports by many researchers have demonstrated that ray tracing techniques are very promising for indoor radio propagation modeling. However, there are numerous unresolved problems.

First, existing simulation tools are usually based on over-simplified propagation mechanisms. Many coarse assumptions were made. Some of them do not have the ability to model the polarization characteristics. In [Sei94], it is assumed that rays that hit the floor or ceiling are TM rays and those that hit the vertical walls are TE rays and all walls are assumed to have the same dielectric constant and loss tangent regardless of material. A transmission loss of 2 dB is assumed for each object and for any ray incidence angles in [Ho93]. Also, details of furniture and other special structural features are usually omitted. In [Che97], numerical experiments were conducted to investigate the radio wave propagation in furnished rooms. It is seen that the propagation loss in the furnished room is very different from that of the empty one.

Second, ray tracing algorithm is based on geometrical optics (GO) and usually supplemented with the uniform theory of diffraction (UTD). It is well known that GO provides good results for electrically large objects and UTD is rigorous only for perfectly conducting wedges. For complex lossy structures with finite dimensions encountered in indoor environment, ray tracing fails to predict correctly the scattered fields. In the complicated indoor communication environment, transmitting and receiving antennas are often inevitably installed close to these complex discontinuities, where no asymptotic solutions are available.

Furthermore, in existing ray tracing algorithms, indoor objects, such as walls, ceilings and floors, are usually modeled as homogeneous dielectric slabs. Only specular components of transmitted and reflected fields by walls are included due to the nature of the GO approximations. However, inhomogeneities inside the walls may have notable effect on signal coverage inside buildings. It is proven that significant amount of power can be scattered from the walls made of concrete blocks in non-specular directions because of the periodic structure created by the web and void design of individual blocks inside the wall [Hon94][Wan00b].

(2) Finite-Difference Time-Domain Method (FDTD)

Another potential candidate for deterministic channel modeling is direct numerical solution of the Maxwell equations. In particular, the FDTD method has been explored by some researchers in the field of indoor radio propagation modeling. FDTD method has been employed in a wide range of electromagnetic propagation modeling studies [Uma82] [Tay69] [Chu91]. By directly solving Maxwell's equations in the time domain, the method fully accounts for the effects of reflection, diffraction and radiation. The medium constitutive relation is automatically incorporated into the solution of Maxwell's equations by using the FDTD method. Therefore, it is well suited to study wave interactions in complex media. The advantages of the FDTD method are its accuracy and that it simultaneously provides a complete solution for all points in the map, which can provide signal coverage information throughout a given area.

However, as a numerical analysis method, FDTD model requires large amounts of memory to keep track of the solution at all locations and for extensive calculations to update the solution at successive instants of time. With today's computational capabilities, it is generally unwieldy to do three-dimensional FDTD simulations for typical indoor areas, which have dimensions on the order of meters, with carrier frequencies around 1 GHz. As will be shown in this thesis, application of accurate numerical analysis method

to the entire modeling area is neither practical because of the computational resource required, nor is it necessary for open areas without many indoor objects.

To the best of the author's knowledge, only limited numbers of reports exist on results of the indoor radio channel modeling using the FDTD method [Pah95][Lee98]. In [Pah95], a 2D simulation for a 12m × 16m area shows good agreement with the measurements. In stead of applying FDTD to the whole scenario, some researchers use FDTD to calculate diffraction coefficient of non-conducting edges [Str97][Wan99] or reflection and transmission coefficients of reinforced concrete walls [Dal99].

1.2 Problem Definition and Proposed Approaches

Accurate site-specific characterization of indoor radio channel is needed to satisfy the requirement of the design of wireless communication systems inside buildings. Channel models found in literature are usually based on simplified radio propagation theories. And drawbacks in the conventional methods make it impossible to study effects of structural details. In contrast to these existing channel models, we propose a deterministic model with full propagation parameters for indoor radio propagation.

First, a refined 3D ray tracing model is developed, which is based on more accurate electromagnetic theories and incorporates polarization characteristics and antenna effects. Also, modified UTD is used to treat non-PEC wedge diffraction more accurately.

Next, we propose the hybrid technique based on combining ray tracing method with FDTD method for more accurate modeling of radio wave propagation. The basic idea is to use ray tracing to analyze wide areas and FDTD to study areas close to complex discontinuities, where ray based solutions are not sufficiently accurate. In the proposed approach, the small area is bounded by a virtual box. Rays intersecting with the boundaries of the box will act as source excitation and propagate into the volume

enclosed in the box by the FDTD propagator. We can then study effects of structural details encountered in indoor environment on the channel characteristics. Besides much improved accuracy, the hybrid method only applies FDTD to a small portion of the entire modeling environment, which ensures the practicality in terms of computational resources. Within the FDTD computation domain, field intensity and phase at all points are obtained, which facilitates the study of both path loss caused by the studied structure and probability distributions of the field envelop.

The proposed hybrid method is then extended to study the case of wave penetration through inhomogeneous walls, which is crucial in the outdoor-indoor coupling and inter-floor coupling studies. It will be shown that using the knowledge of tangential electric and magnetic field distributions along the borders of FDTD computation domain, higher order rays can be sent out to cover the rest of the environment so that prediction of signal coverage can be made more efficiently without compromising accuracy. Significant difference in predicted signal coverage is observed from numerical results obtained by the proposed method and those by the ray tracing method.

1.3 Thesis Organization

The thesis consists six chapters. This chapter presented a review of related literatures, the definition of the research problem and a brief summary of the results obtained in subsequent chapters.

Implementation of the 3D ray tracing method is described in Chapter 2. Reflection, transmission and diffraction mechanisms and antenna effect involved in the ray tracing method are also presented in this chapter. Measurements are carried out in typical indoor communication environments. Comparison between results by ray tracing method and actual measurements will be shown to validate the ray model.

The novel hybrid method based on combining FDTD method with ray tracing method is described in detail in Chapter 3. The accuracy, efficiency and robustness of this method will be demonstrated by comparing numerical results with known exact solutions, results of the full wave analysis or ray model, and measurements.

In Chapter 4, extension is made to the hybrid method for the case of wave penetration through inhomogeneous walls. Numerical results will be compared with those by full wave analysis and ray tracing method.

Applications of the developed model for analyzing small-scale fading effects created by multipath: fading in signal strength, Doppler spread and time dispersion are presented in Chapter 5.

In the last chapter, Chapter 6, the thesis is summarized and suggestions on future research directions are outlined.

1.4 Summary

Our objective is to develop a reliable and efficient site-specific indoor radio channel model. The proposed method provides a tool for studying effects of complex lossy structures encountered in indoor communication environment where no asymptotic solution is available. Such effects have been neglected by most investigators. The contribution of our research effort will be to enhance the understanding of radio propagation in the complicated indoor environment. The developed model can provide information of both long-term path loss and short-term fading effect. Detailed channel characterization can be obtained from this model, which is one of the major requirements for the successful design of radio communication systems.

Chapter 2

Ray Tracing Method

The complicated environment encountered in indoor wireless communication makes it very difficult to work out exact electromagnetic field distribution for channel modeling purpose. Based on geometrical optics theory, ray tracing can provide quick approximations to the exact solutions, which enables the site-specific channel modeling. This chapter consists of implementation of 3D ray tracing process, propagation mechanisms and antenna effects to be incorporated and measurement validation of the ray model.

2.1 Ray Tracing Process

Ray shooting technique is employed in this thesis. This section presents implementation of the 3D ray tracing process. Essential issues to make the ray tracing algorithm work more efficiently will be addressed.

2.1.1 Source ray direction

In this method, the transmitter is modeled as a point source. Rays are originated from the point source and propagated in 3D space. Each ray represents discrete local plane wave of the total field and occupies a solid angle $d\Omega$. It is necessary to consider all possible angles of departure at the transmitter in order to determine all possible ray propagation paths between the transmitter and the receiver.

To keep all ray manipulation routines general, it is desirable that each ray tube occupy the same solid angle and each wavefront be an identical shape and size at a distance from the transmitter. In two-dimensional case, this can be achieved by simply dividing the azimuth angle equally. However, in three-dimensional case, the mechanics of constant angular separation of the rays are much more complicated. If we use the spherical coordinate and simply divide the elevation angle θ and azimuth angle φ equally, it is not sufficient. The reason is that as rays are launched in directions near the poles of the sphere, the angular separation between rays decreases. This problem can be solved by using the theory of geodesic domes [Sei94][Wen79]. Fig. 2.1 shows a regular icosahedron with 20 triangular faces and 12 vertices. It can be inscribed inside a unit sphere. Suppose the coordinate origin O is the sphere center. If rays are launched from origin O and through each of the 12 vertices, each ray is separated by 63 degrees from each of its five nearest neighbors.

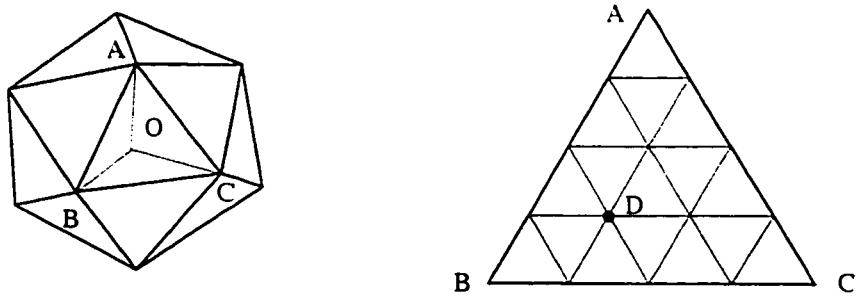

Fig. 2.1 A regular icosahedron inscribed inside a unit sphere and sides of the triangular face *ABC* are tessellated into 4 equal segments.

By using the icosahedron, wavefronts can be subdivided so that ray resolution can be increased easily. The angular resolution increase is realized by the following method. First, we use the geometrical features of an icosahedron to calculate the coordinates of the 12 vertices. Sides of each triangular face of the icosahedron are then tessellated into N equal segments, where N is the tessellation frequency [Wen79]. In Fig. 2.1, $N = 4$ is shown as an example. Lines parallel to one of the three sides of the triangle are drawn to subdivide the triangle into smaller equilateral triangles. Rays are launched at angles that pass through the vertices of these triangles. This process is realized by using vector computation. Since coordinates of A, B and C in Fig. 2.1 are all known, $\overline{AB}$ and $\overline{BC}$ are known vectors. Any vertex (e. g. D in Fig. 2.1) of the sub-triangles inside triangle ABC can be represented by

$$\overline{OD} = \overline{OB} + i \cdot \frac{\overline{AB}}{N} + j \cdot \frac{\overline{BC}}{N}$$

where $i,j = 0, 1, ..., N$. Since length of $\overline{OD}$ may not be unity, $\overline{OD}$ needs to be normalized in order to represent the direction of the source ray. This method of launching the source rays provides wavefronts that completely subdivide the surface of the unit sphere with nearly equal shape and area. If an angular separation of 1.3^0 is required, totally 16,000 rays will be sent out. Although it is easy to increase the resolution further, the computation time will also increase.

2.1.2 Tracing the rays

Starting from the source point, the algorithm follows the source ray direction and detects the closest object intersected by the ray. Once an intersection has been detected, the program generates one transmitted ray and one reflected ray that are initiated at the intersection point on the object. Amplitude and polarization of the transmitted and reflected rays are calculated using equations derived in the next section. The reflected ray

is stored and the transmitted ray is traced in a similar fashion to source rays. This continues until that the ray intensity falls below a specified threshold or the ray exits the building. Next, a previously stored reflected ray is brought out and traced in the same way until all the stored reflected ray are exhausted. The program then generates a new source ray from the transmitter. The iteration will end when all the source rays have been exhausted.

If a ray is received by the receiver, its contribution to the total field of the receiver will be recorded. Receivers are also modeled as points. Since each ray represents the field in the solid angle radiating from the transmitter, a ray is considered received if the point receiver location is within this solid angle. In order to identify received rays, a reception sphere is constructed about the receiving location with radius $r = \alpha d/\sqrt{3}$ in 3D case, where α is the angular spacing between neighboring rays at the source and d is the total path length traveled by the ray [Sei94][Sch92]. In 2D ray tracing, the radius is changed to $r = \alpha d/2$. If the program detects a ray intersection with a reception sphere, incident ray direction, electric field and receiving antenna pattern will all be considered to decide the contribute of the ray to the total field at the receiving point. Multiple receiving locations can be defined, so that electric field at each of these receiving locations can all be obtained after one run of the source ray tracing process.

In the proposed algorithm, objects are modeled as dielectric slabs with predefined thickness, boundaries, dielectric constant and loss tangent, which is appropriate for most obstacles in indoor environments. Cross-section of the slab does not have to be rectangular. It can be arbitrary polygon. Objects included in our model are walls, ceiling, floors, windows, doors and some large furniture. In order to make the computation more efficient, the building to be studies is divided into different "rooms". When the ray being traced is in a certain room, only objects inside this room need to be considered to find out the closest object intersected by the ray. And only receivers in the same room as the ray need to be detected if an intersection occurs between ray and the receiver. In this manner, one can speed up the tracing process while including more objects in each room.

The ray/sphere intersection, ray/polygon intersection and ray/box intersection algorithms described in [Gla89] are used in the intersection detection.

2.1.3 Computation Flow

The computation flow of the proposed ray tracing algorithm is shown in Fig. 2.2. Input information includes building size, objects in each room, dielectric constant and loss tangent for each object, and location and antenna type of each transmitter and receiver. Computation time depends on complexity of the building, number of source rays, or ray resolution, and ray termination threshold.

For clarity, the case of wedge diffraction is not shown in the computation flow in Fig. 2.2. Diffracting edges are also defined as objects in the input file. Input information includes position and wedge type, e.g. half plane or right-angle wedge. If a ray intersects a diffracting edge, the diffracted field contributes to all receivers that are hit by the diffracted rays. Unlike reflected and transmitted rays, diffracted rays are not traced further.

Whenever a ray intersects an object, amplitude and polarization of the transmitted, reflected or diffracted ray need to be calculated. In the following section, major radio wave propagation mechanisms in an indoor environment will be discussed. Equations of calculating transmission, reflection and diffraction coefficients will be given.

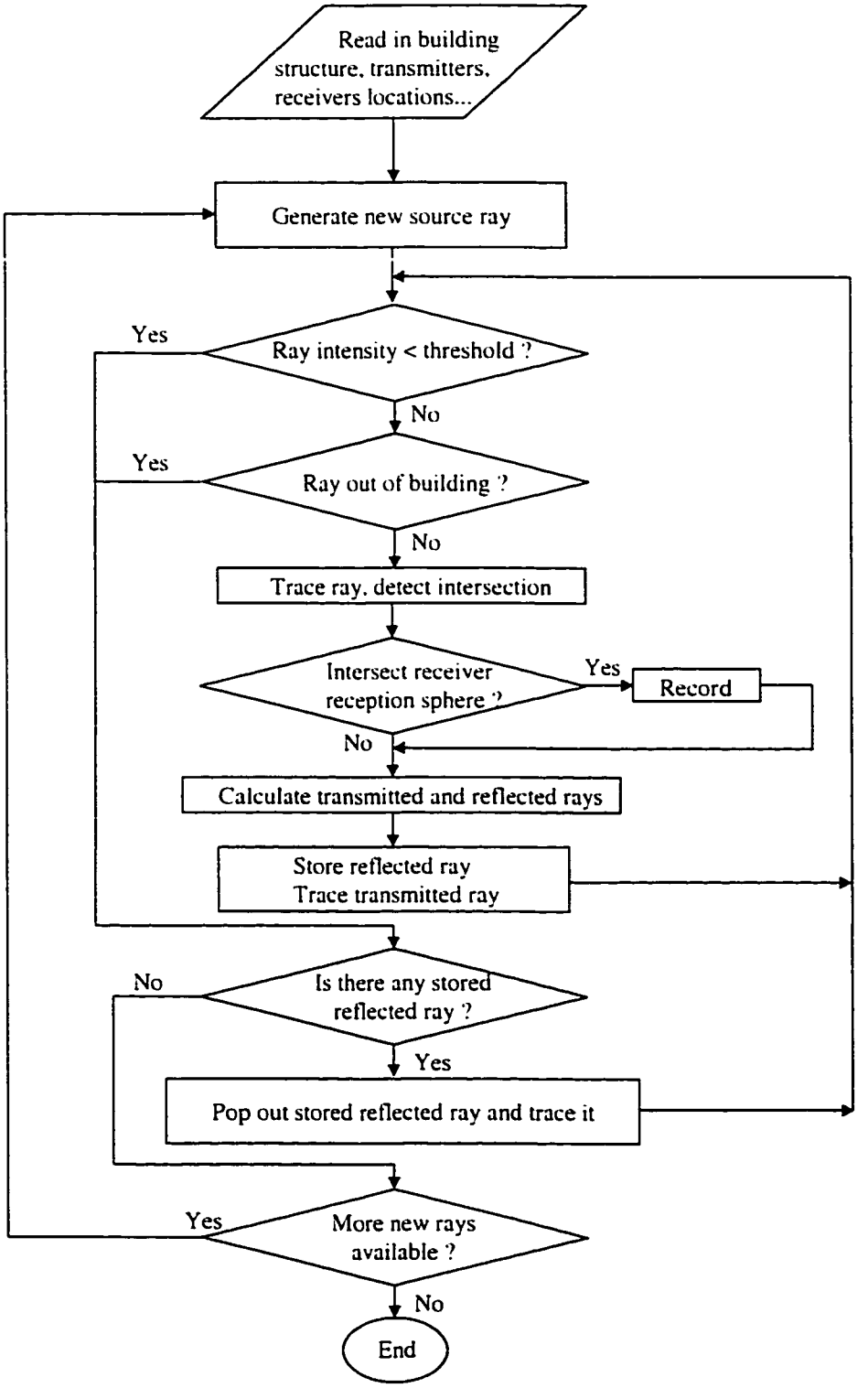

Fig. 2.2 Computation flow.

2.2 Propagation Mechanisms and Antenna Effects

A physical propagation model of an indoor radio environment consists of several mechanisms: reflection, transmission, and diffraction. In most indoor environments reflection and transmission are dominant. Diffraction contributes significantly in cases where reflected and transmitted rays through many objects are much weaker than diffracted rays.

In this section, propagation mechanisms and antenna effects to be incorporated in the ray tracing model will be discussed.

In order to include the polarization effects, the proposed method is based on the use of the electric field vectors. The vector model makes it possible to study polarization effects of transmitting and receiving antennas.

2.2.1 Reflection by and transmission through indoor objects

Once an intersection between the ray and an object is detected, the incident electric field vector of the ray is decomposed into two components: one perpendicular to the incident plane (TE wave), and the other parallel to the incident plane (TM wave). The reason lies in the fact that reflection and transmission coefficients for these two types of incident waves are different. The incident plane is defined by the incident ray and surface normal vector of the object at the point of intersection.

As shown in Fig. 2.3, objects are modeled as dielectric slab with thickness d, permittivity ε, and conductivity σ, in free space. A plane wave is incident at arbitrary angle θ_i, upon the slab. ε_0 and μ_0 are the permittivity and the permeability of free space, respectively.

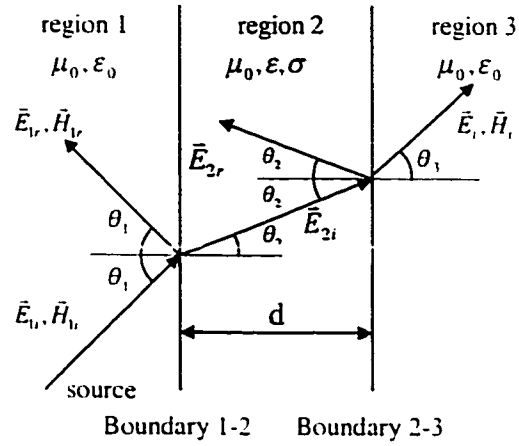

Fig. 2.3 Plane wave incident on the dielectric slab model of an object.

Reflection coefficient Γ is defined as the ratio of reflected field ($\bar{E}_{1r}$) to incident ($\bar{E}_{1i}$) field in the free space to the left of the plane boundary between region 1 and 2, i.e.

$$\Gamma = \frac{E_{1r}}{E_{1i}} \tag{2.1}$$

Transmission coefficient T is defined as the ratio of the transmitted ($\bar{E}_t$) field in the right free space region, region 3, to the incident field ($\bar{E}_{1i}$), i.e.

$$T = \frac{E_t}{E_{1i}} \tag{2.2}$$

TE wave incidence and TM wave incidence need to be considered separately. In Appendix A, derivation of the reflection coefficients and transmission coefficients for TE wave incidence and TM wave incidence is given in detail.

2.2.2 Diffraction

Besides reflection and transmission, diffraction is another important mechanism of indoor radio wave propagation. However, geometrical optics fails to account for diffracted energy in the shadow regions, and the geometric-optic field is discontinuous at shadow boundaries. A major contribution from Keller extended classical GO to include diffracted rays and geometrical theory of diffraction (GTD) [Kel62][Bha95] was originated. Later, the singularity of the field at the shadow boundaries in GTD was removed by the uniform theory of diffraction (UTD) [Kou74]. However, these diffraction coefficients are rigorously established only for perfect electrical conducting (PEC) wedges.

To allow the approximate treatment of non-PEC wedge diffraction, heuristic extensions have been made to UTD in [Lue84] for modeling path loss over hills or ridges and diffraction by loss-less thin film in [Bur83]. Individual components of the diffraction coefficient are multiplied by reflection and/or transmission coefficients of the faces of the wedge so that the total field around the wedge is continuous. There are concerns about the accuracy of diffraction coefficient for lossy dielectric wedge. Efforts toward improvement of diffraction coefficient are reported by ways of adding additional terms to UTD formula [Rou97] or by FDTD [Str97].

Our focus is on the application in indoor modeling of radio wave propagation. In indoor environment, home or office buildings, most of the structures causing diffraction can be categorized into half plane, such as soft and hard partitions, and right-angle wedge, such as wall corner. We will study the total field, including incident field, reflected field, diffracted field and/or transmitted field, in the whole space around the right-angle wedge and thick lossy dielectric half plane for both TE and TM polarizations. Results are compared to those obtained by FDTD method so as to evaluate the accuracy of the modified UTD method.

Formulation

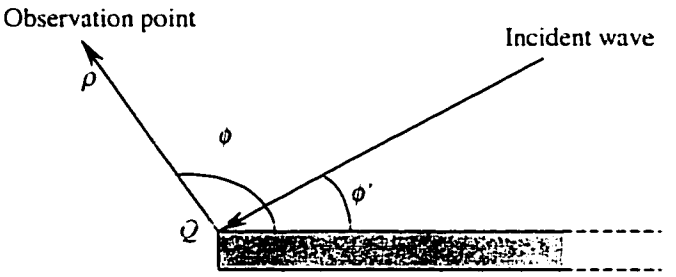

Fig. 2.4 Diffraction by thick lossy dielectric half plan (top view).

First, consider the 2D half plane diffraction as shown in Fig. 2.4, where a plane wave is incident at angle ϕ' upon the lossy dielectric half plane with finite thickness. Observations are made at a distance ρ from the point of diffraction Q. The modified diffraction coefficient is given in [Bur83] as

$$D(\phi,\phi') = (1-T)\cdot D(\phi-\phi') + R\cdot D(\phi+\phi') \tag{2.3}$$

where R and T are reflection and transmission coefficient, respectively. Equations (2.1), (2.2), (A.3) and (A.6) are used to calculate R and T. $D(\phi - \phi')$ is associated with the incident shadow boundary and the term $D(\phi + \phi')$ is associated with the reflection shadow boundary. If we assume

$$D_1 = \frac{-e^{-j\pi/4}}{2n\sqrt{2\pi k}}\cot\left[\frac{\pi+(\phi-\phi')}{2n}\right]F\left[kLa^+(\phi-\phi')\right] \tag{2.4a}$$

$$D_2 = \frac{-e^{-j\pi/4}}{2n\sqrt{2\pi k}}\cot\left[\frac{\pi-(\phi-\phi')}{2n}\right]F\left[kLa^-(\phi-\phi')\right] \tag{2.4b}$$

$$D_3 = \frac{-e^{-j\pi/4}}{2n\sqrt{2\pi k}}\cot\left[\frac{\pi-(\phi+\phi')}{2n}\right]F\left[kLa^-(\phi+\phi')\right] \tag{2.4c}$$

$$D_4 = \frac{-e^{-j\pi/4}}{2n\sqrt{2\pi k}}\cot\left[\frac{\pi+(\phi+\phi')}{2n}\right]F\left[kLa^+(\phi+\phi')\right] \tag{2.4d}$$

equation (2.3) can be written as

$$D(\phi,\phi') = (1-T)\cdot(D_1 + D_2) + R\cdot(D_3 + D_4) \tag{2.5}$$

In equation (2.4), $n = 2$, $L = \rho'\rho/(\rho'+\rho)$ for 2D with ρ' being the total distance traveled by the incident ray up to point Q, and $a^{\pm}(x) = 1+\cos(\pi-2n\pi N^{\pm})$ with N^{+} or N^{-} being a positive or negative integer or zero which most closely satisfies $2n\pi N^{\pm}-x = \pm\pi$. $F(X)$ is the Fresnel's transition function [Bal89]

$$F(X) = 2j\sqrt{X}e^{jX}\int_{\sqrt{X}}^{\infty} e^{-j\tau^2}d\tau$$

The diffraction coefficient by 2D right-angle lossy dielectric wedge, as shown in Fig. 2.5, is given by Luebbers [Lue84] and can be simplified using (2.4a)-(2.4d) to be

$$D(\phi,\phi') = (D_1 + D_2) + R_0\cdot D_3 + R_n\cdot D_4 \tag{2.6}$$

where $n = 1.5$ for the right-angle wedge and R_0 and R_n are the reflection coefficients for the 0 face, incident angle ϕ', and for the n face, reflection angle $n\pi-\phi$. The usual plane wave reflection coefficients upon finite conductivity dielectric surface [Bal89] are used in the calculation.

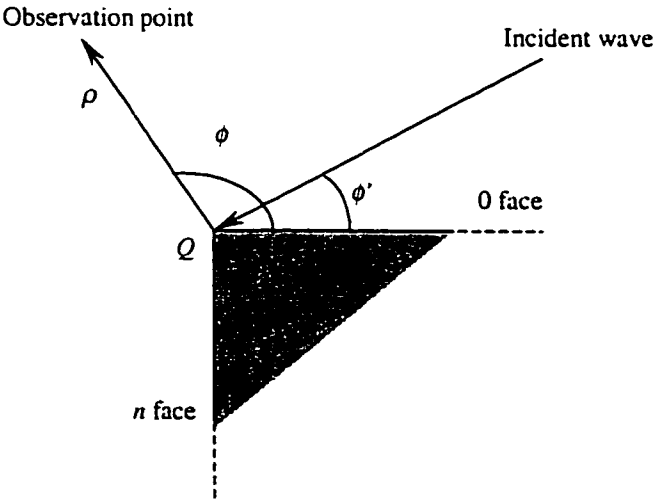

Fig. 2.5 Diffraction by right-angle lossy dielectric wedge (top view).

Equation (2.5) and (2.6) can be written into one equation as

$$D(\phi,\phi') = (1-T)(D_1 + D_2) + R_0 \cdot D_3 + R_n \cdot D_4 \tag{2.7}$$

where $T = 0$ for right-angle wedge and $R_0 = R_n = R$ for half plane so it can be easily implemented using one subroutine.

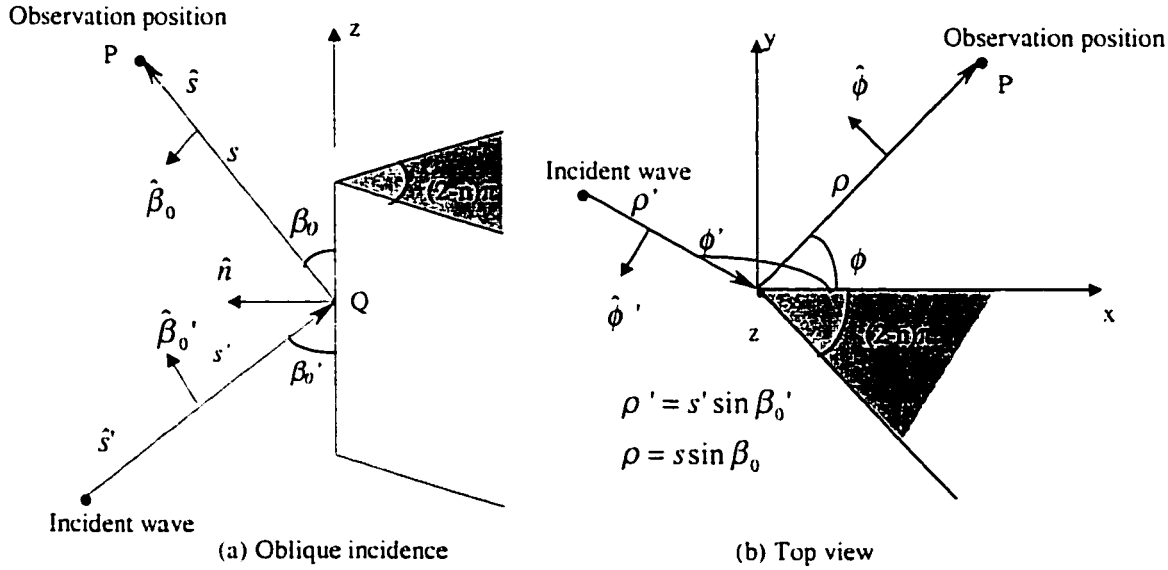

Fig. 2.6 Edge-fixed coordinate system used for 3D diffraction.

For 3D diffraction, the edge-fixed coordinate is adopted as shown in Fig. 2.6. The edge-fixed plane of incidence contains the edge vector $\hat{z}$ and direction of the incident ray $\hat{s}'$. The incident electric field at Q is decomposed into components parallel and normal to the edge-fixed plane, represented by $E_i^{\beta_0'}$ and $E_i^{\phi'}$, respectively, where $\hat{\beta}_0'$ is parallel to the plane and $\hat{\phi}'$ is normal to the plane as illustrated in Fig. 2.6. Similarly, the edge-fixed plane of diffraction contains $\hat{z}$ and direction of the diffracted ray $\hat{s}$. The reflected and transmitted fields can be decomposed into parallel and normal components: ($E_r^{\beta_0}$, E_r^{ϕ}) and ($E_t^{\beta_0}$, E_t^{ϕ}), respectively [Bur83]. Also, parallel and normal components of the

diffracted field at the observation point P are represented by $E_d^{\beta_0}(P)$ and $E_d^{\phi}(P)$. Comparing to (2.7), the 3D diffracted field can be conveniently expressed as

$$\begin{bmatrix} E_d^{\beta_0}(P) \\ E_d^{\phi}(P) \end{bmatrix} = \left(\begin{bmatrix} E_i^{\beta_0'} - E_t^{\beta_0} \\ E_i^{\phi'} - E_t^{\phi} \end{bmatrix} (D_1 + D_2) + \begin{bmatrix} E_{r_0}^{\beta_0} \\ E_{r_0}^{\phi} \end{bmatrix} D_3 + \begin{bmatrix} E_{r_n}^{\beta_0} \\ E_{r_n}^{\phi} \end{bmatrix} D_4 \right) \sqrt{\frac{s'}{s(s'+s)}} e^{-jks} \qquad (2.8)$$

Again, $E_t = 0$ for right-angle wedge and $E_{r_0} = E_{r_n} = E_r$ for half plane. The last two terms in (2.8) are the spread and phase factors of the diffracting wavefront [Bal89].

B. Numerical experiments

To calculate the total field around the half plane in Fig. 2.4, the diffracted field is obtained from the diffraction coefficient given in (2.7), and reflected and transmitted fields are computed using equations (A.3) and (A.6). In the first example studied, TE polarized plane wave is incident at an angle of 20° upon the dielectric slab with $\varepsilon_r = 3$ and $tan\delta = 0.015$. Observations are made on a circle with $\rho = 4\lambda$, where λ is the wavelength at 2.4 GHz, and $0° < \phi < 360°$. Different cases were studied when thickness of the slab was set to be $\lambda/8$, $\lambda/4$, $\lambda/2$ and λ. The total electric field is compared to the field computed using FDTD method. A good agreement between the two curves is observed even when the slab thickness is $\lambda/2$, as shown in Fig. 2.7. The coarse nature of the curve is caused by the fact that each electric field is evaluated on a node of the FDTD mesh, which divides the space into small rectangular cells. Therefore, ρ has slight fluctuation when ϕ changes.

As expected, the accuracy degrades when the slab thickness is increased to λ in Fig. 2.8. Estimated signal level with reasonable accuracy can still be obtained at most observation angles. Fig. 2.9 shows an example of TM polarized wave incident at 57° upon the same lossy dielectric slab. Thickness of the slab is $\lambda/8$.

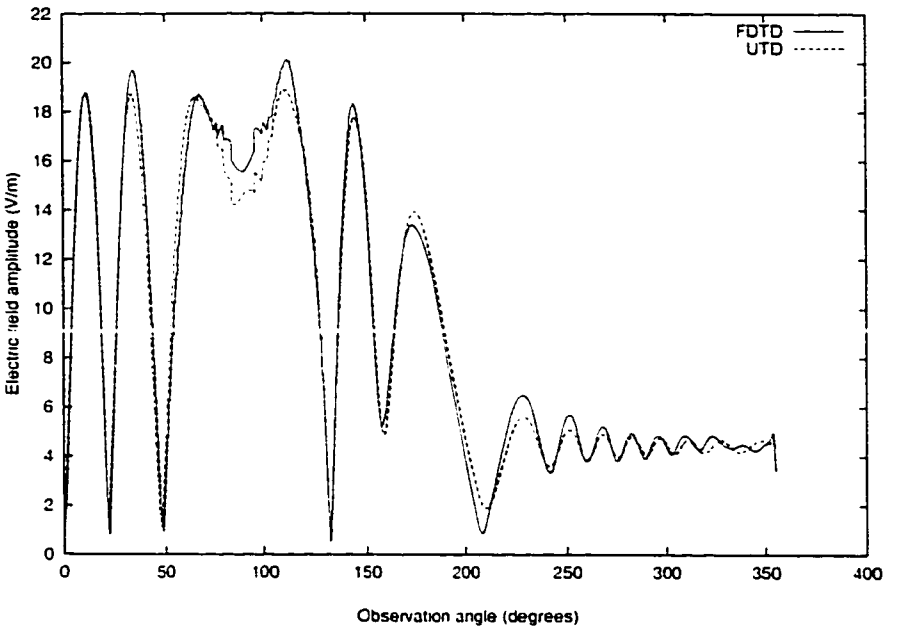

Fig. 2.7 Total electric field around the thick lossy dielectric half plane (thickness = $\lambda/2$), TE wave, $\rho = 4\lambda$, $\varepsilon_r = 3$, $tan\delta = 0.015$, $\phi' = 20°$.

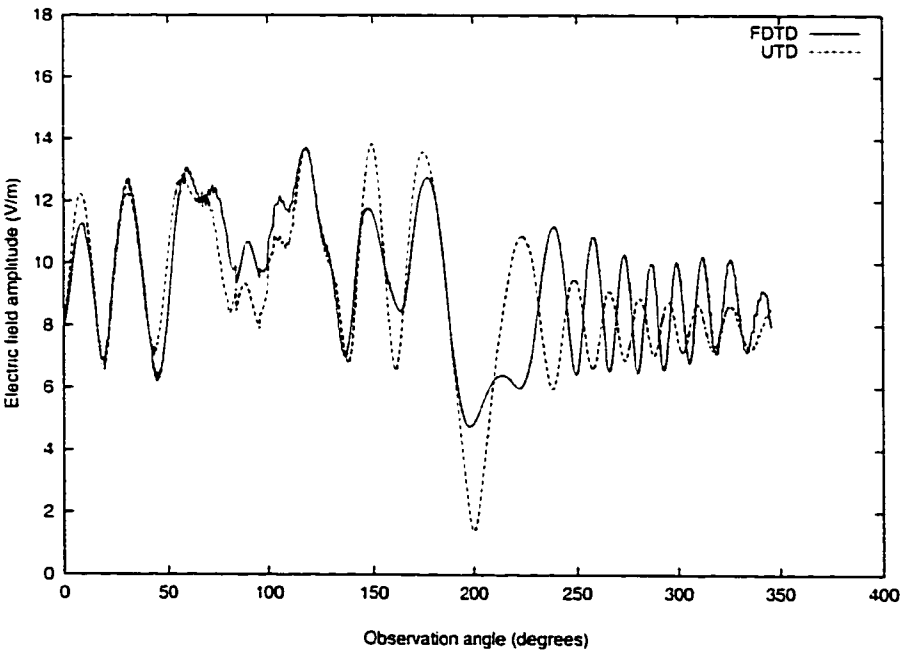

Fig. 2.8 Total electric field around the thick lossy dielectric half plane (thickness = λ), TE wave, $\rho = 4\lambda$, $\varepsilon_r = 3$, $tan\delta = 0.015$, $\phi' = 20°$.

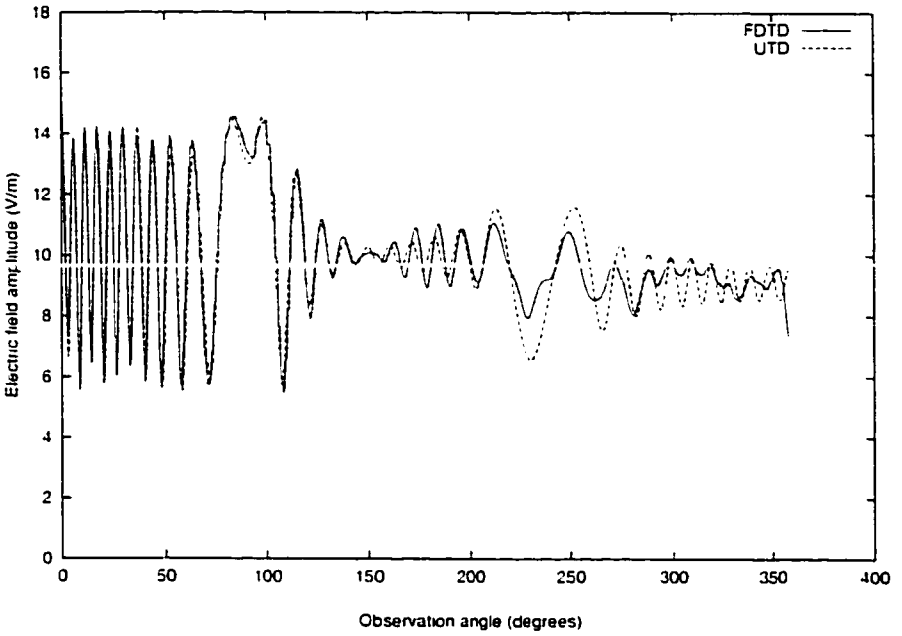

Fig. 2.9 Total electric field around the thick lossy dielectric half plane (thickness = λ/8), TM wave, $\rho = 6\lambda$, $\varepsilon_r = 3$, $tan\delta = 0.015$, $\phi' = 57°$.

For the right-angle wedge in Fig. 2.5, the diffracted field is calculated using equation (2.7). Reflected field is obtained from R_0 as mentioned earlier. In all cases studied, ε_r is assumed to be larger than 2, which is valid for most materials encountered in indoor environment. In the example shown in Fig. 2.10, TE polarized plane wave is incident at an angle of 20° upon the lossless dielectric wedge with $\varepsilon_r = 3$. The result shown in Fig. 2.11 is for TM polarization and 20° wave incident angle. The dielectric is set to have $\varepsilon_r = 3$ and $tan\delta = 0.015$. Observations are made at $\rho = 2\lambda$.

Beside the above examples, we have studied dielectrics with wide range of $tan\delta$ from lossless to PEC, different ε_r values and observation points as close as one wavelength from the diffraction points. In all cases, a good agreement between the UTD and FDTD results has been observed.

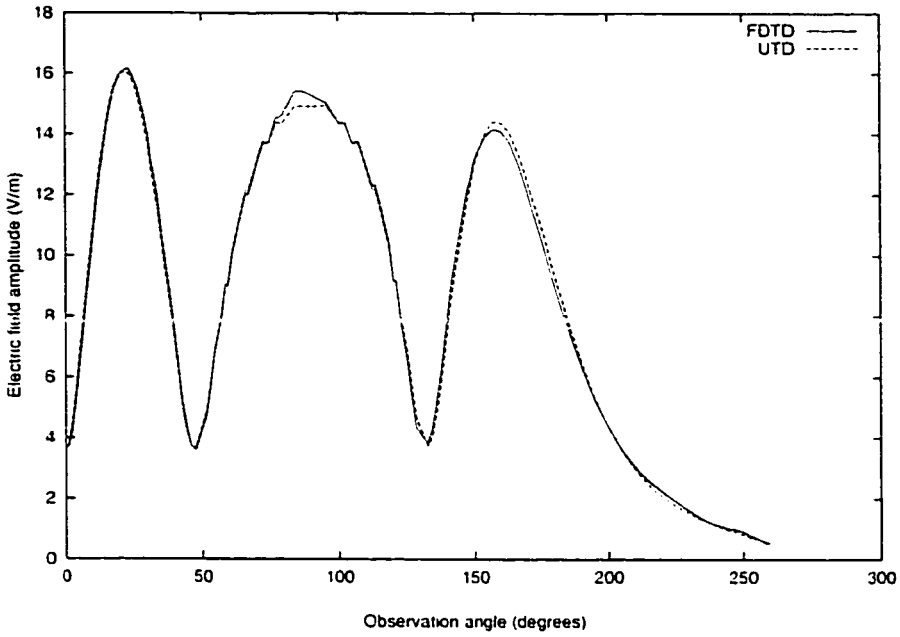

Fig. 2.10 Total electric field around the right-angle wedge.
TE wave, $\rho = 2\lambda$, $\varepsilon_r = 3$, *lossless*, $\phi' = 20°$.

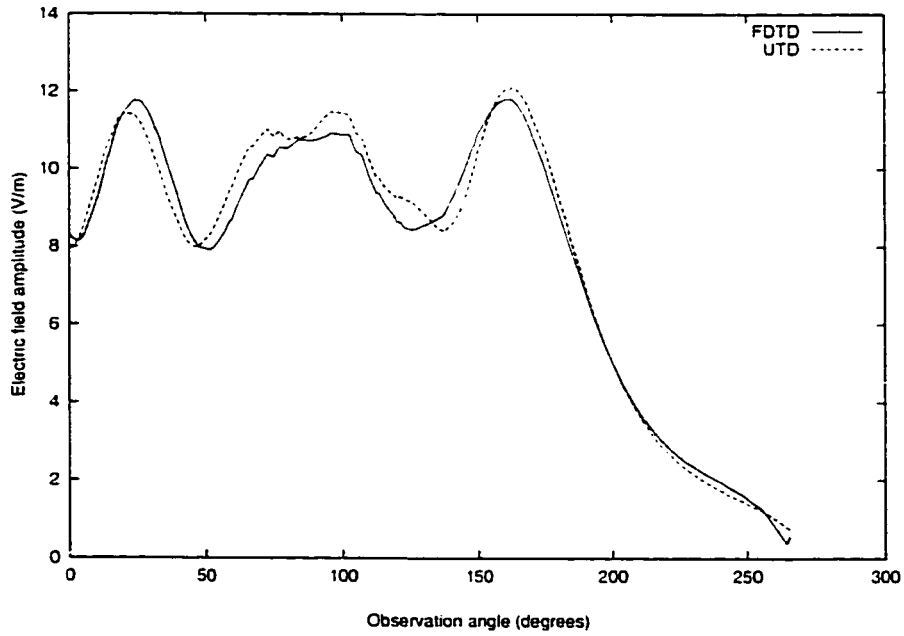

Fig. 2.11 Total electric field around the right-angle wedge.
TM wave, $\rho = 2\lambda$, $\varepsilon_r = 3$, $tan\delta = 0.015$, $\phi' = 20°$.

In light of our observations, we conclude that the modified UTD is adequate for the purpose of site-specific modeling of indoor radio wave propagation.

By using equations (2.7) or (2.8), diffraction mechanism is incorporated in our ray tracing algorithm.

2.2.3 Antenna Effects

In the ray tracing algorithm the transmitting antenna pattern is included as follows. Once the source ray is generated using the method described in section 2.1, the elevation angle θ and azimuth angle φ can be easily derived from the ray direction vector. These angles are then substituted into the antenna pattern. Take half-wave dipole antenna as an example, which has the desirable radiation pattern for indoor communication purpose. The far field electric field of a half-wave dipole in spherical coordinate system can be written as [Stu81]

$$\vec{E} = j\omega\mu \frac{2I_m}{\beta} \frac{e^{-j\beta r}}{4\pi r} \frac{\cos[(\pi/2)\cos\theta]}{\sin\theta} \hat{\theta} \tag{2.9}$$

Since the Cartesian coordinate is adopted for the ease of representing most indoor objects, equation (2.9) is transformed to

$$\vec{E} = E_x(\theta,\phi)\hat{x} + E_y(\theta,\varphi)\hat{y} + E_z(\theta,\varphi)\hat{z} \tag{2.10}$$

by using $\hat{\theta} = \hat{x}\cos\theta\cos\varphi + \hat{y}\cos\theta\sin\varphi + \hat{z}\sin\theta$. Thus the complex vector decided by (2.10) is assigned to each source ray to represent the electric field.

Upon reception of a ray with field $\bar{E}$ by the receiving antenna, the received signal strength depends on the antenna pattern and polarization mismatch between the antenna and the $\bar{E}$ field of the ray. The received signal is calculated by $\bar{G}(\theta,\varphi)\cdot\bar{E}$, where $\bar{G}(\theta,\varphi)$ is the complex polarization dependent antenna pattern of the receiving antenna.

2.3 Measurement

In order to validate the ray model, a measurement campaign is carried out in typical residential environment.

Among typical measurement systems, frequency-domain measurement using a network analyzer is the simplest method for use in small areas [Zag91][Pah89]. Such a system consists of a network analyzer with a s-parameter kit. The output of the network analyzer port 1 of the s-parameter kit is amplified and transmitted. The receiving port of the network analyzer (port 2 of the s-parameter kit) is connected to the receiving antenna. The theory of operation is that s_{21}, the ratio of the received to the transmitted voltages, as a function of the frequency is the frequency response of the channel between ports 1 and 2 of the s-parameter kit.

A portable spectrum analyzer instead of a network analyzer is used in our measurement system, which simplifies the system setup. The theory and system configuration are all similar to those of the measurement system with a network analyzer, except that the phase information can not be obtained through a spectrum analyzer.

The measurement system configuration and comparison between measurement results and ray tracing simulation results will be presented in this section.

2.3.1 Measurement system configuration

The measurement setup is composed of two parts, the transmitter and the receiver as illustrated in Fig. 2.12.

The signal generator is connected to the transmitting antenna and sends out CW signal centered at 2.4 GHz.

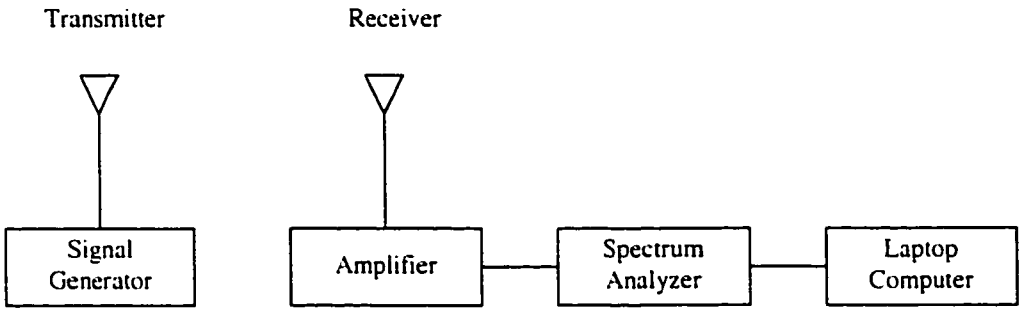

Fig. 2.12 Measurement system configuration.

In the receiver part of the system, signal received by the receiving antenna is amplified by the amplifier before it is sent to the spectrum analyzer. The spectrum analyzer is controlled by the laptop computer. The receiving system, except for the antenna, is carried on a cart, so that the receiver can be moved around easily and measure path loss at different places. The receiving antenna is supported by a tripod and connected to the amplifier by a 15 meters long cable. Therefore, the receiving antenna can be kept a distance away from the cart. Thus, we can minimize the interference of the devices with the received signal.

2.3.2 Comparison of measurement with results by ray tracing

Using the designed measurement system, measurements were made at 2.4 GHz in typical residential indoor environments. A 20 dBm CW signal was transmitted by an

antenna at a height of about 1m above the floor. The transmitter was stationary. The receiving antenna, which was also about 1m above the floor, was placed at different locations evenly spread out in the whole interested area so as to make the comparison between measurement and prediction more comprehensive. The receiving antenna was mounted on a frame that allowed it to move within a circle with radius of 2λ. At each test location, 40 measurements were made within the circle and then averaged to give the average signal strength of this receiving location. The reference signal level was measured when the receiving antenna was set up at one meter away from the transmitting antenna.

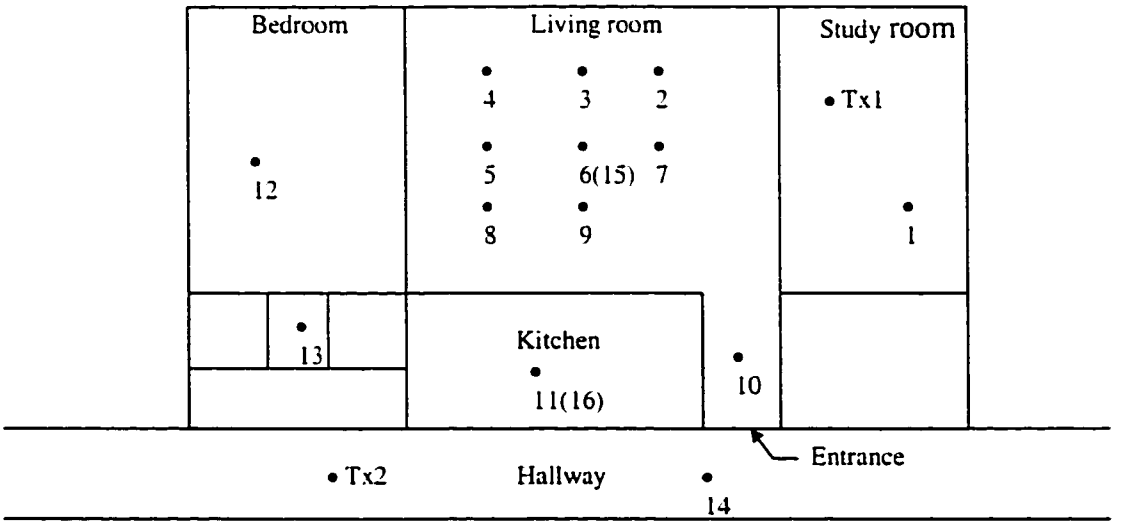

Fig. 2.13 Layout of the tested apartment.

The first measurement was made in a furnished apartment, 9m × 13m in size, as shown in Fig. 2.13. The transmitter was set at the location Tx1 in the study room and locations 1 to 13 were measured. Then the transmitter was moved from inside the apartment to the hallway as indicated by Tx2 in Fig. 2.13. Locations 14, 15, 16 were tested. Location 15 and 16 are the same as locations 6 and 11, respectively, except that locations 15 and 16 were tested when the transmitter is at location Tx2, and 6 and 11 were tested when the transmitter is at Tx1.

Simulation using the proposed 3D ray tracing was then carried out. Non-movable objects were included, such as walls, ceiling, floor, windows, doors, and closets. Because the exact building material properties are unknown, an effective dielectric constant $\varepsilon_r = 8.0$ and a loss tangent of 1.5×10^{-3} are assumed, which is reasonable according to the values given in [Hip54]. Different dielectric constant was tried between 4~12. Minor difference was found. Comparison of prediction with measured path loss is shown in Fig. 2.14, where the simulation results have been normalized to the measured reference level. A good agreement between the two sets of results is demonstrated with a root mean square (rms.) error of 3.9 dB.

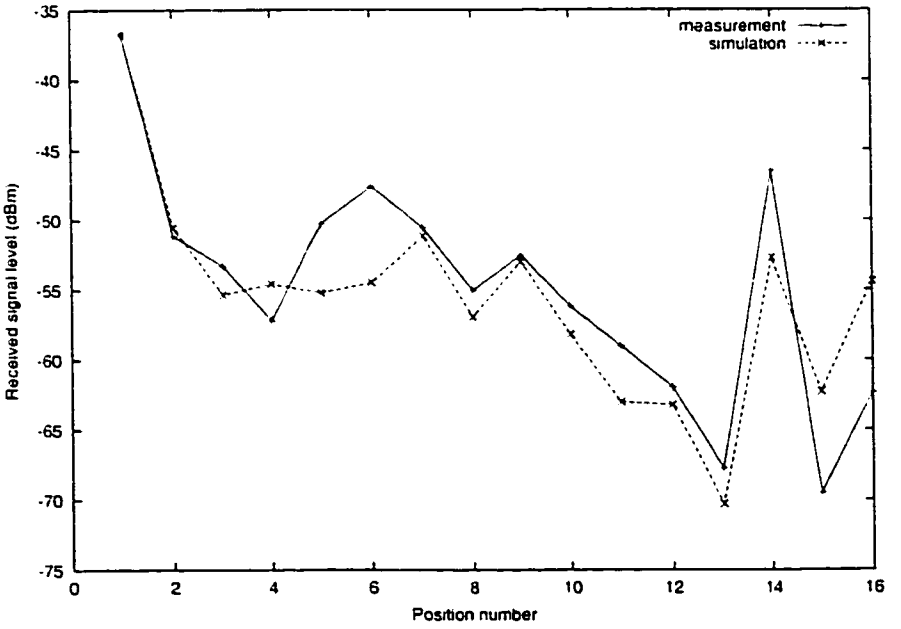

Fig. 2.14 Comparison of prediction with measured path loss in the apartment (rms. error 3.9 dB).

Next measurement was made in a two-story house with a basement and an area of 10m x 18m. Floor plans are shown in Fig. 2.15(a) ~(c), with (a) illustrating the lay out of the main floor, (b) the lay out of the second floor, and (c) the basement. Transmitter was first put in the study room on the main floor, which is indicated by Tx1 in Fig. 2.15(a). Measurements were made on the first floor and second-floor at location numbers 1~29. Then transmitter was set up on the second floor at location Tx2 in Fig. 2.15(b) and

measurements were carried out in the basement, so that the largest transmitter-receiver separation was included in our measurements.

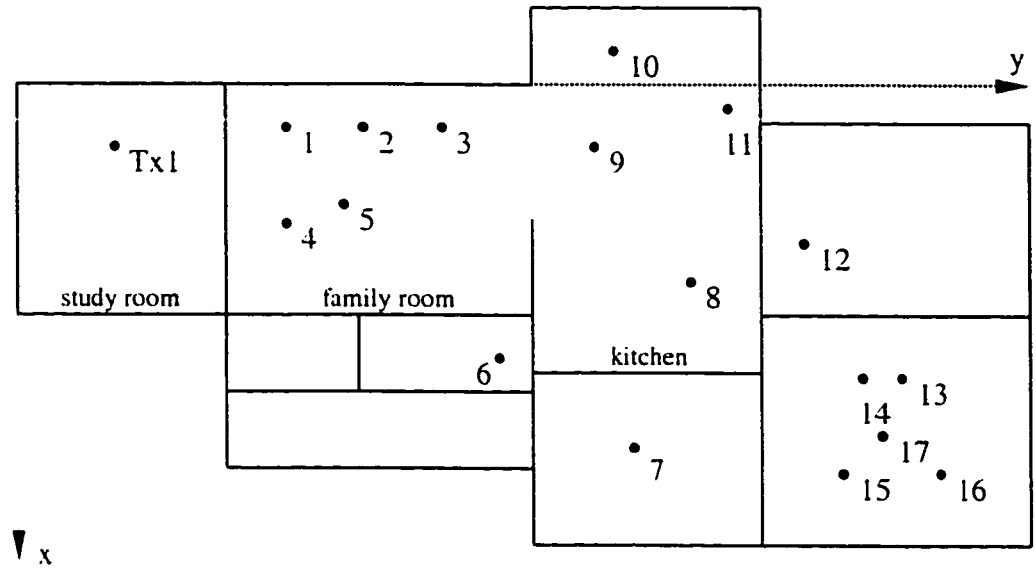

(a) Main floor

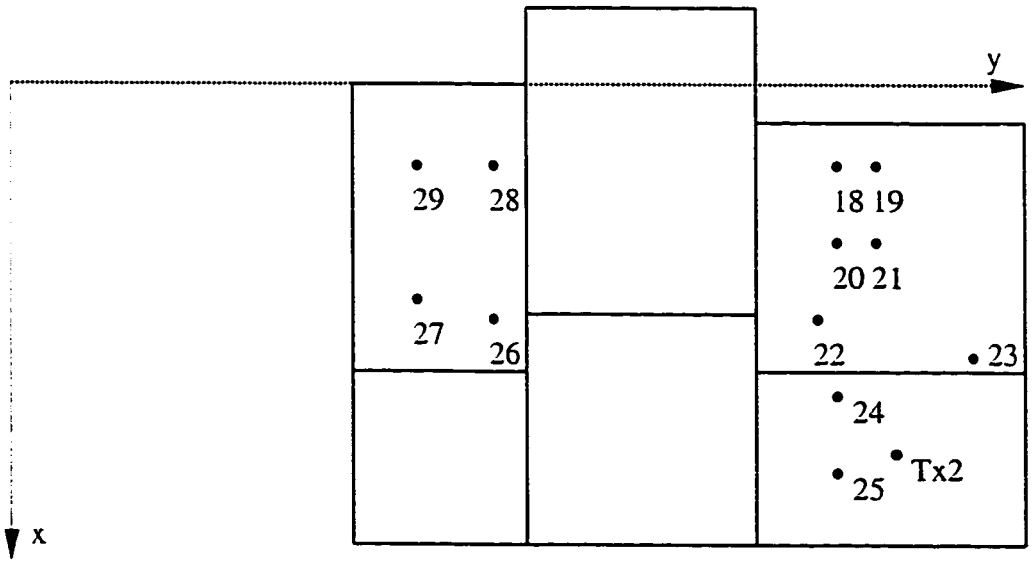

(b) Second floor

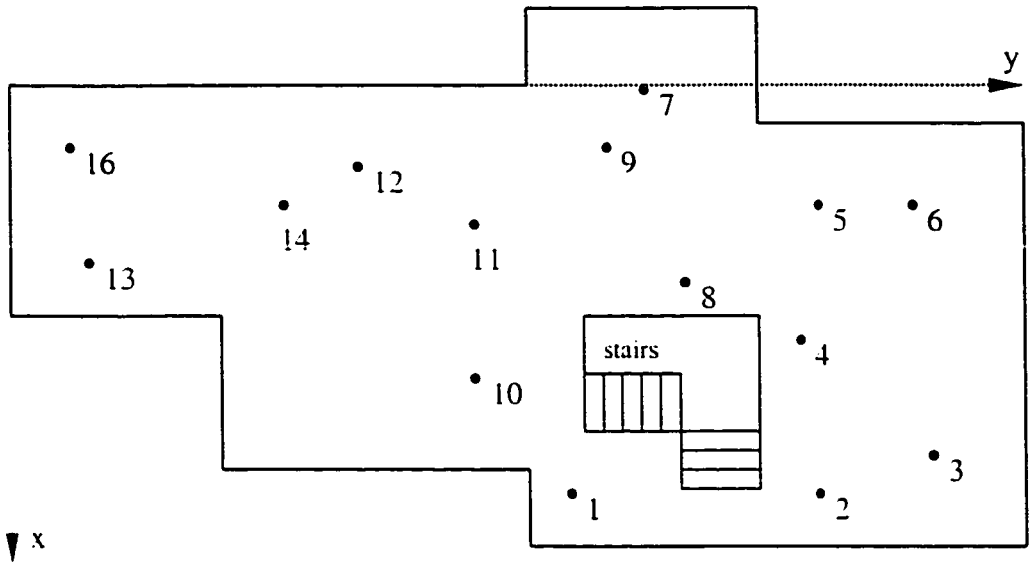

(c) Basement

Fig. 2.15 Floor plans of the tested house: (a) main floor (b) second floor (c) basement.

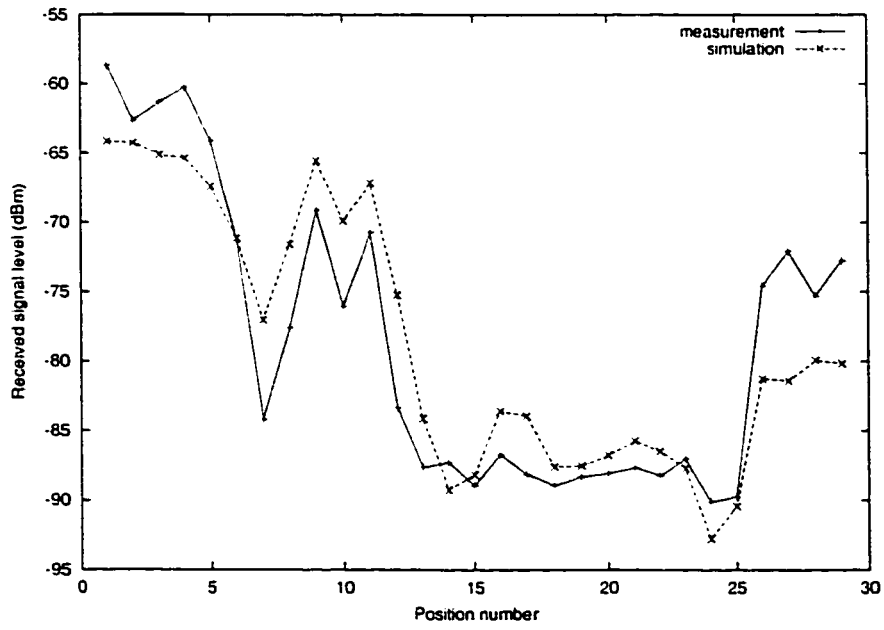

Fig. 2.16 Comparison of prediction with measured path loss in the house for transmitter location Tx1 (rms. error 4.4 dB).

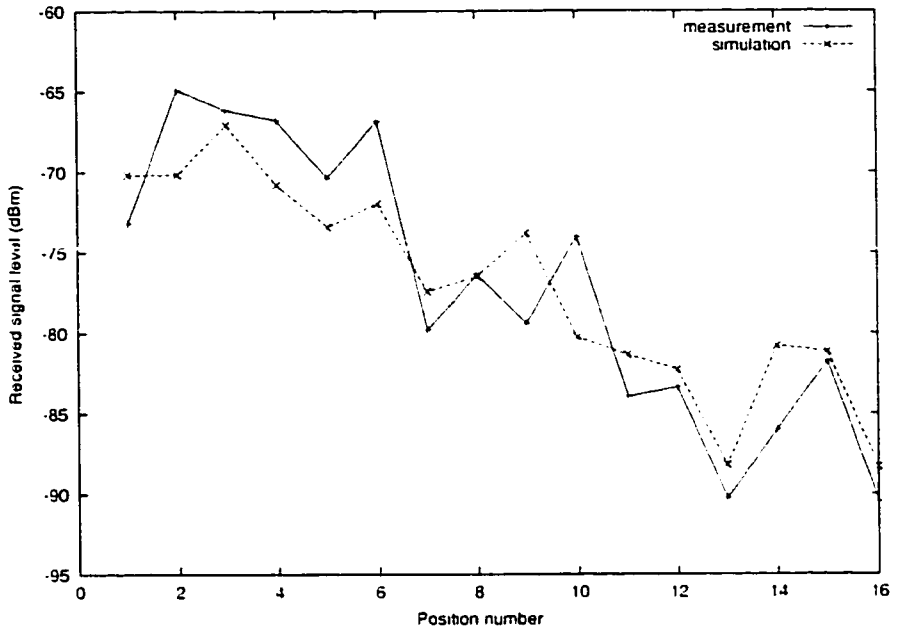

Fig. 2.17 Comparison of prediction with measured path loss in the house for transmitter location Tx2 (rms. error 3.6 dB).

In the simulation, a higher loss was assigned to the objects in the kitchen because the environment is complicated by the existing metallic objects, e.g. the stove, the refrigerator and kitchen utensils. Good conformity of the values between measurement and simulation is demonstrated in Fig. 2.16 with 4.4 dB rms. error for the first transmitter position, and in Fig. 2.17 with 3.6 dB rms. error for the second transmitter position. This is a good proof of the validity of the proposed ray tracing model.

2.4 Summary

In this chapter, we described the implementation of the 3D ray tracing algorithm and considered the main propagation mechanisms and antenna effects. A good agreement is shown between measurement results in residential indoor environment and simulation results by the ray model.

The ray tracing method is a high frequency approximation of the exact solution for electromagnetic fields, which makes the site-specific channel modeling in complicated environment possible. It can give accurate results if the size of the obstacle is much larger than a wavelength, and the observation point is many wavelengths away from the scatters. When the above assumptions are not satisfied, we will need to use other methods to solve the problem more accurately. This will be addressed in the following chapter.

Chapter 3

The Hybrid Technique – A Combination of Ray Tracing and FDTD Methods

The analysis in Chapter 2 was based on geometrical optics theory and the modified uniform theory of diffraction, which is valid when the objects are large with respect to the observing wavelength. For structures that are inhomogeneous or not smoothly curved, e.g. regions close to corners, geometrical optics fails to predict correctly the scattering properties of the body. Although these effects are usually ignored for simplicity, it is quite possible that the transmitter and/or receiver are located close to complex indoor objects. It is thus desirable to have models to study these effects. Furthermore, by comparing the results obtained by ray tracing method and those by more accurate method, we will be able to assess to what extent the ray model can provide sufficiently accurate channel prediction.

Since for most of actual indoor structural features there are no exact solutions or asymptotic solutions available, we propose the usage of numerical analysis method, specifically, the FDTD method in combination with the ray tracing method. The major effects of the discontinuities to the electromagnetic fields are local in nature [Ruc70]. Therefore FDTD method is to be applied to regions with the dimension of only a few

wavelengths surrounding these objects instead of the whole modeling area, which would ensure the practicality in terms of computational resources.

In this chapter, the hybrid method of combining ray tracing and FDTD methods is described in detail. Examples of applying the proposed method for studying indoor structures and penetration of wave from outdoor to indoor are given at 2.4 GHz. Numerical results are presented and compared with known exact solutions, or results of the full wave analysis, or ray model to demonstrate the accuracy, efficiency and robustness of our method. Numerical results are also compared with the measurement reported in [Hor86] for waves at 1.29 GHz penetrating an external wall with metal-framed windows.

3.1 Description of the FDTD Method

Before introducing the hybrid method, the FDTD method will be briefly described in this section. Based on the Maxwell's equations in its finite-difference form, the FDTD method models the propagation of an incident electromagnetic wave into a volume of space containing the structure of interest. In a source free, isotropic and linear medium, the propagation of radio wave is governed by the two Maxwell's curl equations

$$\mu \frac{\partial \bar{H}}{\partial t} = -\nabla \times \bar{E} \tag{3.1}$$

$$\varepsilon \frac{\partial \bar{E}}{\partial t} = \nabla \times \bar{H} - \sigma \bar{E} \tag{3.2}$$

where ε, μ, and σ are the permittivity, permeability and conductivity of the medium. Vector components of the curl operator in (3.1) and (3.2) can be written out to yield the following six coupled scalar equations in the Cartesian coordinate:

$$\frac{\partial H_x}{\partial t} = \frac{1}{\mu} \cdot \left(\frac{\partial E_y}{\partial z} - \frac{\partial E_z}{\partial y} \right) \tag{3.3}$$

$$\frac{\partial H_y}{\partial t} = \frac{1}{\mu} \cdot \left(\frac{\partial E_z}{\partial x} - \frac{\partial E_x}{\partial z} \right) \tag{3.4}$$

$$\frac{\partial H_z}{\partial t} = \frac{1}{\mu} \cdot \left(\frac{\partial E_x}{\partial y} - \frac{\partial E_y}{\partial x} \right) \tag{3.5}$$

$$\frac{\partial E_x}{\partial t} = \frac{1}{\varepsilon} \cdot \left(\frac{\partial H_z}{\partial y} - \frac{\partial H_y}{\partial z} - \sigma E_x \right) \tag{3.6}$$

$$\frac{\partial E_y}{\partial t} = \frac{1}{\varepsilon} \cdot \left(\frac{\partial H_x}{\partial z} - \frac{\partial H_z}{\partial x} - \sigma E_y \right) \tag{3.7}$$

$$\frac{\partial E_z}{\partial t} = \frac{1}{\varepsilon} \cdot \left(\frac{\partial H_y}{\partial x} - \frac{\partial H_x}{\partial y} - \sigma E_z \right) \tag{3.8}$$

Using Yee's Lattice [Yee66], the volume to be studied is then discretized into cells in 3D case or a mesh in 2D case. The electromagnetic parameters ε, μ, and σ of different materials are assigned to each cell according to the spatial distribution of the structure. Components of electric and magnetic field are positioned at alternate half intervals. A space point in a uniform rectangular lattice is denoted by $(i,j,k) = (i\Delta x, j\Delta y, k\Delta z)$ and any function u of space and time evaluated at a discrete point in the grid and at a discrete point in time is represented by

$$u(i\Delta x, j\Delta y, k\Delta z, n\Delta t) = u^n(i, j, k)$$

where Δx, Δy, Δz are the space increments, Δt is the time increment and i, j, k and n are integers. The space and time derivatives in the set of equations (3.3) – (3.8) are expressed in the centered difference forms, which has the advantage of being second-order accurate in the space and time increments. The difference operators for $\frac{\partial u}{\partial x}$ and $\frac{\partial u}{\partial t}$ are

$$\frac{\partial u}{\partial x} = \frac{u^n\left(i+\tfrac{1}{2},j,k\right) - u^n\left(i-\tfrac{1}{2},j,k\right)}{\Delta x} + 0\left[(\Delta x)^2\right] \tag{3.9}$$

$$\frac{\partial u}{\partial t} = \frac{u^{n+\frac{1}{2}}(i,j,k) - u^{n-\frac{1}{2}}(i,j,k)}{\Delta t} + 0\left[(\Delta t)^2\right] \tag{3.10}$$

Expressing the partial derivatives in (3.3) and (3.6) by the centered expressions of (3.9) and (3.10) results in the following finite-difference equations:

$$H_x^{n+\frac{1}{2}}(i,j,k) = H_x^{n-\frac{1}{2}}(i,j,k) + \frac{\Delta t}{\mu(i,j,k)} \cdot \left(\frac{E_y^n(i,j,k+\tfrac{1}{2}) - E_y^n(i,j,k-\tfrac{1}{2})}{\Delta z} - \frac{E_z^n(i,j+\tfrac{1}{2},k) - E_z^n(i,j-\tfrac{1}{2},k)}{\Delta y} \right)$$

$$E_x^{n+1}(i,j,k) = A(i,j,k) \cdot E_x^n(i,j,k) + B(i,j,k) \cdot \left(\frac{H_z^{n+\frac{1}{2}}(i,j+\tfrac{1}{2},k) - H_z^{n+\frac{1}{2}}(i,j-\tfrac{1}{2},k)}{\Delta y} - \frac{H_y^{n+\frac{1}{2}}(i,j,k+\tfrac{1}{2}) - H_y^{n+\frac{1}{2}}(i,j,k-\tfrac{1}{2})}{\Delta z} \right)$$

where

$$A(i,j,k) = \frac{1 - \dfrac{\sigma(i,j,k)\Delta t}{2\varepsilon(i,j,k)}}{1 + \dfrac{\sigma(i,j,k)\Delta t}{2\varepsilon(i,j,k)}}, \qquad B(i,j,k) = \frac{\dfrac{\Delta t}{\varepsilon(i,j,k)}}{1 + \dfrac{\sigma(i,j,k)\Delta t}{2\varepsilon(i,j,k)}}$$

Equations of H_y, H_z, E_y and E_z can be obtained similarly.

With these finite-difference equations, the new value of a field vector component at any space lattice point depends only on its previous value and the previous values of the components of the other field vector at adjacent points.

This fully explicit time-stepping process employed in the FDTD method for Maxwell's curl equations requires time increment Δt to have a specific bound relative to the lattice space increments Δx, Δy and Δz. This bound is necessary to avoid numerical instability, which can cause the computed results to spuriously increase or decrease without limit as time-marching continues. The stability condition referred to as the CFL stability condition [Chu91], is that in a sourceless and homogeneous medium, the following criteria must be satisfied:

$$\text{2D: } c\Delta t \le \left[\frac{1}{\Delta x^2} + \frac{1}{\Delta y^2}\right]^{-\frac{1}{2}}$$

$$\text{3D: } c\Delta t \le \left[\frac{1}{\Delta x^2} + \frac{1}{\Delta y^2} + \frac{1}{\Delta z^2}\right]^{-\frac{1}{2}}$$

where c is the wave propagation velocity in the medium.

One major issue in the FDTD method is that the computation domain must be limited in size because of the limitation of computer memory. At the outer grid boundary of the computational domain, an absorbing boundary condition is needed to simulate the extension of the grid to infinity. To this end, Mur's second order absorbing boundary condition [Mur81][Taf95] is used in this work.

3.2 Combination of Ray Tracing and FDTD Methods

In this section, a method of combining ray tracing with FDTD is presented.

First, the ray tracing method described in Chapter 2 is used to send out ray tubes from the transmitter. The progress of each ray is traced throughout the environment. The region to be studied by FDTD method is enclosed by a virtual box. It may contain inhomogeneity in construction materials, isolated objects, or any structural features that

are of interest. In the software implementation, this box is defined as an object in the input data file of ray tracing process.

Whenever a ray tube intersects the predefined virtual box, its contribution to the total incident waves along the interfaces between the ray tracing domain and FDTD domain is recorded. These incident waves are then propagated into the region of interest by the FDTD propagator to analyze wave interaction with the structure enclosed in the box. Thus, field amplitude at each point within the FDTD computation domain is obtained.

Multiple virtual boxes can be defined, so that source excitation into each enclosed region can be obtained after one execution of ray tracing. However, each region needs to be treated separately by FDTD afterwards. It is assumed that the receiving points of interest are in the enclosed regions.

As an example, Fig. 3.1 shows a 2D environment with a transmitter Tx. An area of interest is enclosed by the dashed-line rectangle $A_1B_1C_1D_1$, which contains complex inhomogeneity while the rest of the area is quite open. The four sides of the rectangle are the incident planes providing interface between the intersecting rays and the FDTD method. Some typical rays that hit the rectangle are shown in Fig. 3.1, with ray 1 representing the direct ray, ray 2 reflected ray and ray 3 diffracted ray. Inside the enclosed region, FDTD method will be used to fully account for the effects of reflection, diffraction and scattering. Objects outside this region are treated by GO and modified UTD as explained in Chapter 2. Additional virtual boxes, e.g. $A_2B_2C_2D_2$, can be defined enclosing the square-shaped object at the left bottom corner if the field surrounding the object is also of interest.

Reflected or scattered field emerging from the virtual box will interact with the outside environment. Such high-order effects can be included using ray tracing when the interested area can still support well-defined rays, such as the walls enclosed in $A_1B_1C_1D_1$ in Fig. 3.1. Ray 4 enters the enclosed area from point P_1 and reflected by a wall. If traced further, the reflected ray exits this area and after one more reflection, it re-

enters the area as ray 5 at point P_2. Both ray 4 and ray 5 can be included in the subsequent FDTD computation to incorporate high-order ray effects.

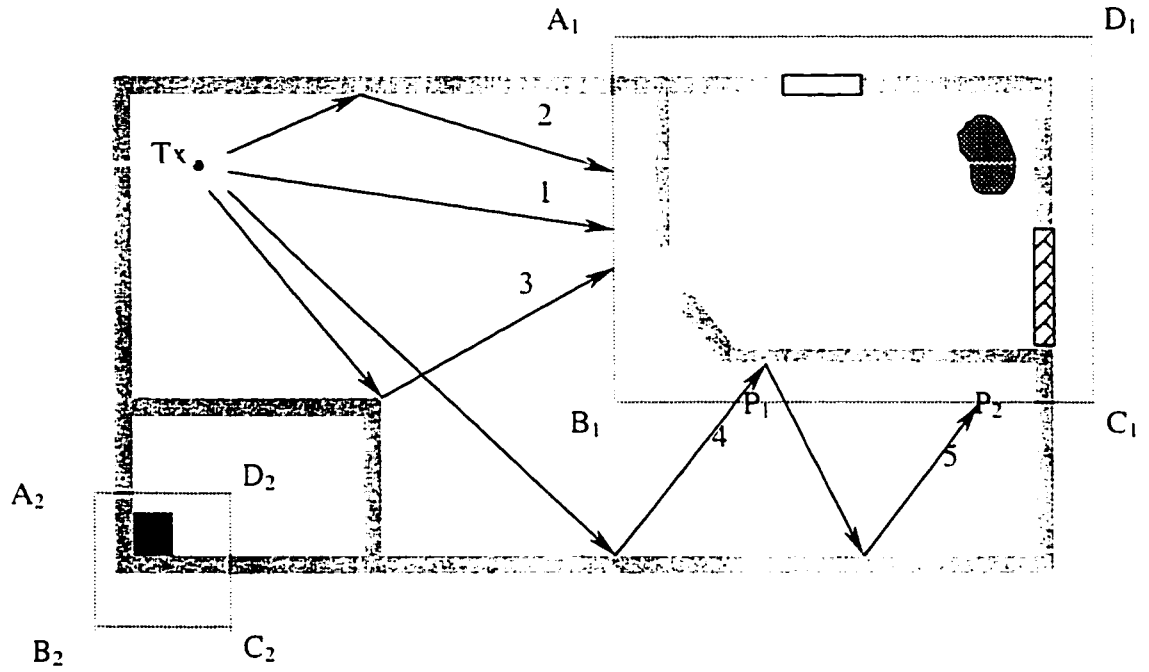

Fig. 3.1 An indoor environment with the interested areas enclosed by the virtual boxes $A_1B_1C_1D_1$ and $A_2B_2C_2D_2$. Different shades and textures are used to represent different building materials.

The rectangle $A_1B_1C_1D_1$ in Fig. 3.1 is enlarged in Fig. 3.2 to demonstrate the FDTD grid. To simplify the explanation, TM polarization, which involves three field components: E_z, H_x and H_y, is assumed in what follows. In order to generate the incident wave, we need to specify the exact field distribution on the incidence planes at each time interval. The field distribution is derived from previously stored intersecting rays. Consider node *(i, j)* $(x=i\Delta x,\ y=j\Delta y)$ in Fig. 3.2 on the incident plane A_1B_1. The distance from node *(i, j)* to each ray is evaluated. As stated in section 2.1.2, if the distance between node *(i, j)* and a ray is less than $\alpha d/\sqrt{3}$ in 3D or $\alpha d/2$ in 2D case, where α is the angular

spacing between neighboring rays at the source and d is the total path length traveled by the ray, node (i, j) is considered to be in the ray tube and the ray contributes to the total field at node (i, j). If k rays hit the node, the electric field at (i, j) becomes $\bar{E}(i,j) = \sum_{n=1}^{k} \bar{E}_n$, where $\bar{E}_n$ is the time dependent electric field of the nth ray at point (i, j). Also, adjacent nodes can be illuminated by the same ray as shown in Fig. 3.2: both node (i, j) and its adjacent nodes $(i, j-1)$ and $(i, j+1)$ can have contribution from ray tube 1.

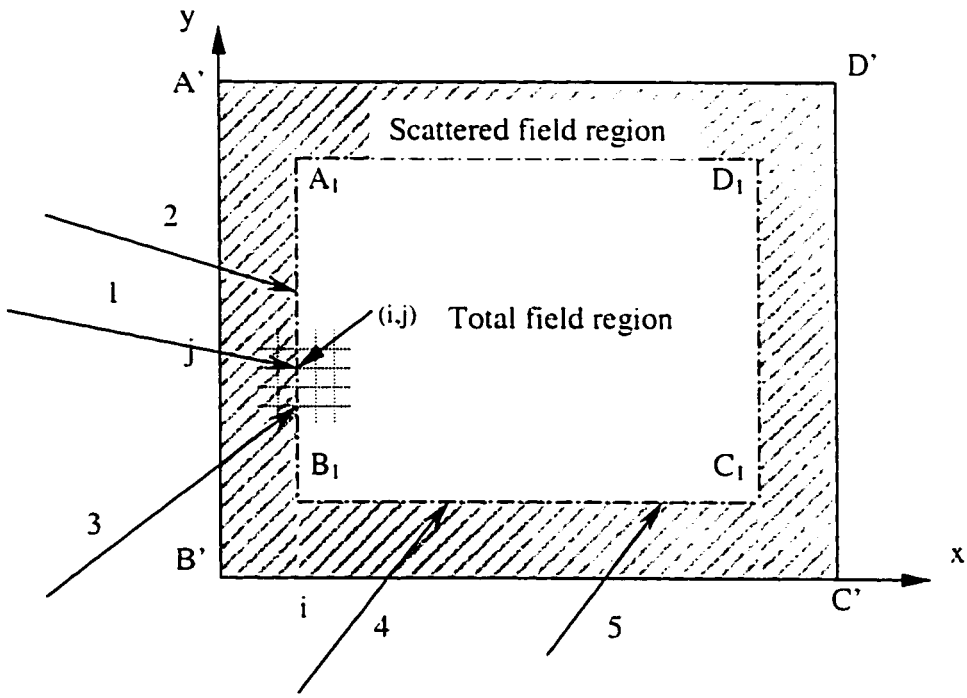

Fig. 3.2 Enlargement of the rectangle $A_1B_1C_1D_1$ in Fig. 3.1 showing the combination of ray tracing and FDTD methods.

The actual computation domain of FDTD extends to A'B'C'D', which is larger than rectangle $A_1B_1C_1D_1$, as shown in Fig. 3.2. The shaded area is the scattered-field region,

which is introduced to reduce parasitic waves generated by the source excitation method described above [Chu91]. The area inside is the total-field region. This approach is based on the decomposition of the electric and magnetic fields as

$$\vec{E}_{tot} = \vec{E}_{scat} + \vec{E}_{inc}$$

$$\vec{H}_{tot} = \vec{H}_{scat} + \vec{H}_{inc}$$

where subscriptions *tot*, *scat* and *inc* are used to denote total, scattered and incident components of electric and magnetic fields, respectively. In the scattered-field region, the algorithm only operates on scattered-field components, which implies that there is no incident wave in this region. In the total-field region, where the structure of interest is embedded, the algorithm operates on the total field. Incident wave is introduced along the interface between these two regions.

The source excitation scheme is demonstrated in Fig. 3.3, which shows field components around node *(i, j)* along incident plane A_1B_1.

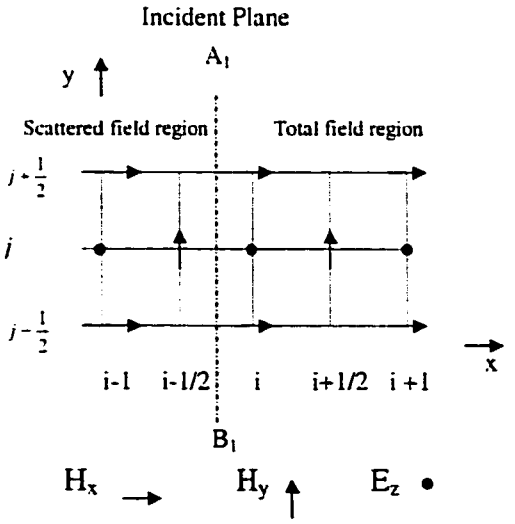

Fig. 3.3 Source excitation scheme.

The evaluation of $E_z(i, j)$ at time step $(n+1)$, denoted by $E_z^{n+1}(i, j)$, using the FDTD propagator requires knowledge of the preceding half time step values of $H_y(i-1/2, j)$, $H_y(i+1/2, j)$, $H_x(i, j-1/2)$ and $H_x(i, j+1/2)$. There is inconsistency if the FDTD propagator is applied blindly, because $E_z(i, j)$, $H_y(i+1/2, j)$, $H_x(i, j-1/2)$ and $H_x(i, j+1/2)$ are in the total field region while $H_y(i-1/2, j)$ is in the scattered field region. The correct equation for updating $E_z(i, j)$ is given by Taflove [Taf95] as

$$E_{z,tot}^{n+1}(i,j) = E_{z,tot}^{n}(i,j) + \frac{\Delta t}{\varepsilon_0 \Delta}\left[\begin{array}{l} H_{y,tot}^{n+\frac{1}{2}}(i+\frac{1}{2},j) - H_{y,scat}^{n+\frac{1}{2}}(i-\frac{1}{2},j) \\ + H_{x,tot}^{n+\frac{1}{2}}(i,j-\frac{1}{2}) - H_{x,tot}^{n+\frac{1}{2}}(i,j+\frac{1}{2}) \end{array}\right] - \frac{\Delta t}{\varepsilon_0 \Delta} H_{y,inc}^{n+\frac{1}{2}}(i-\frac{1}{2},j) \tag{3.11}$$

where $\Delta x=\Delta y=\Delta$ is assumed for simplicity and ε_0 is the permittivity of free space.. Similarly, the scatter field of H_y at node $\left(i-\frac{1}{2}, j\right)$

$$H_{y,scat}^{n+1}(i-\frac{1}{2},j) = H_{y,scat}^{n-\frac{1}{2}}(i-\frac{1}{2},j) + \frac{\Delta t}{\mu_0 \Delta}\left[E_{z,tot}^{n}(i,j) - E_{z,scat}^{n}(i-1,j)\right] - \frac{\Delta t}{\mu_0 \Delta} E_{z,inc}^{n}(i,j) \tag{3.12}$$

where μ_0 is the permeability of free space. Note that equation (3.11) and (3.12) are made consistent by adding the last term. Therefore both $E_z(i, j)$ and $H_y(i-1/2, j)$ components of the incident wave are required. With known incident ray direction and electric field, the incident magnetic fields can be readily calculated using plane wave model. Source excitations along B_1C_1, C_1D_1 and D_1A_1 are carried out in a similar manner.

After specifying the incident field distribution on the incident planes, waves are propagated into the enclosed region by the FDTD propagator. The absorbing boundary condition [Mur81] is applied to update fields at the four boundaries: A'B', B'C', C'D' and D'A' in Fig. 3.2. Thus, field distribution inside the region is obtained.

Location and size of each virtual box can be defined flexibly, depending on interest. An area enclosed in the box with a larger dimension requires more memory and CPU time. Since ray tracing treats areas outside the box, any scattering effects omitted by GO and the modified UTD can not be included in the field inside the box, which can be a cause of error. However, scattering by small inhomogeneities is usually local in nature. Therefore, the predicted field inside the box is more accurate when the box boundaries are positioned away from outside scatterers. A proper choice of the dimension and location of the virtual box requires a good understanding of wave propagation mechanisms.

Applications of the hybrid technique of combining ray tracing and FDTD methods to 2D problems will be presented in the next section. Computations are done at 2.4 GHz except for the last example, which is calculated at 1.29 GHz.

3.3 Numerical Results

3.3.1 Comparison with exact solution

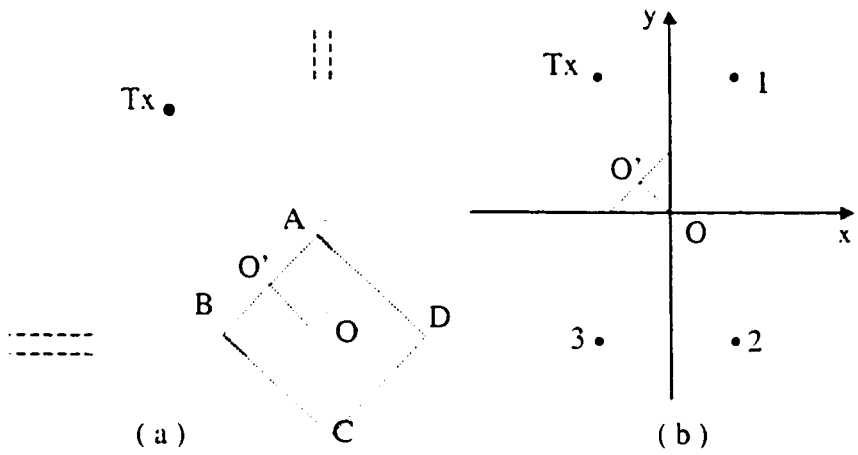

Fig. 3.4 The 2D problem of a corner formed by two half-plane electric conductors (a) An infinite electric line source located at Tx; (b) Equivalent sources.

To validate the proposed method, a 2D problem shown in Fig. 3.4(a) was studied first. It is a corner formed by two half-plane electric conductors. An electric line source is located at about 50λ from the corner, where λ is wavelength of the incident em wave. In this geometry, ray tracing treats the entire region except the vicinity of the corner. The area to be analyzed by FDTD is enclosed by the dashed-line rectangle. For such a simple structure, the exact electric field distribution can be obtained by using equivalent sources to replace the conductors [Bal89] as shown in Fig. 3.4(b). Assuming the electric line source is $\hat{z}I_e$, located at (-x, y), the equivalent source 1 is $-\hat{z}I_e$, located at (x, y), equivalent source 2 is $\hat{z}I_e$, located at (x, -y), and equivalent source 3 is $-\hat{z}I_e$, located at (-x, -y). The electric field along OO', which is 10λ long, can be conveniently derived from the four sources. Fig. 3.5 shows both the exact solution and the predicted electric

field along OO' by the hybrid method, where a grid resolution (Δ) of 25 cells/λ is used in the FDTD computation. A good agreement between the two curves can be seen.

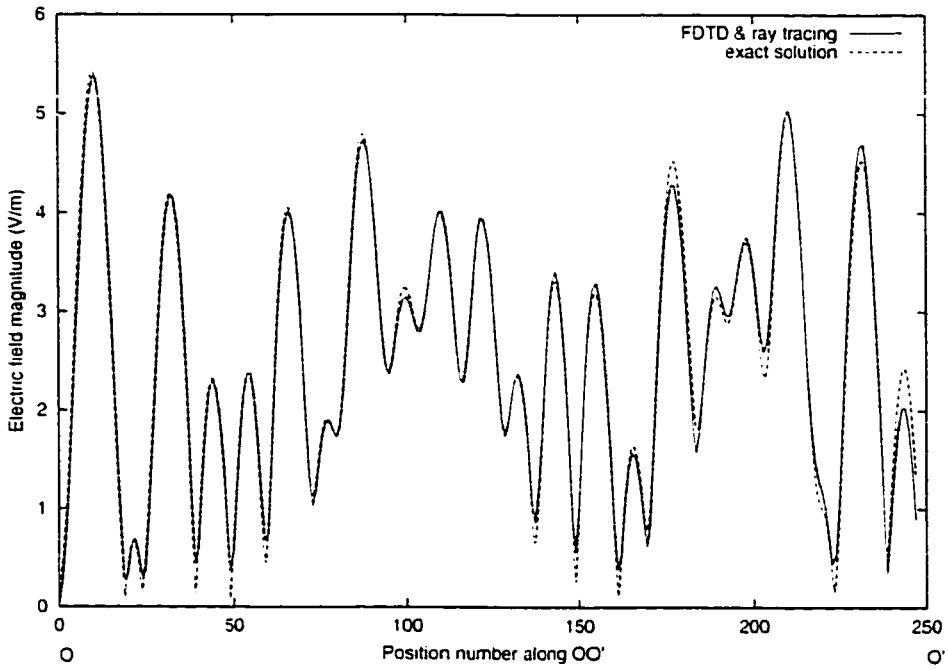

Fig. 3.5 Comparison of electric field distribution along OO' of Fig. 3.4 computed by the hybrid method and exact solution.

3.3.2 Penetration of wave from outdoor to indoor

Fig. 3.6 shows an example of applying the method to study wave penetration from outdoor to indoor. A wooden house, with dielectric constant ε_r=3 and $tan\delta$=0, is enclosed in the dashed-line rectangle ABCD. The transmitter is located outside of the house. Wave propagation from the transmitter to the rectangle ABCD is simulated by ray tracing, and FDTD is applied inside ABCD. The size of the house is chosen to be just a few wavelengths, so that full wave analysis by using FDTD can be applied to the entire scenario to verify the proposed method.

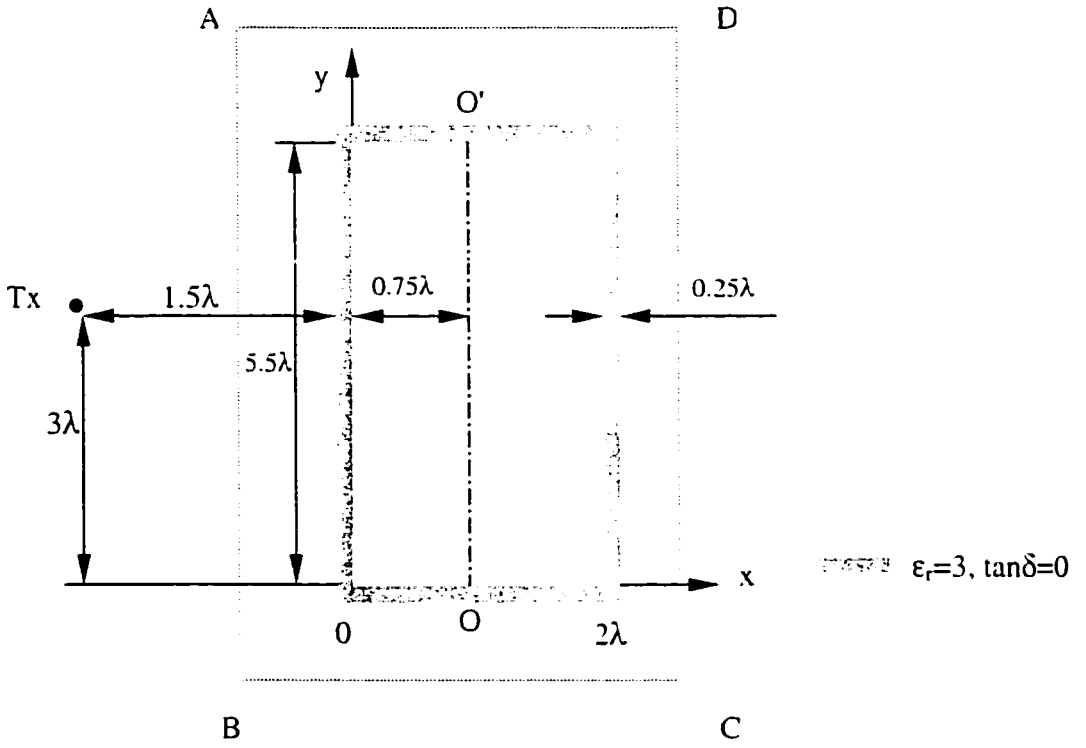

Fig. 3.6 2D lay out of a house with wooden walls and a transmitter located outside for studying penetration of wave from outdoor to indoor. The area of interest is enclosed by the virtual box ABCD.

Electric field distribution inside the house is computed and compared by three methods: FDTD method, the proposed hybrid method and the ray tracing method. In the first method, the entire region including the transmitter and the house is modeled by FDTD method. In both the second and the third methods, the ray tube angle α is set to be 0.5°. In the simulations in this chapter, the ray termination threshold is defined with reference to the field strength at one wavelength from the transmitting antenna in free space. Rays are terminated after their intensity dropped 30 dB below the reference level, i.e. threshold is –30 dB. It is observed that with lower threshold, there is no notable change in the resulting field distribution. In both the first and the second methods, the FDTD grid resolution is set to be 20 cells/λ. The dimension of the house is 2λ×5.5λ. Therefore, in total 4400 (40×110) locations inside the house are calculated by the hybrid

method and the ray tracing method. Results by the FDTD method are used as reference. Root mean square (rms.) errors of the other two methods and the computation CPU time on Pentium 450 are compared in Table 3.1. In such a simple situation, both ray tracing and the hybrid method give good results. It still can be seen that, by including diffraction from corners, the hybrid method is more accurate than ray tracing method. Fig. 3.7 shows electric field distribution along OO' of Fig. 3.6, which is 0.75λ away from the left wall.

Table 3.1 Comparison of rms. error and CPU time by the hybrid method and ray tracing method for the case in Fig. 3.6

	Hybrid method	Ray tracing method
rms. error (dB)	0.32	1.31
CPU time (S)	20	19

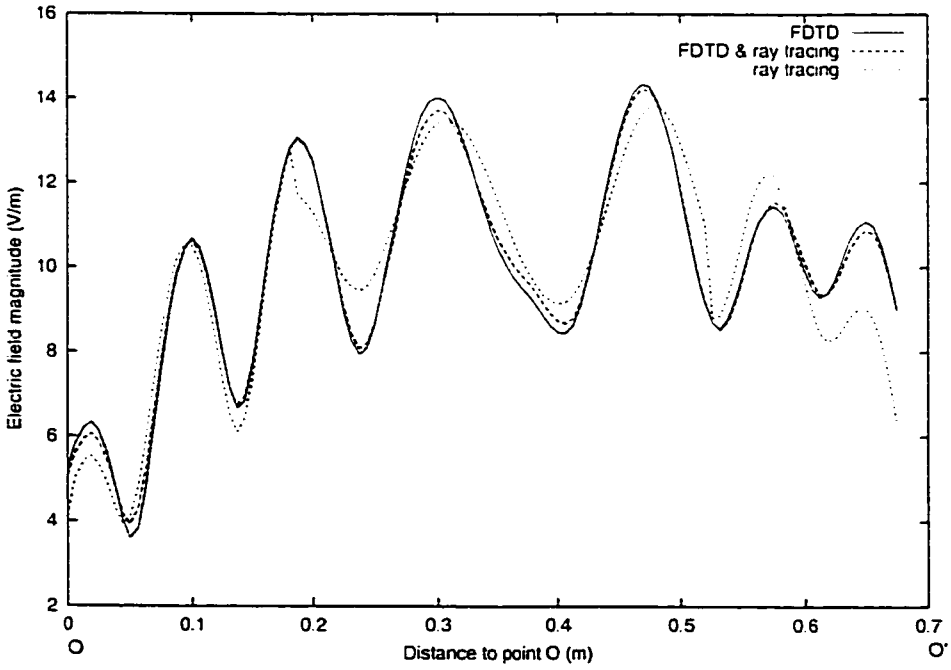

Fig. 3.7 Electric field distributions along OO' of Fig. 3.6.

Next, the situation in Fig. 3.6 is complicated by the presence of a lossy door with ε_r=5.2 and $tan\delta$=0.06 and a window with ε_r = 5 and $tan\delta$=0, as shown in Fig. 3.8. The electric field distribution along OO' is shown in Fig. 3.9. It can be observed that the accuracy of ray tracing degrades compared to results shown in Fig. 3.7 for the simple case. Obviously, the inhomogeneity in the left wall plays an important role in this case, which is omitted in GO approximations. As shown in Table 3.2, the rms. error of ray tracing is increased by 1.81 dB. However, the hybrid method still shows good accuracy.

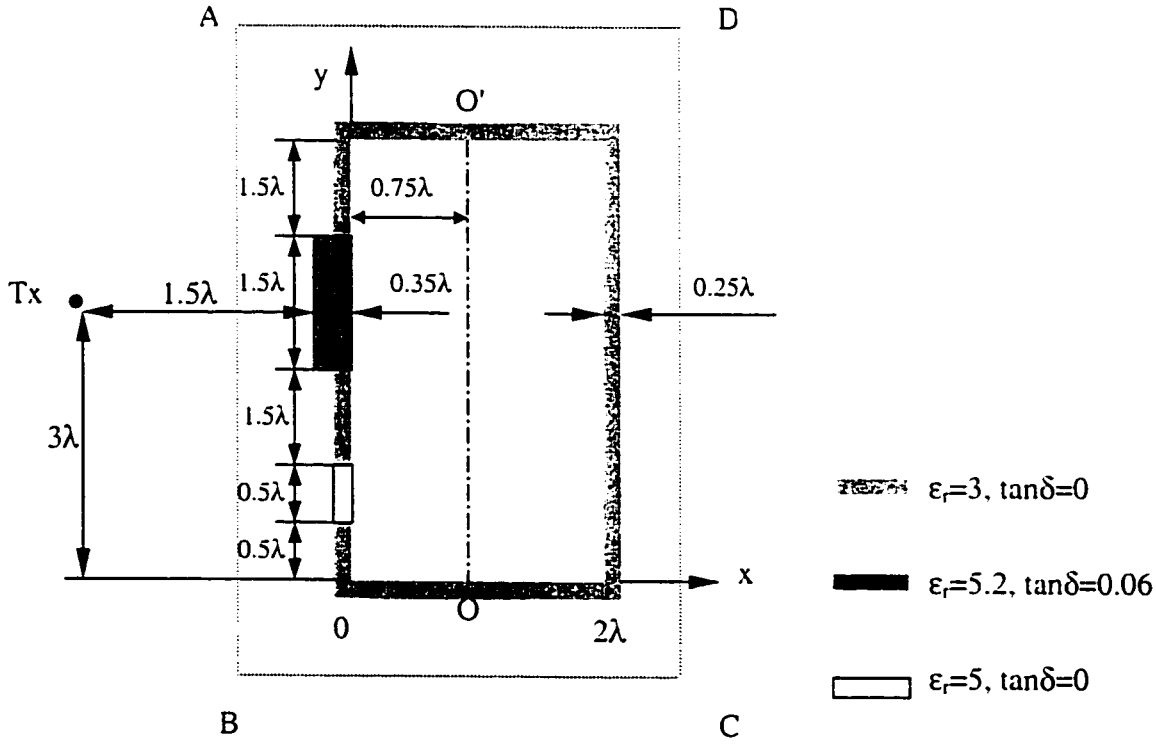

Fig. 3.8 2D lay out similar to Fig. 3.6 with the addition of a lossy door and a window.

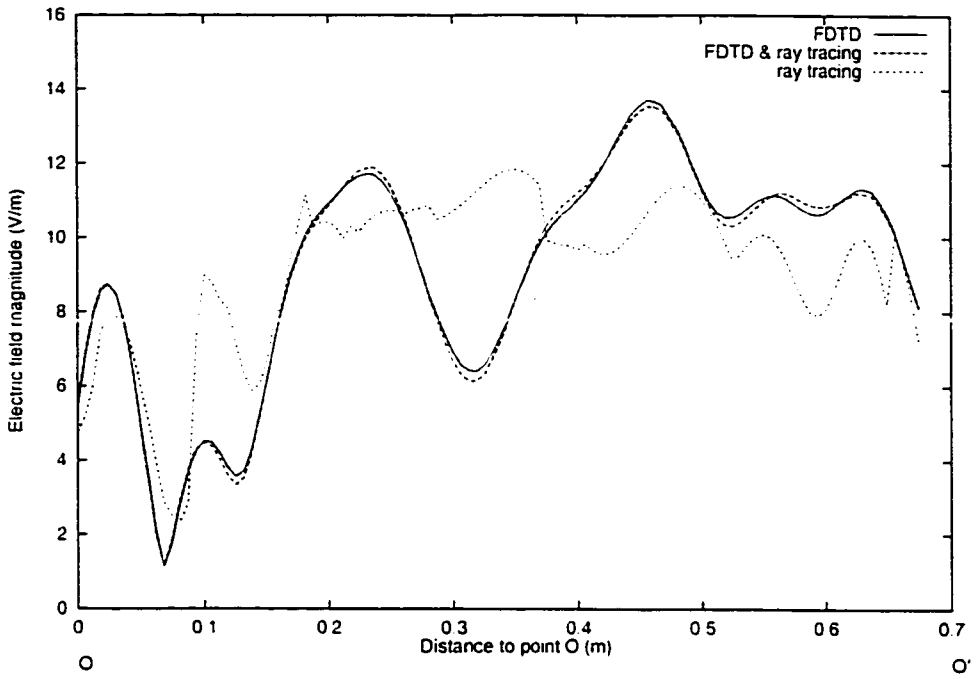

Fig. 3.9 Electric field distributions along OO' of Fig. 3.8.

Table 3.2 Comparison of rms. error and CPU time by the hybrid method and ray tracing method for the case in Fig. 3.8

	Hybrid method	Ray tracing method
rms. error (dB)	0.29	3.12
CPU time (S)	20	19

3.3.3 Indoor example

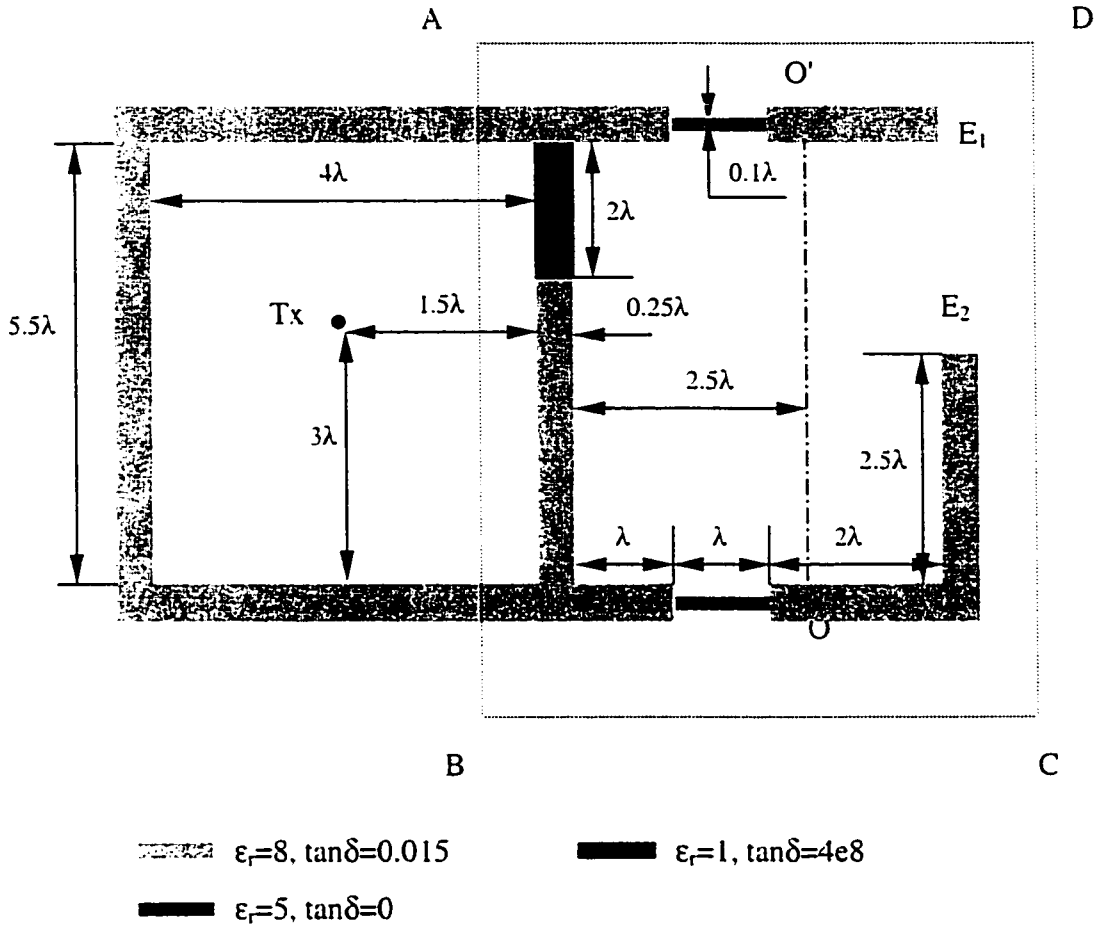

Fig. 3.10 Lay out of a two-room indoor environment. The right-side room is enclosed in ABCD and studied by FDTD.

The next example studied is a two-room structure with the transmitter located in the left-side room, as shown in Fig. 3.10. The building material of the wall is assumed to have dielectric constant ε_r=8 and $tan\delta$=0.015. A wall and a metallic door separate the two rooms. The structure of the left-side room is simple, hence modeled by ray tracing. The right-side room has two windows and an open door, which is enclosed in the dashed-line

rectangle ABCD and is studied by FDTD. Results of the hybrid method are compared with those obtained by applying FDTD method to both rooms and those of the ray tracing method. In ray tracing computations, the ray tube angle α is set to be 0.5° and threshold for ray termination is –30 dB. Beside reflections and transmissions, diffraction by the two diffracting edges, E_1 and E_2, is also included in ray tracing computations. In FDTD computations, the grid resolution is set to be 20 cells/λ. Both rooms are $4\lambda \times 5.5\lambda$ in size. Therefore, 8800 (80×110) locations inside the right-side room are calculated by the hybrid method and ray tracing method. Results by the FDTD method are used as reference.

Table 3.3 compares the rms. errors of ray tracing method and the hybrid method and CPU time on Pentium 450. It can be seen the accuracy is increased by about 2 dB by using the hybrid method. Fig. 3.11 shows electric field distributions along OO', which is arbitrarily chosen. A good agreement between the results by FDTD method and the results by the hybrid method can be observed. In this case the amount of CPU time needed by ray tracing is much more than the hybrid method, which is mainly because of the large number of computed receiving locations. Ray tracing is more efficient, in terms of computation time, if the number of receiving locations is less.

Table 3.3 Comparison of rms. error and CPU time by the hybrid method and ray tracing method for the case in Fig. 3.10

	Hybrid method	Ray tracing method
rms. error (dB)	2.21	4.24
CPU time (M:S)	1:32	2:31

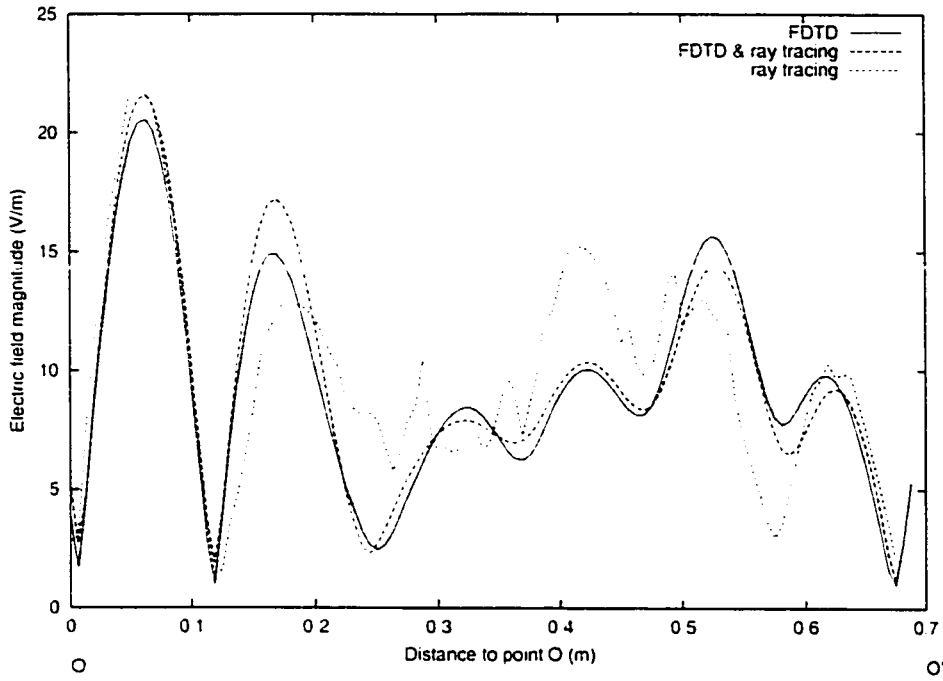

Fig. 3.11 Electric field distributions along OO' of Fig. 3.10.

3.3.4 Effect of ray resolution

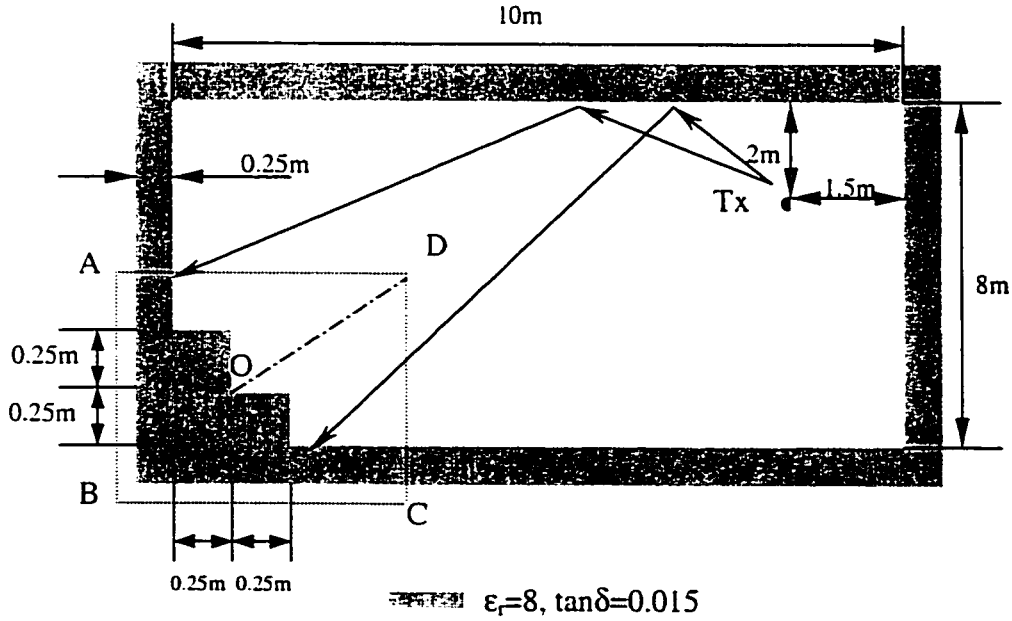

Fig. 3.12 A one-room structure with an L-shaped object at the left-bottom corner.

It is well known that a potential problem with ray tracing method is that it does not ensure that every signal path between the transmitter and receiver is considered, since it is impossible to send out infinite number of rays. The problem becomes more severe as the path length traveled by a ray from a source increases because of the spreading effect of the wave front of the ray tube and when the size of an object is small.

The example shown in Fig. 3.12 is used to illustrate this problem, which shows a room, 10m×8m in size, with an L-shaped structure at the left-bottom corner. Two adjacent rays are sent out from the transmitter and reflected by the wall. As shown in Fig. 3.12, The two reflected rays do not see the existence of the object at the corner. Were another ray sent out in-between, the total field at some locations, especially in the vicinity of the object, would be very different. Such problem can be alleviated by using the hybrid method. The area close to the object is enclosed in the rectangle ABCD in Fig. 3.12. Ray resolution becomes less of an issue where objects' size is large, such as the area outside of ABCD. Therefore, up to the incident plane of AD and CD, the electric field distribution can be correctly determined, whether for a fine or a reasonably coarse ray resolution. Inside ABCD, any wave reflection or scattering is taken into account by FDTD.

The curves in Fig. 3.13 show the electric field distributions along OD computed by the hybrid method when ray tube angle α=0.5° and α=2°. The two curves agree with each other quite well, which means same level of accuracy can be achieved with reduced number of rays.

Fig. 3.14 compares electric field distributions along OD computed by the ray tracing method at different ray resolutions, where large difference can be observed especially at locations close to the object. This tends to indicate that the hybrid method is more robust than the ray tracing method.

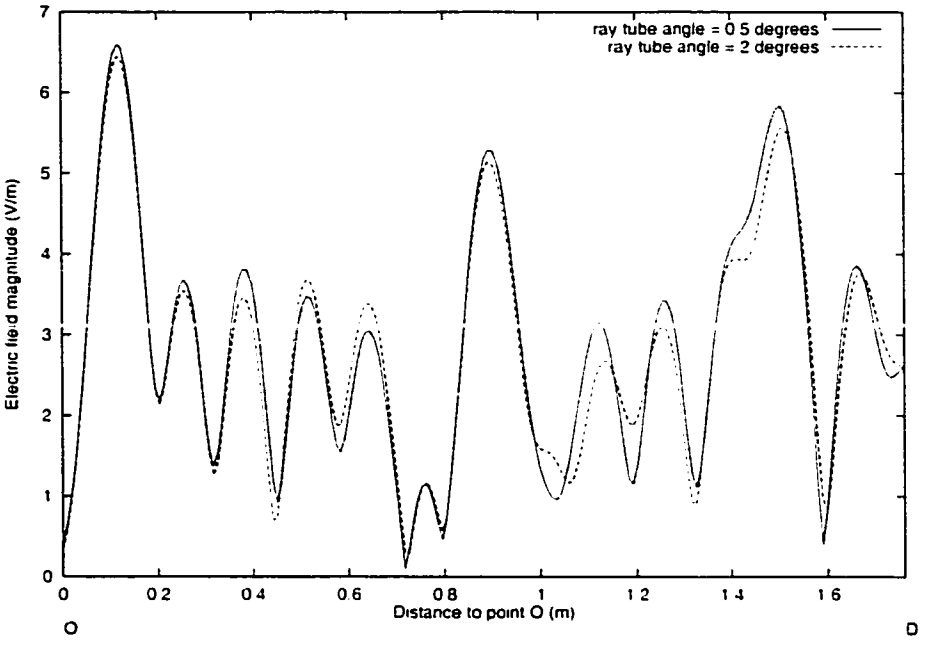

Fig. 3.13 Comparison of electric field distribution along OD of Fig. 3.12 computed by the hybrid method at different ray resolutions: $\alpha = 0.5°$ and $\alpha = 2°$.

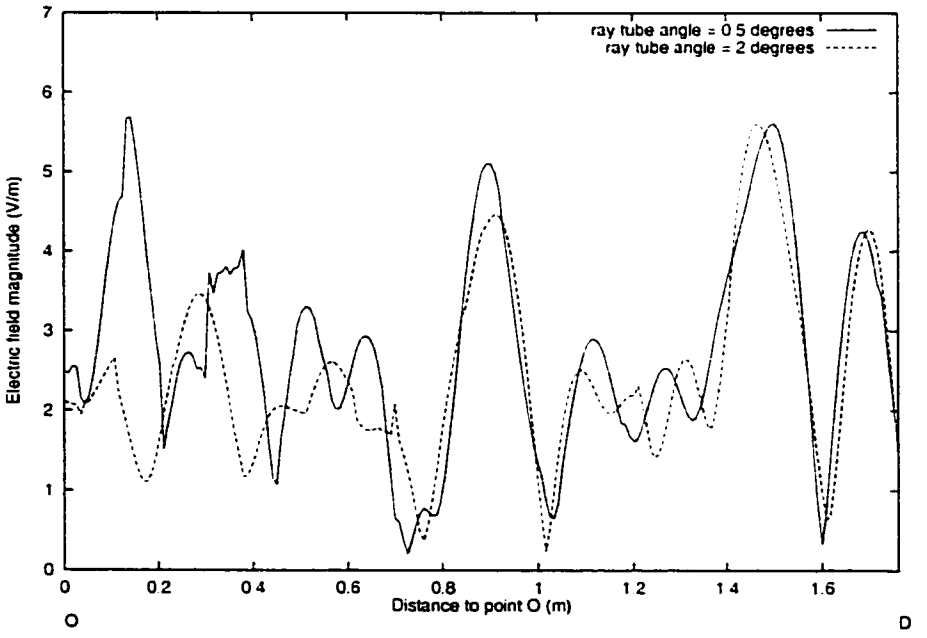

Fig. 3.14 Comparison of electric field distribution along OD of Fig. 3.12 computed by the ray tracing method at different ray resolutions: $\alpha = 0.5°$ and $\alpha = 2°$.

3.3.5 Comparison with field measurement

In this example, a comparison is made between simulation and measurement reported in [Hor86] for wave penetration through an exterior wall at 1.29 GHz. Fig. 3.15 shows the side view and top view of the empty room where the measurement was taken. The exterior wall is covered with metal-framed window and three concrete posts that separate windows. All other sides are made of concrete walls and wooden doors. A vertically polarized Yagi-array with 23 elements was used as the transmitting antenna, which is 888m away from the exterior wall and wave incident angle is 3° off the wall surface normal as marked in the figure. The receiving antenna is standard dipole antenna. The measuring course O_1O_2 is parallel to the windows and 1m away from the inner surface of the exterior wall, i. e. d=1m in Fig. 3.15. The measured signal envelope along O_1O_2 is shown in Fig. 3.16 [Hor86] with an offset of –35 dB for clarity.

For this far-zone simulation, the problem is treated as two-dimensional and an electric line source is assumed as the transmitter. Both the ray tracing and the hybrid methods are used. The material properties and some structural dimensions are adopted from reference [Yan98], where a comparison is made between ray tracing simulation and the measurement results mentioned above. In the hybrid method, the rectangle ABCD with a dimension of $75\lambda \times 9\lambda$ is drawn enclosing the exterior wall as shown in Fig. 3.15. Inside this area, the field distribution affected by metal-framed windows is obtained by FDTD method. In ray tracing computations, the ray tube angle α is set to be 0.01° in order to include the effect of concrete poles because of the large distance between transmitter and the room. Rays are terminated after their intensity dropped 40 dB below the reference level. In this case, the reference level is set to be the signal intensity at a location inside the room and right next to the window. Scattering effects of the window frames are not included in ray tracing computation.

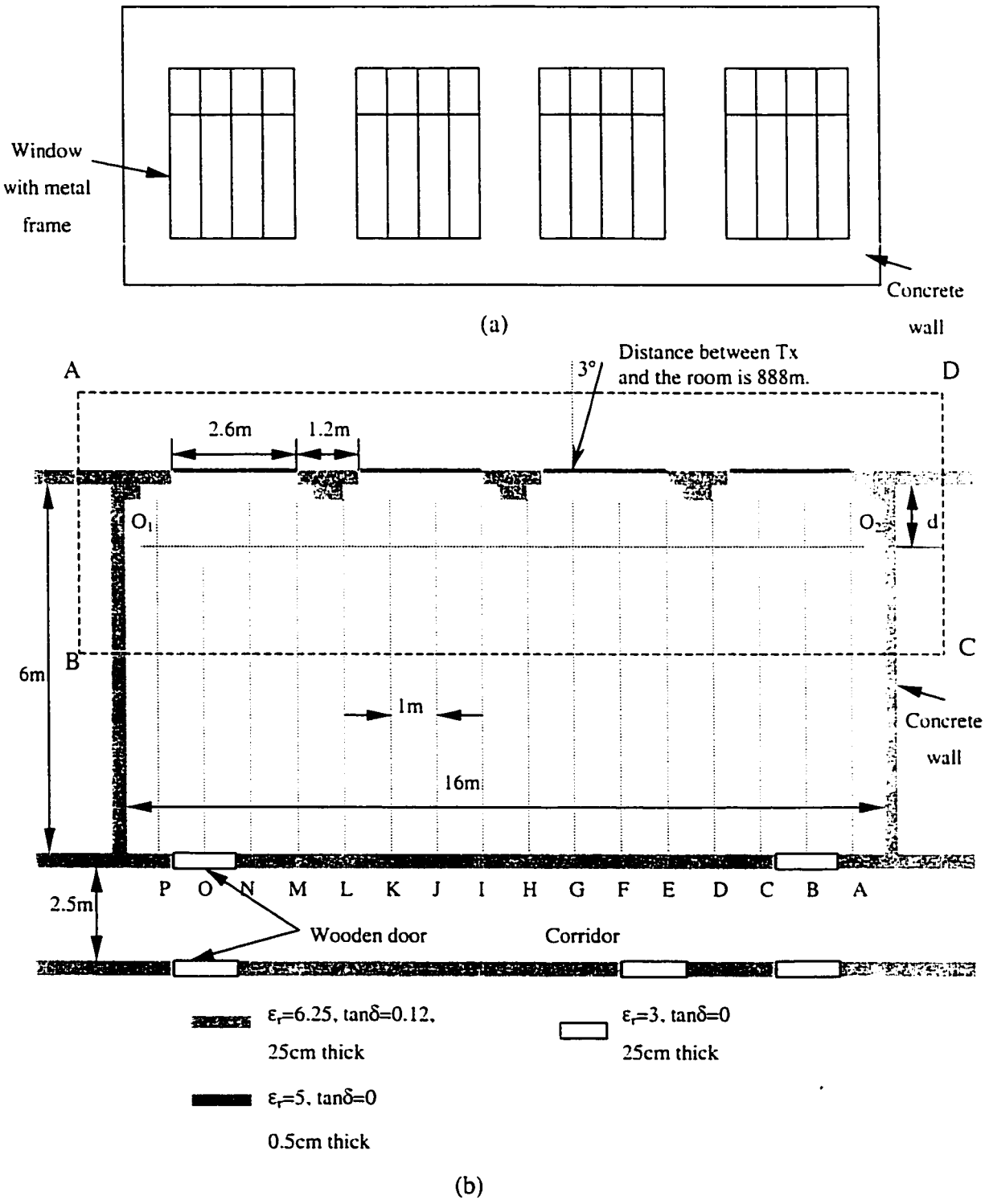

Fig. 3.15 (a) Side view and (b) top view of the room for simulation and measurement reported in [Hor86] of wave penetration through an exterior wall at 1.29 GHz.

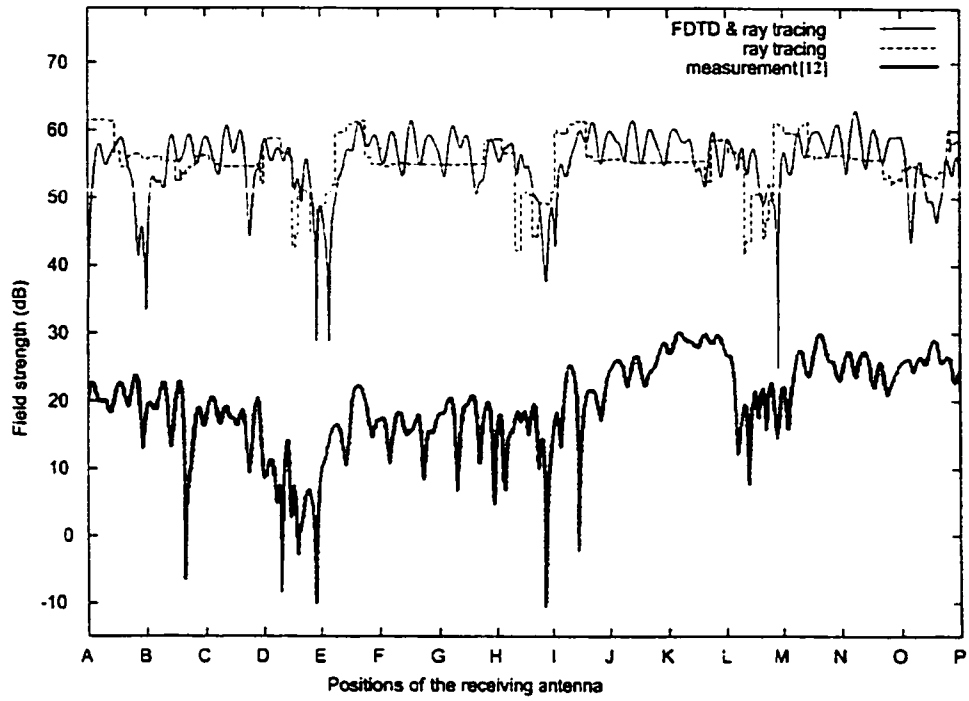

Fig. 3.16 Comparison of measured signal envelope along the measuring course O_1O_2 in Fig. 3.15 when d=1m [Hor86] with simulation results by the hybrid method and ray tracing method.

Simulation results are compared in Fig. 3.16, which have been normalized to the average signal level estimated from the measurement result. Reproduction of the measured signal envelope is impossible, since a lot of assumptions were made in the simulation due to the lack of accurate material and structural information, such as wall thickness, width of the metal frame, and dimensions of doors. However, as can be observed in Fig. 3.16, the results by the hybrid method accurately reproduce the fast fading phenomenon seen in the measured signal envelope and deep fades over 20-30 dB. The ray tracing results show a rather smooth variation along the measurement path similar to the simulation results reported in [Yan98] because of GO approximation. The results in [Yan98] show even less fluctuation than the ray tracing results in Fig. 3.16. Our

speculation is that a higher threshold was used in reference [Yan98], therefore less numbers of reflections inside the room were considered. Both ray tracing method and the hybrid method predict the excessive attenuation observed for signal envelope received near the poles.

3.4 Summary

A novel technique for site-specific modeling of indoor radio wave propagation is presented in this chapter, which combines the strength of ray tracing and FDTD methods. It has the flexibility of being able to be tailored to different environment according to desired accuracy. The FDTD module can be easily linked to existing ray tracing procedures.

The proposed method provides a tool for studying effect of complex lossy structures encountered in indoor communication environment where no asymptotic solution is available. Results presented have demonstrated the accuracy and robustness of this technique.

Theoretically, the method can be applied to all frequency ranges of indoor communication. However, when frequency goes up, it becomes more demanding for computational resources to study common indoor structures with dimensions on the order of meters.

In the next chapter, extension will be made to the hybrid method for the case of wave penetration from outdoor to indoor so that receiving points of interest does not have to be inside the FDTD computation domain. Hence, prediction of signal coverage can be made more efficiently.

Chapter 4

Extension of the Hybrid Method for Studying Wave Penetration through Inhomogeneous Walls

Study of outdoor-indoor radio signal coupling is an important issue in indoor radio propagation modeling, which has been motivated by the expansion of current cellular mobile services to indoor application and unification of the two types of services. It is known that the presence of inhomogeneities inside walls can have notable effects on signal coverage inside buildings. It is therefore important for reliable channel models to have the ability to study wave penetration through inhomogenous walls.

The hybrid method developed in Chapter 3 allows us to study the effects of generic indoor structural features, including inhomogeneities inside walls. The FDTD method is applied to areas close to complex discontinuities and field amplitude at each point within the FDTD computation domain can be obtained. Therefore, all receiving points of interest would need to be included in the box. If the receiving position of interest is far from the inhomogeneous wall, the FDTD computation domain can be quite large, which increase

the demand on computational resources. In this chapter, the hybrid method is extended for the case of wave penetration through inhomogeneous walls so that prediction of signal coverage far from the walls can be made more efficiently without compromising accuracy.

4.1 Description of Approach

The structure shown in Fig. 4.1(a) is used as an example to illustrate the method, which is a 2D environment with a transmitter, Tx, located outside a building. The exterior wall W_1W_2 may be made of inhomogeneous structures, such as metal bars, concrete blocks, or windows.

First the hybrid method based on combination of ray tracing and FDTD methods is used to study wave penetration through the inhomogeneous wall W_1W_2. The region of interest in the simulation area is enclosed by a virtual box. Incident waves arriving at the box, which are determined through ray tracing, are propagated into the region of interest by the FDTD propagator. In the case shown in Fig. 4.1(a), if the receiving points are far from W_1W_2 the FDTD computation domain would need to be very large. However, in the approach proposed here, it is not necessary to apply the accurate FDTD method to such a large area, since except for wall W_1W_2 the rest of the environment is homogeneous and simple. Ray tracing method can provide accurate estimation of field intensity more efficiently in terms of computation time.

To this end, the virtual box ABCD is positioned as shown in Fig. 4.1(a). The size of box is slightly larger than wall W_1W_2 so that the FDTD computation domain is reduced to minimum. Side BC of the virtual box is illuminated by the rays sent out from the transmitter and reflected rays from neighboring objects. After FDTD computation, transmitted electric and magnetic fields though wall W_1W_2 can be found along AD in Fig. 4.1(a).

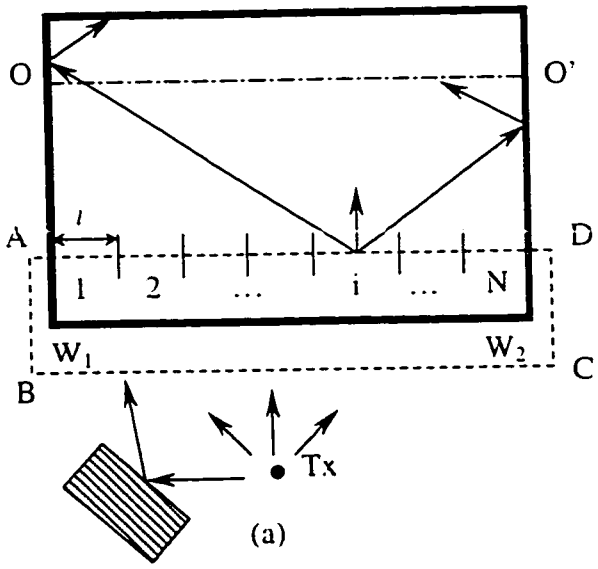

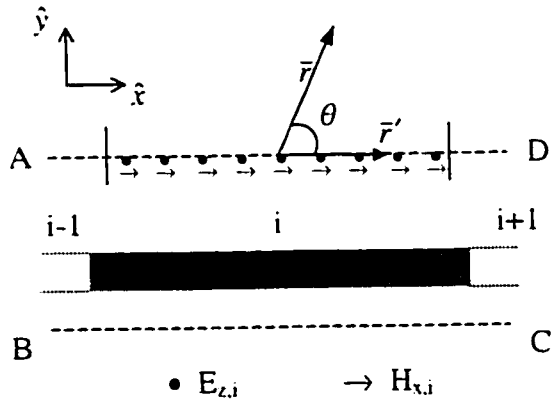

Fig. 4.1 (a) A 2D environment with a transmitter, Tx, located outside a building. FDTD computation domain is enclosed in ABCD. AD is partitioned into *N* sections. (b) Tangential electric and magnetic fields along the *i*th section.

In order to study the rest of the building using ray tracing, the next step is to send out rays from AD based on the transmitted field distribution along AD. To accomplish this, AD is partitioned into N sections, with length of each section being l, as shown in Fig. 4.1(a). Second order rays are sent out from the center of each section. The ith section is enlarged in Fig. 4.1(b). To simplify the explanation, TM polarization, which involves three field components: E_z, H_x and H_y, is assumed in what follows. $E_{z,i}$ and $H_{x,i}$ are tangential electric and magnetic fields along the ith section of the FDTD domain border, as shown in Fig. 4.1(b). To find electric field of each ray, the near-to-far-field transformation equation (8.12) in [Taf95] is used and simplified to be

$$E_z(\bar{r}) = \frac{e^{-jkr}}{\sqrt{r}} \frac{e^{j\pi/4}}{\sqrt{8\pi k}} \int_{-l/2}^{l/2} \left(\omega \mu_0 H_{x,i}(\bar{r}') + k E_{z,i}(\bar{r}') \hat{y} \cdot \hat{r}\right) e^{jk\hat{r}\cdot\bar{r}'} dx' \qquad (4.1)$$

where $\bar{r}$ is the position vector of the observation point, $\bar{r}'$ is the vector of the source point and k is the wavenumber. In order to make the far field assumption valid in the above equation, length of each section need to be small enough so that the distance between the observation point and any source points on the ith section is much larger than the length of the section. $l = \lambda/2$ is used in the following simulations, where λ is the wavelength of the incident wave. Rays are only sent out in the upper half space, i. e. $0° < \theta < 180°$ in Fig. 4.1(b). Once direction and electric field of each ray is determined, rays are traced throughout the environment as in the ray tracing method described in Chapter 2. Thus, field intensity at any interested position inside the building can be obtained.

4.2 Plane Wave Incidence upon Periodic Structures

When the transmitter is located far from the exterior wall of the building, the incident wave can be considered plane wave or superposition of plane waves. Furthermore, periodicity usually exists in one or more dimensions of the wall structure. Taking advantage of the periodicity can lead to greater efficiency in solving the problem.

FDTD method has been applied to the problem of electromagnetic wave scattering by periodic rough surfaces for normal incident plane wave [Cha91]. Fig. 4.2 shows an example of a periodic wall that can replace W_1W_2 in Fig. 4.1. Due to its periodic nature, the problem can be solved by applying FDTD to single cell, i.e. each periodic feature of the whole structure as shown in Fig. 4.2, and applying periodic boundary conditions along boundaries A_kB_k and C_kD_k between each cell. For oblique incidence, the problem is more complicated, since there is a cell-to-cell phase shift causing the time-domain implementation to become more difficult. In [Vey93] and [Rod98], Floquet field mapping is applied for oblique incidence. It results in a set of mapped fields which possess the same cell-to cell field relations as exist for the normally incident unmapped fields. The split-field update method introduced by Roden and et. al. [Rod98], which has the advantages of simple implementation and less strict stability criterion, is used in the following computations.

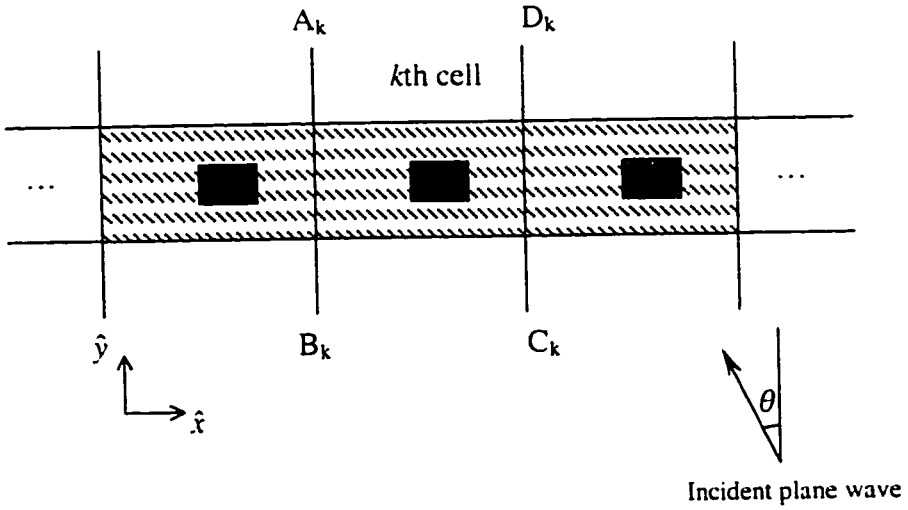

Fig. 4.2 Plane wave incidence at an angle θ upon a periodic geometry.

The technique is briefly introduced using an example of TM plane wave incident at an angle θ on a 2D material, which is periodic in the $\hat{x}$ direction, as shown in Fig. 4.2. With $\theta \neq 0$, field components E_z, H_x and H_y will have a phase shift of the form $e^{jk_x x}$, where $k_x=\omega \cdot sin\theta/c$ and c is the speed of light in free space, and are not periodic in the $\hat{x}$ direction. Auxiliary variables are introduced as

$$P_z = \frac{E_z e^{-jk_x x}}{\eta_0} \tag{4.2a}$$

$$Q_x = H_x e^{-jk_x x} \tag{4.2b}$$

$$Q_y = H_y e^{-jk_x x} \tag{4.2c}$$

where η_0 is the impedance of free space. With these definitions, P_z, Q_x and Q_y become periodic functions in the $\hat{x}$ direction and the periodic boundary condition can be applied by constraining the tangential fields on opposing boundary walls, e.g. A_kB_k and C_kD_k in Fig. 4.2, to be equivalent. (4.2a)~(4.2c) are then substituted into Maxwell's equations and discretized to obtain a numerical solution. [Rod98] gives equations for lossless media, i.e. conductivity σ = 0. In what follow, more general equations for media with finite conductivity will be given.

Substituting P_z, Q_x and Q_y into Maxwell's equations leads to

$$\frac{\varepsilon_r}{c}\frac{\partial P_z}{\partial t} = \left(\frac{\partial Q_y}{\partial x} - \frac{\partial Q_x}{\partial y} - \sigma\eta_0 P_z\right) + \frac{\sin\theta}{c}\frac{\partial Q_y}{\partial t} \tag{4.3a}$$

$$\frac{\mu_r}{c}\frac{\partial Q_x}{\partial t} = -\frac{\partial P_z}{\partial y} \tag{4.3b}$$

$$\frac{\mu_r}{c}\frac{\partial Q_y}{\partial t} = \frac{\partial P_z}{\partial x} + \frac{\sin\theta}{c}\frac{\partial P_z}{\partial t} \tag{4.3c}$$

The last term in both (4.3a) and (4.3c) causes difficulty in the discretization. In [Rod98], it is suggested that P_z and Q_y be split into two parts: $P_z = P_z^a + P_z^b$ and $Q_y = Q_y^a + Q_y^b$, where

$$\frac{\varepsilon_r}{c}\frac{\partial P_z^a}{\partial t} = \left(\frac{\partial Q_y}{\partial x} - \frac{\partial Q_x}{\partial y} - \sigma \eta_0 P_z \right) \tag{4.4a}$$

$$P_z^b = \frac{\sin\theta}{\varepsilon_r} Q_y \tag{4.4b}$$

$$\frac{\mu_r}{c}\frac{\partial Q_y^a}{\partial t} = \frac{\partial P_z}{\partial x} \tag{4.5a}$$

$$Q_y^b = \frac{\sin\theta}{\mu_r} P_z \tag{4.5b}$$

From (4.4b) and (4.5b), we have

$$P_z = \frac{P_z^a}{1 - \dfrac{\sin^2\theta}{\varepsilon_r \mu_r}} + \frac{\sin\theta}{\varepsilon_r - \dfrac{\sin^2\theta}{\mu_r}} Q_y^a \tag{4.6}$$

Equations (4.3b), (4.4a), (4.5a), (4.5b), and (4.6) are discretized into

$$P_z^{a^n}(i,j) = A(i,j)\cdot P_z^{a^{n-1}}(i,j) + B(i,j)\cdot \left(\begin{array}{l} \dfrac{Q_y^{n-1/2}(i+1/2,j) - Q_y^{n-1/2}(i-1/2,j)}{\Delta x} \\ - \dfrac{Q_x^{n-1/2}(i,j+1/2) - Q_x^{n-1/2}(i,j-1/2)}{\Delta y} \end{array} \right) \tag{4.7a}$$

$$Q_x^n(i,j+1/2) = Q_x^{n-1}(i,j+1/2) - \frac{c\Delta t}{\mu_r(i,j+1/2)} \cdot \left(\frac{P_z^{n-1/2}(i,j+1) - P_z^{n-1/2}(i,j)}{\Delta y} \right) \tag{4.7b}$$

$$Q_y^{a^n}(i+1/2,j) = Q_y^{a^{n-1}}(i+1/2,j) + \frac{c\Delta t}{\mu_r(i+1/2,j)} \cdot \left(\frac{P_z^{n-1/2}(i+1,j) - P_z^{n-1/2}(i,j)}{\Delta x} \right) \tag{4.7c}$$

$$P_z^n(i,j) = \frac{P_z^{a^n}(i,j)}{1-\dfrac{\sin^2\theta}{\varepsilon_r(i,j)\mu(i,j)_r}} + \frac{\sin\theta}{\varepsilon_r(i,j)-\dfrac{\sin^2\theta}{\mu_r(i,j)}}\frac{1}{2}[Q_y^{a^n}(i+\frac{1}{2},j)+Q_y^{a^n}(i-\frac{1}{2},j)] \quad (4.7d)$$

$$Q_y^{b^n}(i+1/2,j) = \frac{\sin\theta}{\mu_r(i+1/2,j)}\cdot\frac{1}{2}\cdot\left[P_z^n(i+1,j)+P_z^n(i,j)\right] \quad (4.7e)$$

where

$$A(i,j) = \frac{1-\dfrac{\sigma(i,j)c\Delta t}{2\varepsilon_r(i,j)}\eta_0}{1+\dfrac{\sigma(i,j)c\Delta t}{2\varepsilon_r(i,j)}\eta_0}, \qquad B(i,j) = \frac{\dfrac{c\Delta t}{\varepsilon_r(i,j)}}{1+\dfrac{\sigma(i,j)c\Delta t}{2\varepsilon_r(i,j)}\eta_0}$$

In (4.7), each field component is computed at each half time step, i. e. $n = 0,1/2,1,3/2,2,\ldots$.

The conventional absorbing boundary conditions of FDTD method also need to be modified. Assume E_z to be the field component tangential to the absorbing boundary. The absorbing boundary condition along A_kD_k in Fig. 4.2 can be written as [Taf95]

$$\left(\frac{\partial^2}{\partial y\partial t}+\frac{1}{c}\frac{\partial^2}{\partial t^2}-\frac{c}{2}\frac{\partial^2}{\partial x^2}\right)E_z = 0 \quad (4.8)$$

After substituting (4.2a) into (4.8) and transformation, we can obtain the absorbing boundary condition equation for P_z as [Vey93]

$$\left[\frac{\partial^2}{\partial y\partial t}+\frac{1}{c}\left(1-\frac{1}{2}\sin^2\theta\right)\frac{\partial^2}{\partial t^2}-\sin\theta\frac{\partial^2}{\partial x\partial t}-\frac{c}{2}\frac{\partial^2}{\partial x^2}\right]P_z = 0 \quad (4.9)$$

Absorbing boundary condition along B_kC_k can be derived in the same manner.

Once P_z, Q_x and Q_y are calculated, E_z, H_x and H_y can be obtained by using (4.2) or a gradual time shift in the time domain:

$$E_z(x, y, t) = P_z(x, y, t + x\sin\theta / c)$$
$$H_x(x, y, t) = Q_x(x, y, t + x\sin\theta / c)$$
$$H_y(x, y, t) = Q_y(x, y, t + x\sin\theta / c)$$

Using periodicity of the structure, electric and magnetic fields along the entire wall can be obtained from the fields of single cell calculated above. Then, following the approach introduced in section 4.1, higher-order rays are sent out to cover the rest of the area in Fig. 4.1. Note that the finite length of the wall and corners at the two ends of the wall are ignored. Effects caused by the approximations are shown to be insignificant for the prediction of signal strength in the following numerical results.

4.3 Numerical Results

4.3.1 Non-plane wave incidence

Example A

To validate this method, the transmission property of a concrete block wall is studied first. A measurement of transmission through a concrete block wall at 3 GHz is reported in [Hon94], in which two standard gain horn antennas were set up on either side of a concrete block wall, as shown in Fig. 4.3(a). Detailed dimension of each concrete block is shown in Fig. 4.3(b). Both antennas were 3 feet from the wall. The receiving antenna was moved in an arc. The relative dielectric constant for the concrete of which the blocks were made was assumed to be 3. The electric field magnitude along the arc as a function of receiver angle θ is calculated by the extended hybrid method and shown in Fig. 4.4(a).

The field intensity has been normalized to the received signal when the two antennas face each other at boresight in the absence of the wall. It can be observed that the transmitted field has a significant amount of power in non-specular directions and most of the scattered radiation occurs in the range of angles between 30° and 60°. These observations agree very well with the results of measurement and computation made by Honcharenko and Bertoni [Hon94] shown in Fig. 4.4(b), where the computation result is offset by -10 dB for clarity. Peak amplitudes of the transmitted signal are also very similar.

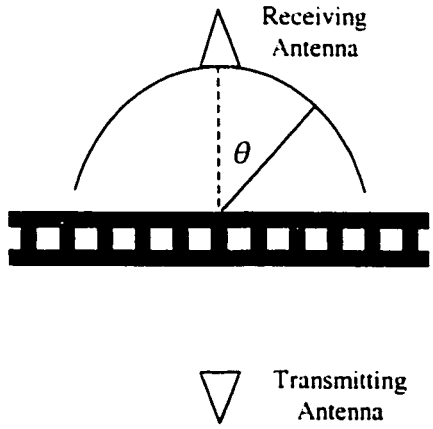

(a)

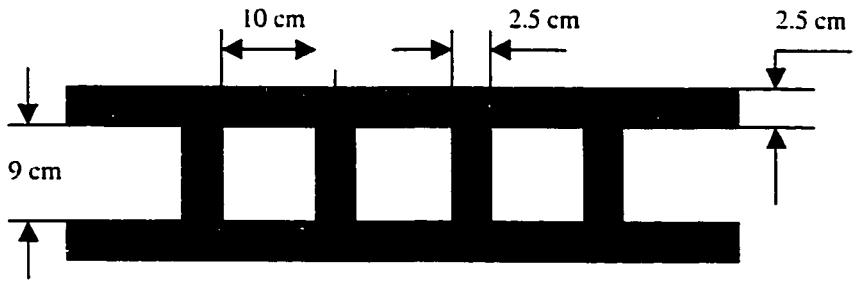

(b)

Fig. 4.3 (a) Measurement of wave penetration through a concrete block wall at 3 GHz [Hon94]. (b) Dimension of each concrete block.

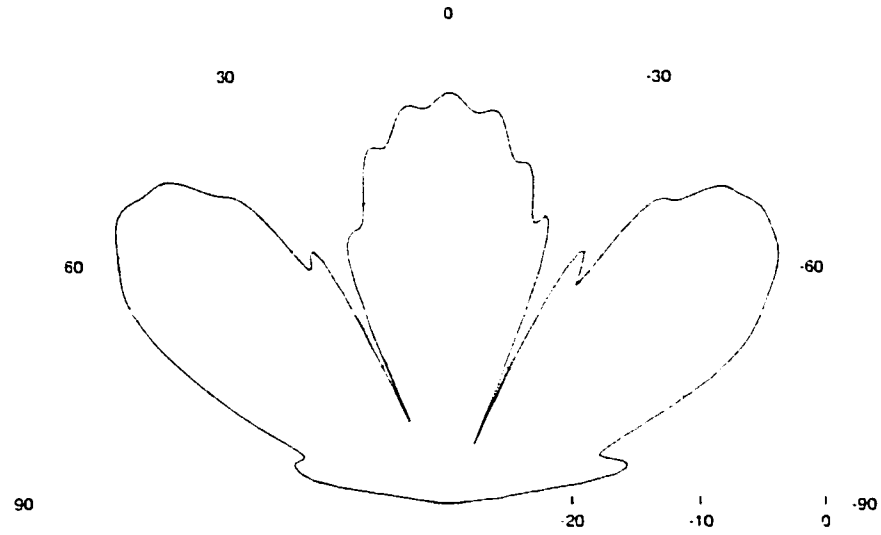

(a)

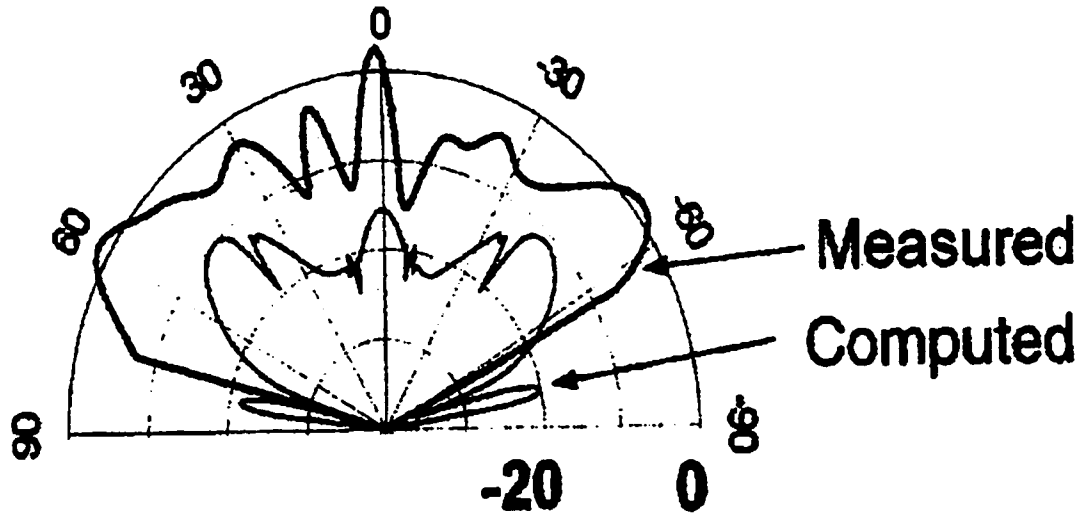

(b)

Fig. 4.4 The electric field distribution (dB) along the arc in Fig. 4.3: (a) calculated by the proposed method and (b) measurement and simulation results in [Hon94].

Example B

In the next example, the structure in Fig. 4.1 is treated. An omni-directional transmitting antenna is positioned outside of a building with the size of 2m×2m. The size of the building is chosen to be relatively small, so that later on full wave analysis by using FDTD method can be applied to the entire building to verify the proposed method. Four walls of the building are made of homogeneous material. Wall W_1W_2 is 14cm thick and the other three walls are 10cm thick. Dielectric constant is assumed to be the same as that in previous example. Both the hybrid method and the ray tracing method are used to study this structure. In the hybrid method, the FDTD computation domain is enclosed in the rectangle ABCD. Wave propagation from the transmitter to the rectangle ABCD is simulated by ray tracing, and FDTD is applied inside ABCD. Then, using tangential electric and magnetic fields along AD, higher-order rays are sent out to find field intensity at any interested locations inside the building.

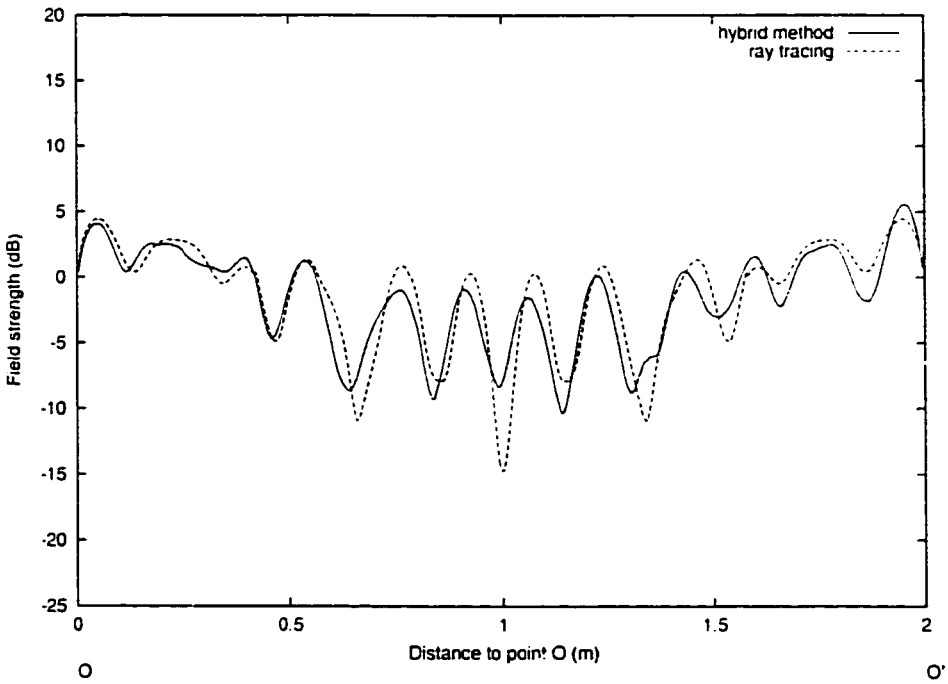

Fig. 4.5 Electric field distributions along OO' of Fig.4.1 when wall W_1W_2 is homogeneous.

Fig.4.5 shows electric field distributions along OO' of Fig. 4.1, which is 1.45m away from wall W_1W_2, calculated by the two methods at 3 GHz. The field intensity has been normalized to the received signal when the transmitting antenna is radiating in free space. It can be seen that results by ray tracing and the hybrid method are quite similar for such a simple situation. The standard deviation between two sets of data is only 1.82 dB.

Next, the structure in Fig. 4.1 is complicated by using the concrete block wall in Fig. 4.3 as W_1W_2. Three methods are used to treat the problem: FDTD method applied to the entire building, the hybrid method, and the ray tracing method. Results by the FDTD method are used as reference. Electric field distributions along OO' calculated by the three methods are compared in Fig. 4.6. Notable differences are observed between the results by ray tracing method and those by FDTD method with the standard deviation being 7.22 dB. However, the results by the hybrid method agree with those by FDTD method very well, and the standard deviation is only 1.66 dB.

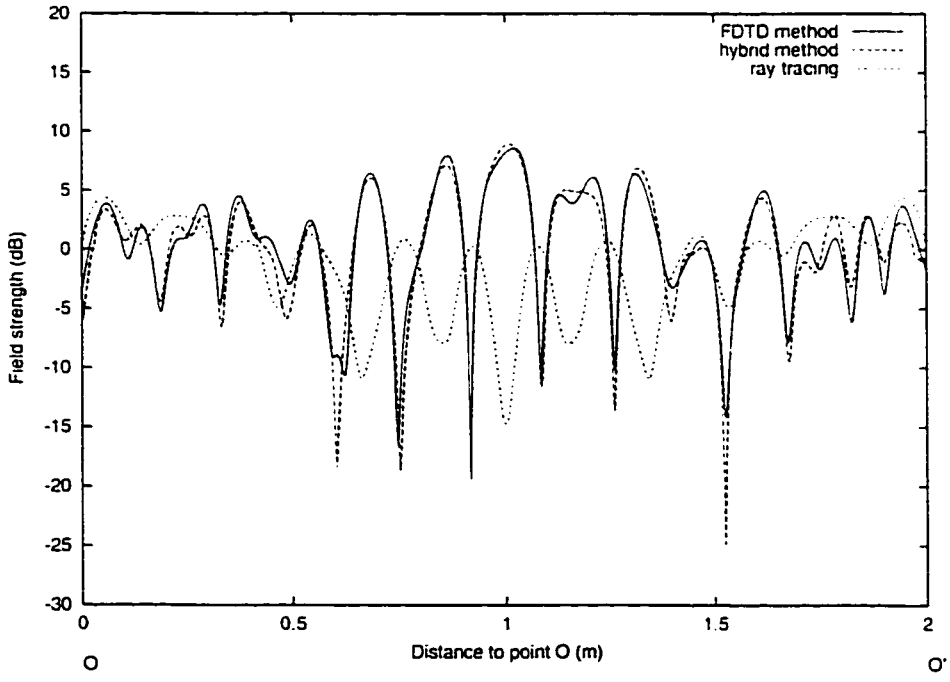

Fig. 4.6 Electric field distributions along OO' of Fig. 4.1 when wall W_1W_2 is made of concrete blocks.

The computation time of the hybrid method is about 25 minutes, which is approximately 10 times less than the FDTD method. In real indoor environment where the structure is usually much larger than the case in Fig. 4.1, the difference in computation times can be expected to be even larger.

Example C

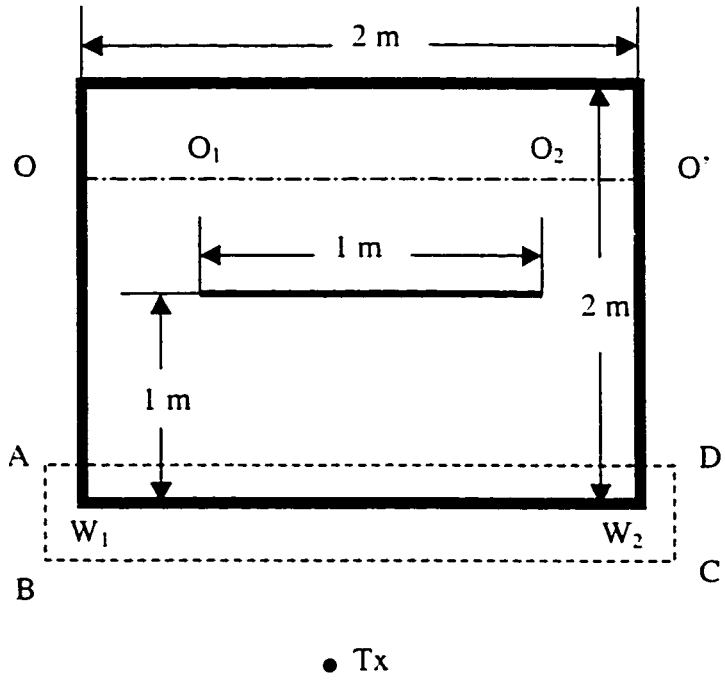

Fig. 4.7 A 2D environment with a thin metallic slab positioned in the center of a building. The FDTD computation domain is enclosed in ABCD.

Fig. 4.7 shows a structure same as the one in the previous example except that a thin metallic slab is positioned in the center of the building. Wall W_1W_2 is made of the concrete blocks in Fig. 4.3(b). Again, electric field distributions along OO' are computed and compared by three methods: FDTD method, the extended hybrid method and the ray

tracing method. In both the hybrid and the ray tracing methods, the ray tube angle α is set to be 0.5°. Rays are terminated after their intensity dropped 60 dB below the reference level, which is defined to be the field strength at one wavelength from the transmitting antenna in free space. In both the hybrid and the FDTD methods, the FDTD grid resolution is set to be 40 cells/λ.

Fig. 4.8 compares electric field distributions along OO' obtained using the ray tracing method and FDTD method. The line is located 4.5λ away from the metallic slab in Fig. 4.7. It can be observed that right behind the metallic slab, the electric field intensity along O_1O_2 predicted by ray tracing is in average 11.5 dB lower than the signal predicted by the FDTD method, which shows inadequacy of ray tracing for studying this case. It can be explained by the results of example A, where the transmitted field through the concrete block wall has a substantial amount of power in non-specular directions, especially at ±45°. The slab blocks the direct transmitted wave from the transmitter. Ray tracing can only take into account transmitted-reflected rays by the side walls or diffracted rays by the slab, whose intensities are much lower than the non-specular signals. Reflected by the two side walls, the non-specular waves carry significant power to the area behind the metallic slab, which is omitted by ray tracing.

A notable improvement in the results can be obtained by utilizing the hybrid method as shown in Fig. 4.9. Using results of the FDTD method as reference, table 4.1 compares rms. errors of field distributions along OO' by the other two methods in addition to the computation CPU time on a Pentium 450.

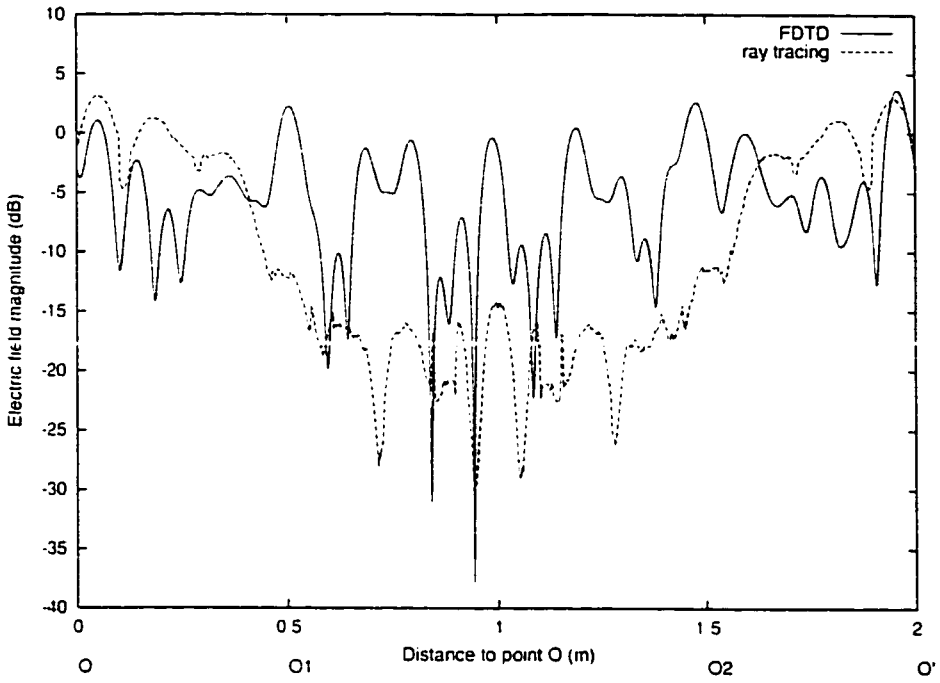

Fig. 4.8 Electric field distributions along OO' of Fig. 4.7 obtained by ray tracing and FDTD methods.

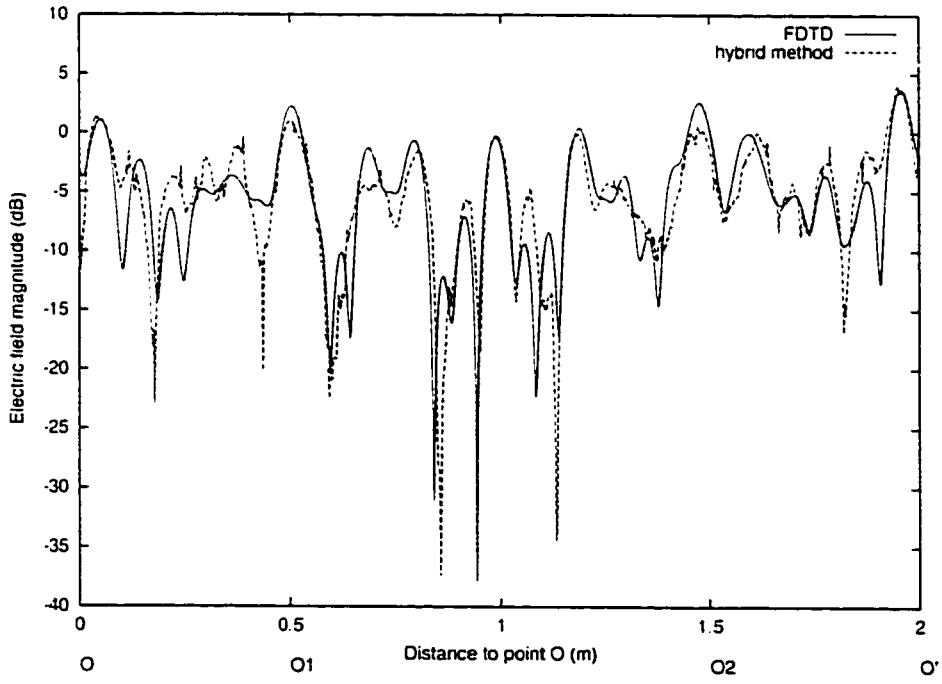

Fig. 4.9 Electric field distributions along OO' of Fig. 4.7 obtained by the hybrid method and FDTD method.

Table 4.1 Comparison of error and CPU time of the electric field distribution along OO' of Fig. 4.7 calculated by three methods

	FDTD method	Hybrid method	Ray tracing method
rms. error (dB)	0	3.78	10.02
CPU time (H:M:S)	4:18:32	0:25:37	0:0:8

4.3.2 Plane wave incidence on periodic structure

In this section, examples with plane wave incidence on periodic structures will be studied. Simulations are again carried out at 3 GHz.

Example A

The first structure is the same as in Fig. 4.7. However, the source is a plane wave perpendicularly incident on wall W_1W_2. In this case, only single cell of the concrete block wall needs to be treated by FDTD to determine the tangential electric and magnetic field along AD in the hybrid method. Equations given in section 4.2 are used in the FDTD computation in stead of the conventional FDTD equations. In ray tracing computations, rays are terminated after their intensity dropped 60 dB below the field strength of the incident plane wave.

Table 4.2 Comparison of error and CPU time of the electric field distributions along OO' of Fig. 4.7 calculated by the FDTD method, the hybrid method and the ray tracing method for the case of plane wave incidence

	FDTD method	Hybrid method	Ray tracing method
rms. error (dB)	0	4.70	15.80
CPU time (H:M:S)	4:20:9	0:5:59	0:0:34

Table 4.2 compares rms. errors of field distributions along OO' and the computation CPU time on a Pentium 450 for the FDTD method, the hybrid method and the ray tracing method. Comparing to the previous example as shown in table 4.1, we can see that while retaining accuracy of the results, computation time by the hybrid method is further reduced by making use of the periodic property of the problem. Fig. 4.10 shows electric field distributions obtained using the ray tracing method and FDTD method along OO'. The results have been normalized to the field intensity of incident plane wave. The slab blocks the direct transmitted wave through wall W_1W_2. In ray tracing method, only diffracted rays by the edges of the slab can cover the area right behind the metallic slab, because of the perpendicular angle of the incident wave. Without considering diffraction, the field intensity along O_1O_2 would be zero. The real signal intensity is much higher because of the of the non-specular scattered waves are reflected by the side walls and reach the area behind the slab.

Comparison between electric field distributions obtained using the hybrid method and FDTD method along OO' is shown in Fig. 4.11. A much-improved agreement between the two curves can be observed.

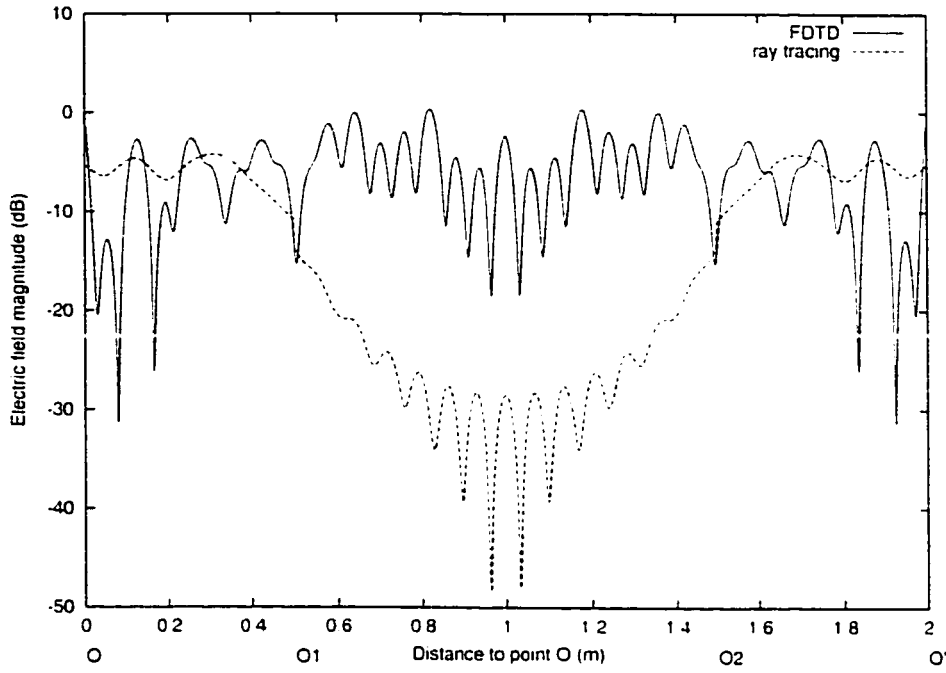

Fig. 4.10 Electric field distributions along OO' of Fig. 4.7 obtained by ray tracing method and FDTD method for the case of plane wave incidence.

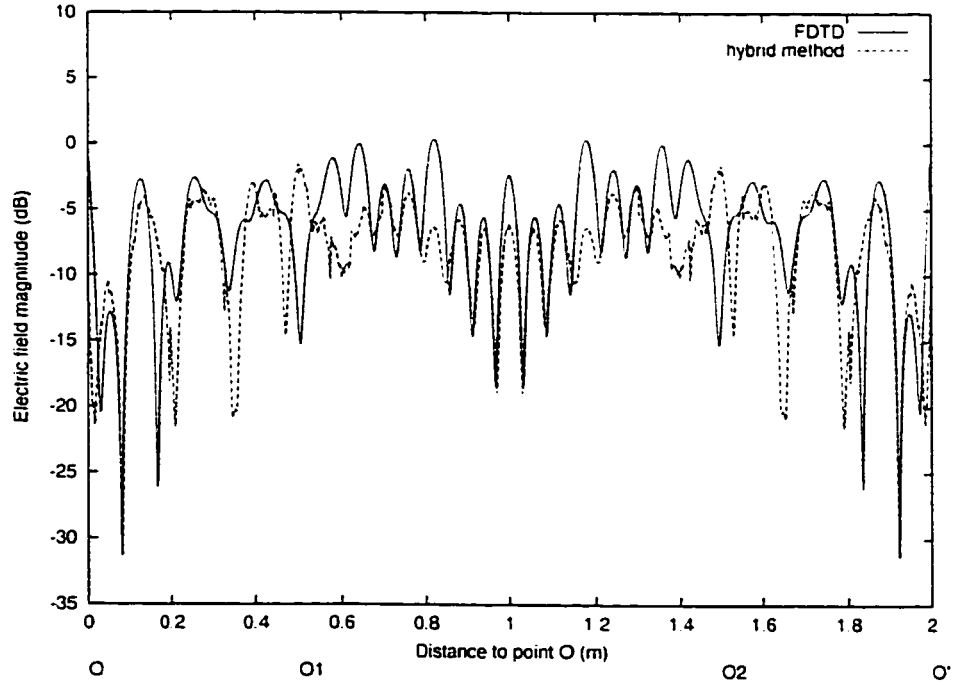

Fig. 4.11 Electric field distributions along OO' of Fig. 4.7 obtained by the hybrid method and FDTD method for the case of plane wave incidence.

Some discrepancies between the two curves in Fig. 4.11 can be observed, especially close to O_1 and O_2. It is speculated that the error is caused by the approximation in the ray tracing simulation. As explained in Chapter 2, diffracted rays by the edges of the metallic slab are not traced further. Therefore, reflection of the diffracted rays by walls and higher-order diffractions are not included in the results by the hybrid method. Furthermore, approximate treatment of the finite length of the exterior wall and corners at the two ends of the wall also contributes to the error, as mentioned in section 4.2.

Example B

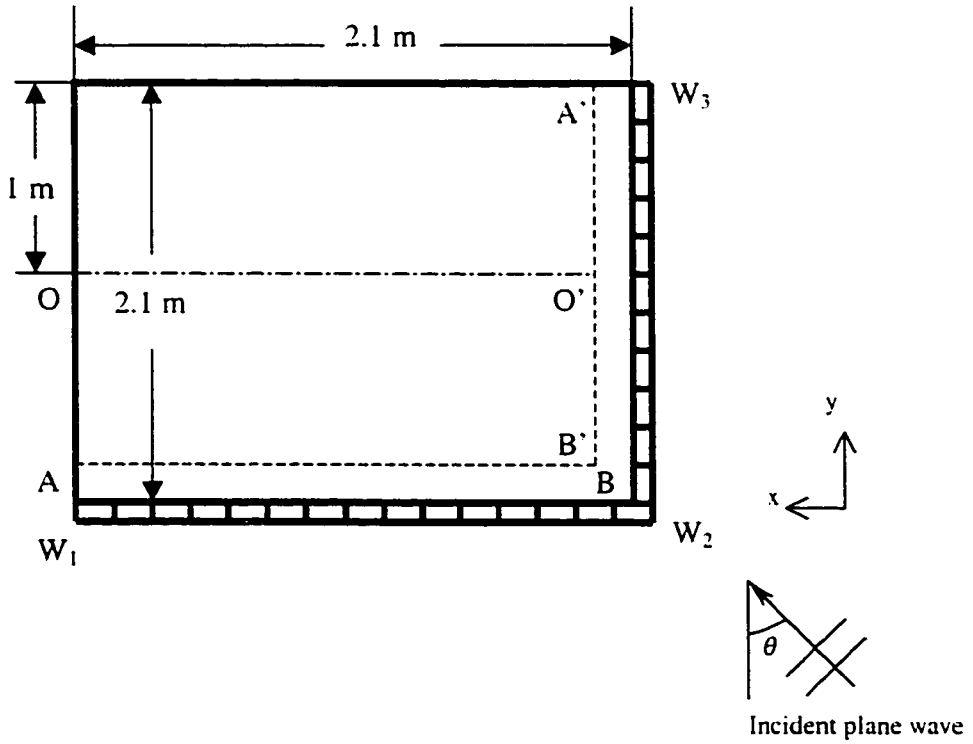

Fig. 4.12 Plane wave incidence on a building at 45°.
Both wall W_1W_2 and W_2W_3 are made of concrete blocks.

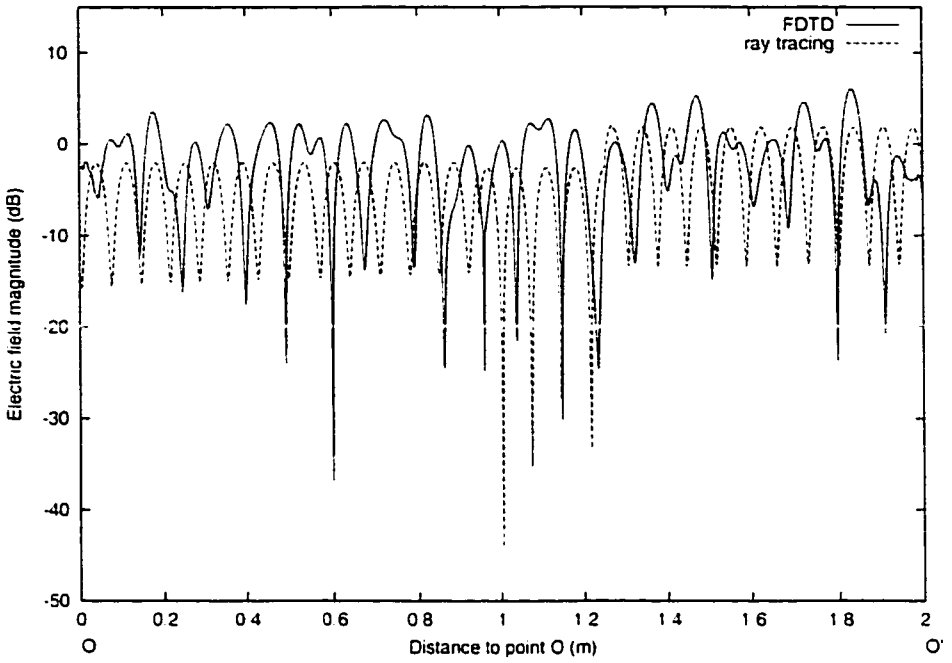

Fig. 4.13 Electric field distributions along OO' of Fig. 4.12 calculated by ray tracing method and FDTD method.

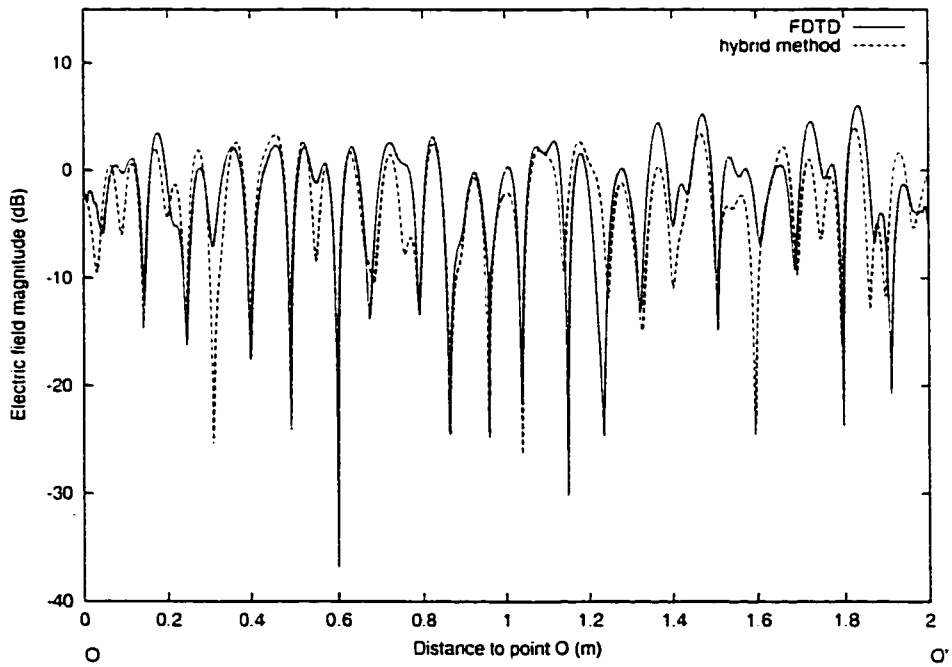

Fig. 4.14 Electric field distributions along OO' of Fig. 4.12 calculated by the hybrid method and FDTD method.

In this example, the structure in Fig. 4.12 is treated. A plane wave is incident upon a building with the size of 2.1m×2.1m at 45°. Both wall W_1W_2 and wall W_2W_3 of the building are made of concrete blocks as shown in Fig. 4.3, while the other two walls are made of homogeneous material. Dielectric constant is assumed to be the same as that in Fig. 4.3(b). The hybrid method is used to study this structure and results will be compared with those by applying FDTD method to the entire building. In the hybrid method, only one cell of the concrete block is treated by FDTD using equations given in section 4.2. where θ equals 45°. Since incident wave comes through both wall W_1W_2 and W_2W_3, tangential electric and magnetic fields along both AB and A'B' in Fig. 4.12 are then determined from the obtained field distribution of each cell of the concrete block wall. B and B' are in fact co-located and used as phase reference in this case. In the next step, rays are sent out from AB and A'B' to cover the indoor area.

Fig. 4.13 shows electric field distributions along OO' of Fig. 4.12 calculated by the ray tracing method and the FDTD method. Compared with the results by FDTD, the ray tracing results have a rms. error of 8.0 dB. Electric field distributions obtained by the hybrid method are shown in Fig. 4.14. It can be seen that results by the hybrid method agree with those by the FDTD method quite well. The rms. error is 4.3 dB. The computation time for the FDTD method is 5 hours while the hybrid method only takes 5 minutes and 56 seconds.

If we change the incident angle θ to 30°, treatment of a cell of the concrete block using FDTD needs to be carried out twice. The reason is that for wall W_1W_2, the incident angle θ of the plane wave equals 30°, while for wall W_2W_3, θ equals 60°. Although B and B' are co-located, the field at B is determined from transmitted field through W_1W_2 and the field at B' is determined from transmitted field through W_2W_3. Therefore, transmitted fields at B and B' may not be the same due to the approximate treatment of the finite size of the walls and omission of the corner effect at W_2. However, numerical results show that effects of these approximations are not significant. Fig. 4.15 compares electric field distributions along OO' of Fig. 4.12 calculated by the hybrid method with results by

FDTD method with the rms. error being 3.6 dB. In Fig. 4.12, ε_r=3 and $tan\delta$=0.01 are assumed for the building material and θ =30°. Note that phases of the fields at B and B' need to be determined using the same reference, i.e. phase of the incident plane wave.

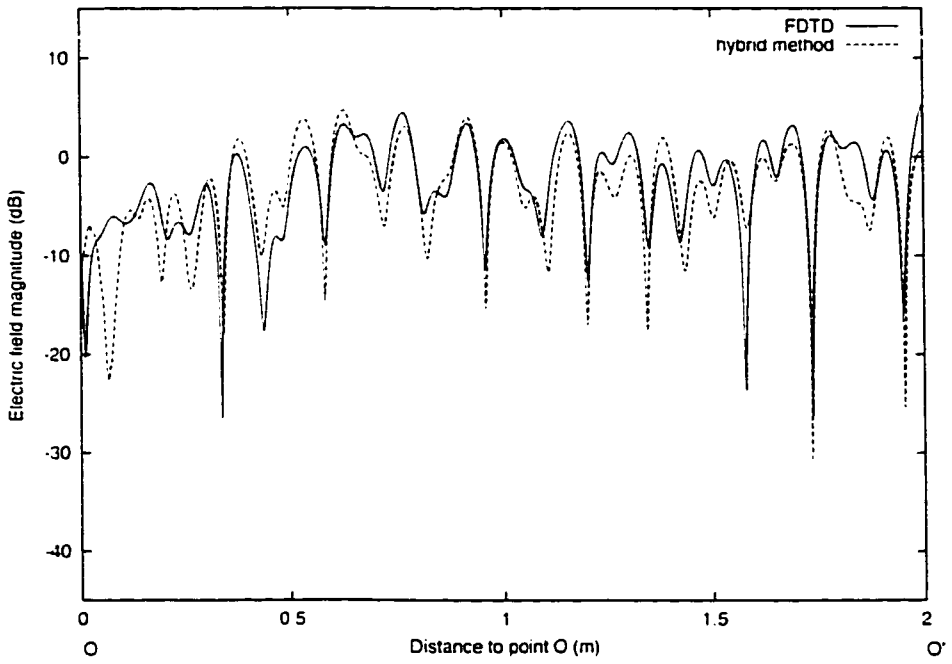

Fig. 4.15 Electric field distributions along OO' of Fig. 4.12 calculated by the hybrid method and FDTD method when θ =30°.

In the case when there are a number of plane waves incident on the building, which is quite common in studying wave penetration from outdoor to indoor, each plane wave can be treated separately using FDTD. Since only one cell of the periodic wall structure is treated by FDTD, the process may not be very time-consuming. Tangential fields along the exterior walls are determined from the summation of the transmitted field of each plane wave through these walls. Higher-order rays are then sent out to cover the area inside the building.

4.4 Summary

A novel method of studying wave penetration through inhomogeneous walls using FDTD and ray tracing is presented in this chapter. Numerical results of the method have been compared and shown to agree very well with those of measurement and those of full wave analysis. Examples are used to show that in the areas where the specular signal is blocked by metallic structure, such as elevator shaft, metal wall, etc., the ray tracing method is not satisfactory. However, the proposed method can accurately predict signal coverage by taking into account the scattered fields by the inhomogeneity inside the walls. Furthermore, the method does not add much to computational complexity, especially when the wall structure is periodic and incident signals are plane waves. Besides outdoor-indoor coupling, the method can also be applied to inter-floor coupling or inter-room coupling, depending on the specific environment and radio propagation mechanisms.

So far, we have studied signal coverage or path loss inside buildings using proposed channel modeling methods. They can also be applied in resolving various fast fading related issues in indoor wireless communications, such as probability distributions of the field envelope, diversity techniques and channel parameters, which will be discussed in the following chapter.

Chapter 5

Applications in the Small-Scale Multipath Channel Modeling

In the indoor environment, the electromagnetic waves travel along different paths of varying lengths due to multiple reflections or scattering from various objects. As the receiver moves over very small distances, e.g. a few wavelengths or even a fraction of a wavelength, the interaction between these waves causes the received signal strength to fluctuate rapidly giving rise to small-scale fading. As the receiver moves away from the transmitter over much larger distances, the local average received signal will gradually decrease. Propagation models have traditionally focused on predicting the average received signal strength over large transmitter-receiver separation distance. In this chapter, developed channel modeling methods will be applied for analyzing various small-scale fading related issues in indoor wireless communications.

There are three most important small-scale fading effects created by multipath [Rap96]: rapid changes in signal strength over a small travel distance or time interval,

random frequency modulation due to varying Doppler shifts on different multipath signals, and time dispersion (echoes) caused by multipath propagation delays. Applications of the developed site-specific channel modeling method in the simulation of all of these three effects will be discussed in this chapter.

5.1 Probability Distribution of Field Strength

By using ray tracing method or the hybrid technique of combining ray tracing and FDTD methods, field distribution in the interested area can be calculated. From the field distribution, one can obtain the probability distribution of field strength. Such statistical analysis gives information of probability of received signal level being above a threshold for good quality of service and is important for designing radio links. Two examples are used to demonstrate the simulation approach.

The first example is the two-room structure studied in Chapter 3, as shown in Fig. 3.10. A transmitter located in the left-side room. Electric field distribution inside the right-side room was computed by three methods: FDTD method, the proposed hybrid method and the ray tracing method. In total, 8800 (80×110) locations inside the right-side room are calculated by the three methods. First, from electric field distribution obtained by FDTD method, the average field power over the 8800 locations in the right-side room is calculated. Next field value at each location is normalized to the average power. The cumulative distribution of the normalized signal level is then computed and shown in Fig. 5.1 by the solid line. It can be read from Fig. 5.1 that 1% probability corresponds to -17 dB, which means that there is 1% probability that the received signal level is 17 dB below the average signal value. Field distributions obtained by ray tracing method and the hybrid method are processed in the same way and cumulative distributions are also shown in Fig. 5.1. As expected, the hybrid method provides an excellent estimation to the cumulative distribution of signal level.

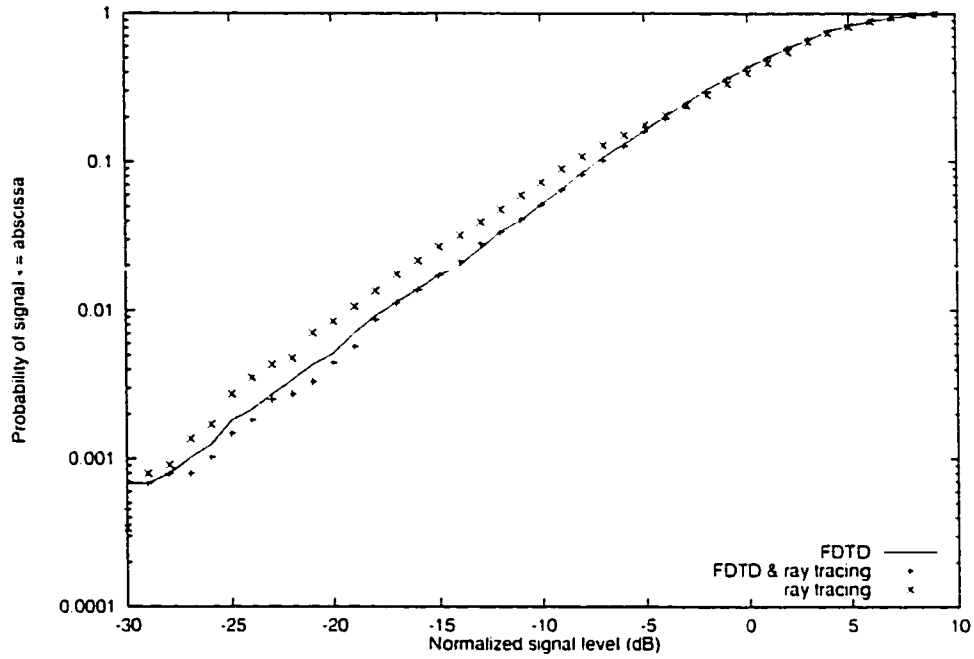

Fig. 5.1 The cumulative distribution of the normalized signal level in the right-side room of Fig. 3.10.

In the second example, a comparison is made between simulation and measurement reported in [Hor86] for wave penetration through an exterior wall covered with metal-framed window at 1.29 GHz, which is described in detail in Chapter 3. Fig. 3.15 shows the side view and top view of the of the empty room where the measurement was taken. The cumulative distributions of the measured signal level in the room indicated a good approximation to the Rayleigh distribution.

The problem has been treated in Chapter 3 using the hybrid method. Fig. 5.2 shows cumulative distributions of normalized signal level obtained from the hybrid method for two courses along O_1O_2 in Fig. 3.15 when d=4λ and d=5λ. A close resemblance to the Rayleigh distribution can be observed, which conforms to the results derived from measurements in [Hor86].

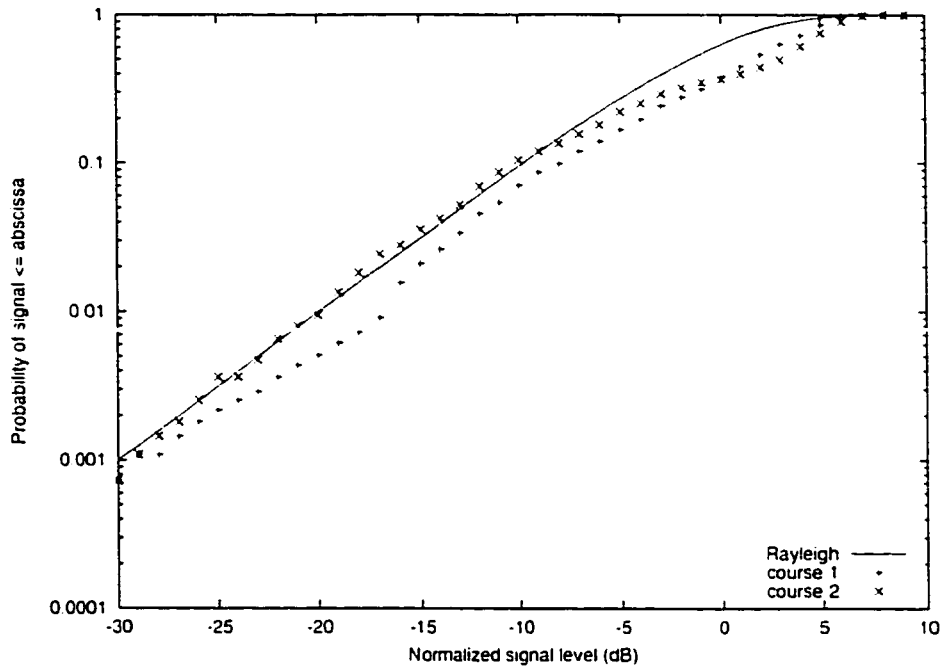

Fig. 5.2 Cumulative distributions of normalized signal level obtained from the hybrid method for two courses along O_1O_2 in Fig. 3.15 when d=4λ (course 1) and d=5λ (course 2).

5.2 Simulation of Diversity Techniques

It can be seen from Fig 5.1 and Fig 5.2 that due to the constructive and destructive effects of multipath waves summing at various points in space, a moving receiver can pass through several fades over a small distance. In a more serious case, a receiver may stop at a particular location at which the receiver signal is in a deep fade. Maintaining good communications can then become very difficult.

Such severe small-scale fading effects are best minimized by diversity techniques. For example, antenna space diversity can prevent deep fading nulls. When two separated receiving antennas are uses, the likelihood of the received signals by both antennas are in deep null is much less than using just one receiving antenna. Antennas with different polarization can be used for the same purpose. Frequency hopping can also be used as a

means for mitigating against fading. Packets that are not correctly received because of deep signal fading can be retransmitted at different frequency, provided that the frequency difference is great enough so that signals are affected differently by the multipath channel.

By studying statistical properties of radio wave propagation between a mobile and a base station, we will be able to predict the performance of different diversity systems. We will evaluate performance of space, frequency and polarization diversities in indoor environment using 2D hybrid method of combining ray tracing and FDTD methods and 3D ray tracing method. The methods avoid making assumptions of distribution of incident wave amplitude, phase or angle, as required in statistical models. Furthermore, the proposed methods have the strength of relating radio wave propagation to the physical layout of the specific communication environment. Simulation results at 900MHz are presented and compared with the reported experimental results [Lem91][Tod92].

5.2.1 Simulation method

To facilitate comparison with experimental results, simulation is made in the building shown in Fig. 5.3, which is the similar type of indoor environment to the one in [Lem91]. Building material is assumed to be homogeneous with $\varepsilon_r = 8$ and $tan\delta = 0.015$. Transmitter is located at Tx.

The 2D hybrid method of combining ray tracing and FDTD is used to study frequency and space diversity techniques. Rays are sent out from the transmitter and traced through the environment. The regions of interest in the simulation area are enclosed by virtual boxes and denoted by the shaded areas in Fig. 5.3. Rays intersecting these boxes are propagated into the regions of interest by the FDTD propagator, and field amplitude at each point is obtained. When a receiver moves within the box along any

route, such as a circle in [Lem91], the variations in the received signal level are captured. The fading statistics can then be obtained.

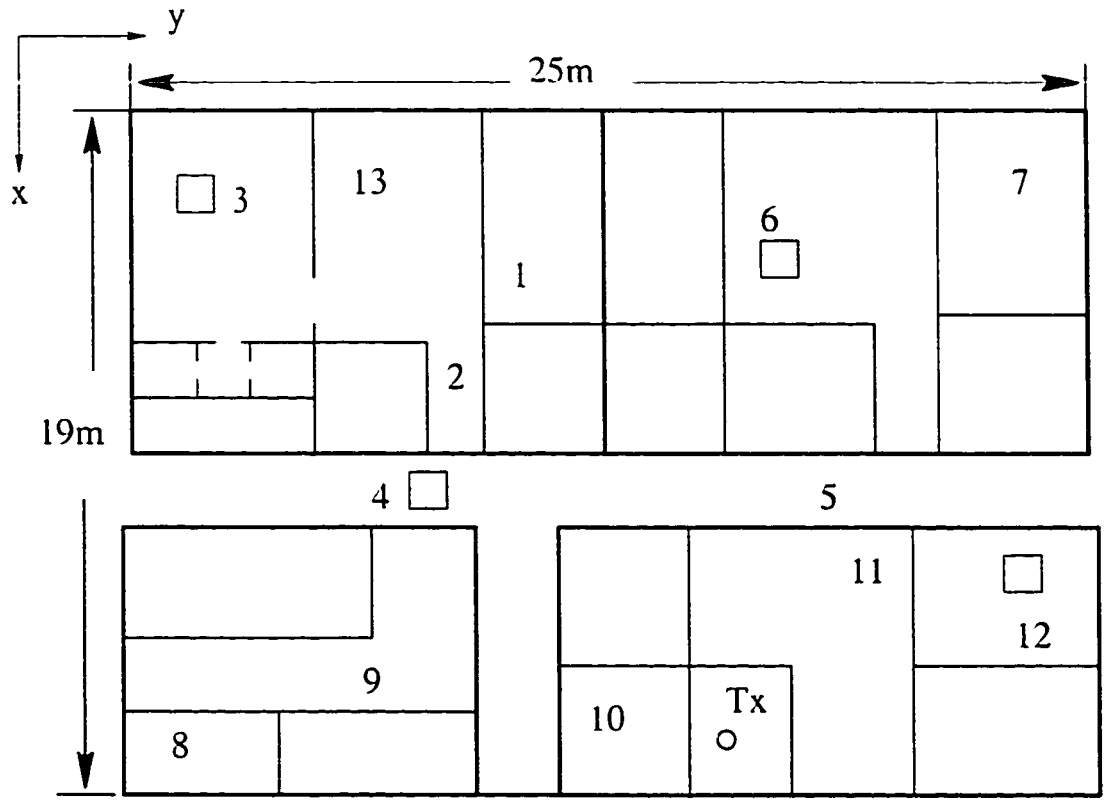

Fig. 5.3 An indoor environment with the transmitter located at Tx. Shaded areas are for frequency and space diversity simulation. Location 1~13 are the receiver locations for polarization diversity simulation.

Selection combining is assumed in the following simulation, which means the best signal among all of the signals received from different diversity branches is always selected. Only two diversity branches are considered. The receiver with diversity system is moved within the shaded areas in Fig. 5.3. The size of each area is $4\lambda \times 4\lambda$, where λ is the wavelength at f_0 = 900 MHz. Space resolution of FDTD is set to be 40 cells per

wavelength, so that there are totally 160×160 receiver locations in each shaded area. At each receiver location, we use γ_1 and γ_2 to denote received signals at the two diversity branches, respectively, which are normalized by the local mean power of the branch to exclude effect of large scale fading. With selectivity combining of the two branches, the stronger signal level is chosen: $\gamma = \max(\gamma_1, \gamma_2)$. Following the definition in [Lem91], for any arbitrary level x, the simultaneous fading probability $P_r(\gamma<x) = P_r(\gamma_1<x, \gamma_2<x)$. The simultaneous fading probability is the smallest if γ_1 and γ_2 are independent, i.e. $P_r(\gamma<x)$ is simply the product of two individual fading probabilities. However, if the two branches are correlated, the diversity gain is reduced. The correlation coefficient between the received signals of the two diversity branches is calculated as follows,

$$\rho = \frac{\sum_{m=1}^{M}\left(\gamma_1^m \gamma_2^m\right)}{\sqrt{\sum_{m=1}^{M}\left(\gamma_1^m\right)^2}\sqrt{\sum_{m=1}^{M}\left(\gamma_2^m\right)^2}}$$

where γ_i^m is the received signal level on the ith (i=1,2) diversity branch at mth receiver location and is normalized to the local mean signal level. To get the global average of the correlation coefficient, all of the four shaded areas in Fig. 5.3 are considered, which makes the total available number of samples, M, to be 4×160×160.

For polarization diversity, 3D ray tracing is used. As shown in Fig. 5.3, transmitter is still located at Tx, which is a dipole antenna with a sloping angle of θ to the z axis as shown in Fig. 5.4(a). The receiving polarization diversity antenna is shown in Fig. 5.4(b), which consists of a vertically polarized dipole antenna and a horizontally polarized dipole antenna. The receiver locations are marked on Fig. 5.3, No.1~No.13. At each of these 13 locations, the receiving antenna is moved within a 4λ×4λ area and 144 samples are taken. Signal levels on the two receiver branches are different, which is described by the Cross Polar Discrimination, XPD. To study diversity performance, signal amplitudes were

normalized to the average received power of the stronger branch at the same location, which in this environment is the vertical antenna.

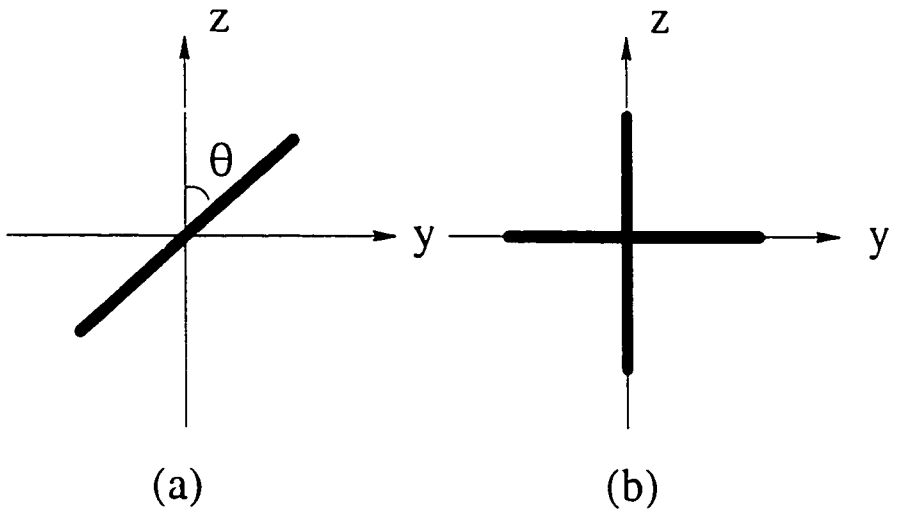

Fig. 5.4 (a) Transmitting dipole antenna orientation and
(b) polarization of the receiving antennas for polarization diversity simulation.

5.2.2 Simulation results

For frequency diversity, γ_1 is the received signal at f_0, and γ_2 is the received signal at $f_0+\Delta f$. Frequency spacings (Δf) of 1, 5, 10, 15 and 20 MHz were calculated, and the cumulative probabilities of simultaneous fading events for different frequency spacings are shown in Fig. 5.5. Since signal levels are normalized to the local averaged received power, the cumulative probabilities of simultaneous fading of each shaded area are averaged and plotted on the same graph. Diversity gains can be read from Fig. 5.5, e.g. at 99% reliability level (1% probability that the received signal is less than the given level

.r), with 5 MHz frequency spacing, there is 8 dB diversity gain comparing to individual receiver channel. Fig. 5.6 shows the measurement results reported in [Lem91]. A very good agreement between the simulation results and the experimental results can be observed. The solid line in Fig. 5.6 illustrates the theoretical cumulative probability of simultaneous fading when the two normalized channels are uncorrelated. It is clear from the figures that a 5 MHz separation between the two tones is needed for the two signals to be substantially uncorrelated.

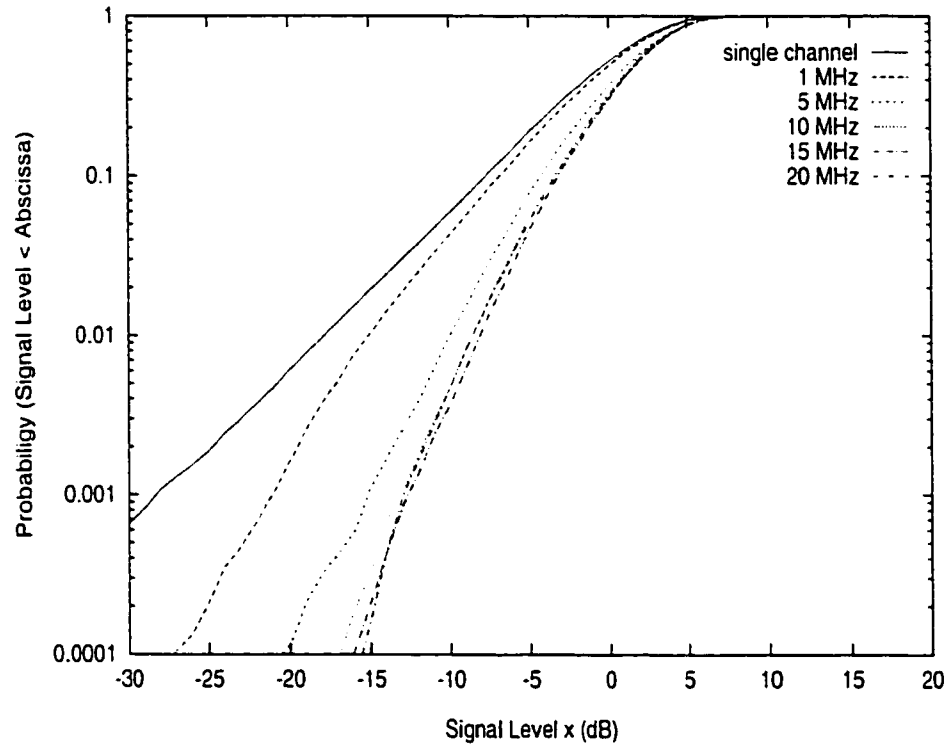

Fig. 5.5 Frequency diversity performance when two frequencies are separated by 1, 5, 10, 15 and 20 MHz.

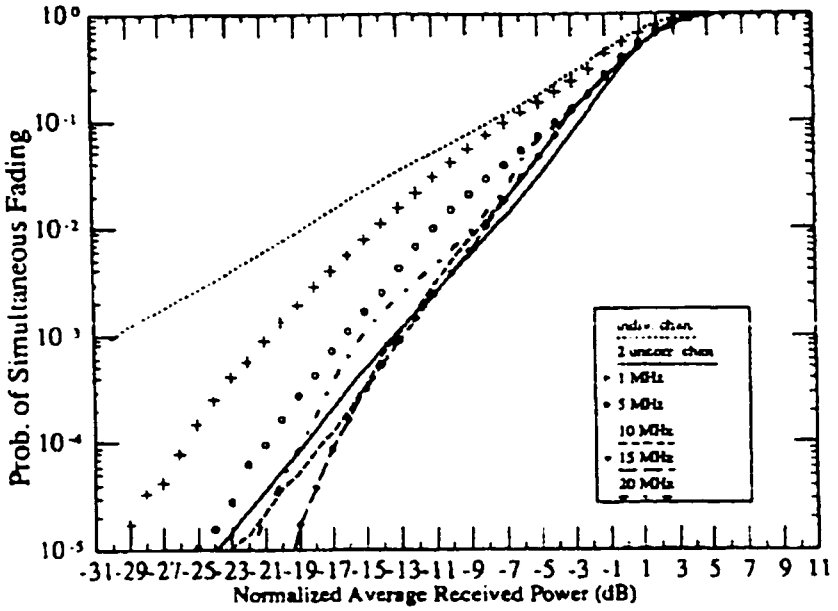

Fig. 5.6 Measurement results of frequency diversity performance when two frequencies are separated by 1, 5, 10, 15 and 20 MHz [Lem91].

Table 5.1 shows diversity gains at 99% reliability level and correlation coefficients between two branches for different frequency spacings. Measurement results of diversity gains are approximate reading from the experimental curves in Fig. 5.6. Global average correlation coefficients between two channels are less than 0.5 when frequency spacing is larger than 5 MHz and a desirable diversity gain may be obtained, as shown in table 5.1. This observation is consistent with the reported measurement at 1.7 GHz in [Tod92]. It can also be concluded that a separation greater than 10 MHz does not affect the results significantly.

Table 5.1 Diversity gains at 99% reliability level and correlation coefficients between two branches for frequency diversity

Δf (MHz)	Diversity gain (dB)		ρ
	Simulation	Measurement [Lem91]	
1	3	4.5	0.942
5	8	7.5	0.439
10	9.5	10.5	0.262
15	10	10.5	0.149
20	9.5	10	0.189

In the case of space diversity, γ_1 and γ_2 represent signals received by two spaced receiving antennas. Fig. 5.7 illustrates the cumulative probability of simultaneous fading for different lengths of separation (Δl) between the two antennas. Fig. 5.8 shows the measurement results reported in [Lem91]. Again, a very good agreement between simulation and measurement can be seen. Table 5.2 shows diversity gains at 99% reliability level and correlation coefficients between two branches for different space separations. Measurement results of diversity gains are approximate reading from the experimental curves in Fig. 5.8. For all space separations simulated, correlation coefficients are very low and diversity gain of about 10 dB at 99% reliability level can be obtained at $1/4\lambda$ separation. Although measurement values are not available at $1/4\lambda$ and $1/2\lambda$ at 900 MHz, this observation agrees with the measurement at 1.7 GHz in [Tod92].

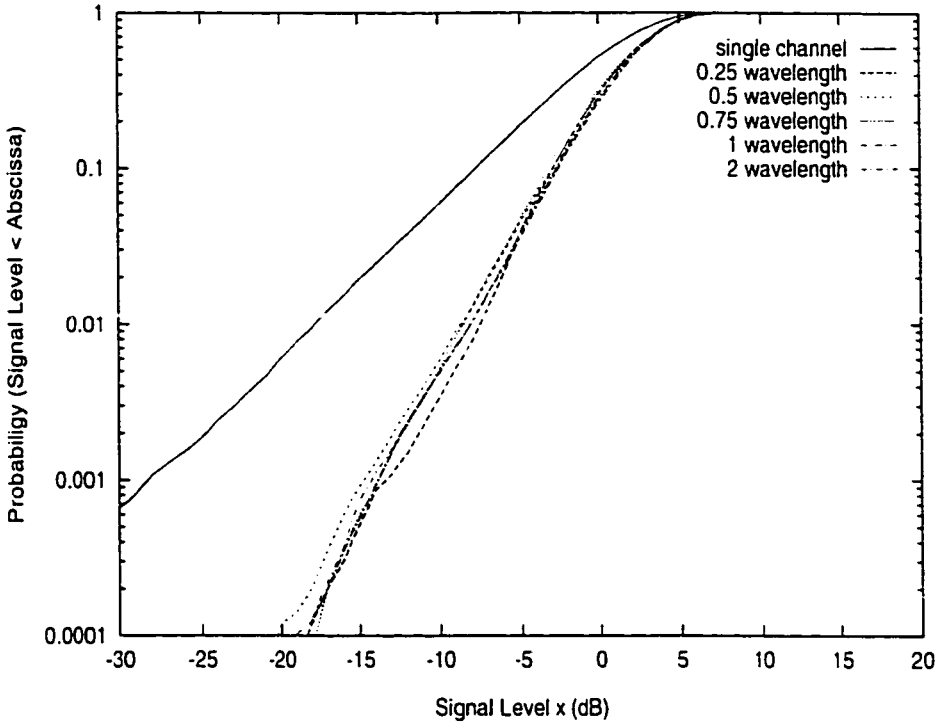

Fig. 5.7 Space diversity performance when two receiving antennas are separated by 0.25λ, 0.5λ, 0.75λ, λ and 2λ.

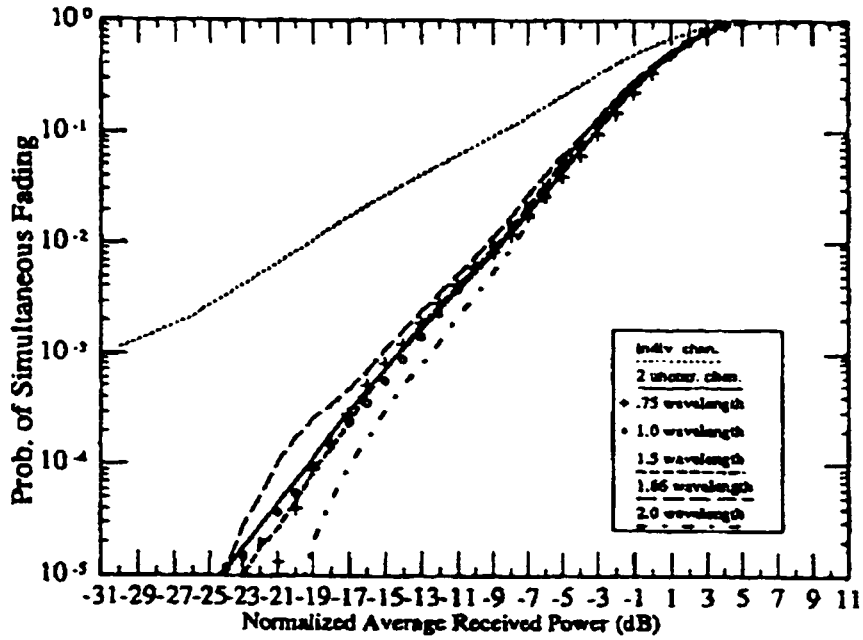

Fig. 5.8 Measurement results of space diversity performance when two receiving antennas are separated by 0.75λ, λ, 1.5λ, 1.66λ and 2λ [Lem91].

Table 5.2 Diversity gains at 99% reliability level and correlation coefficients between two branches for space diversity

Δl	Diversity gain (dB)		ρ
	Simulation	Measurement [Lem91]	
1/4λ	10.5	N/A	0.148
1/2λ	9.5	N/A	0.149
3/4λ	9.5	10	0.247
λ	10	10	0.060

For polarization diversity, first a vertically polarized transmitting antenna was simulated. It was found that the polarization of the transmitted signal was very well preserved with XPD 20 dB high, while the measured data in [Lem91] shows that the difference in power between the co-polarized and cross-polarized signals is typically 3 dB. The difference may be caused by the fact that the measurement in [Lem91] was made in a complex university work environment, while our simulated environment is much simpler and "unfurnished". Diversity performance is dramatically degraded with such a high XPD because the cross-polarized branch makes no contribution. Next the transmitting antenna was rotated so that the sloping angle θ in Fig. 5.4(a) became 45°. It can be seen from Fig. 5.9 that diversity gain is 7 dB at 99% reliability level using polarization diversity. Correlation coefficient between vertical and horizontal antenna branches is about 0.22.

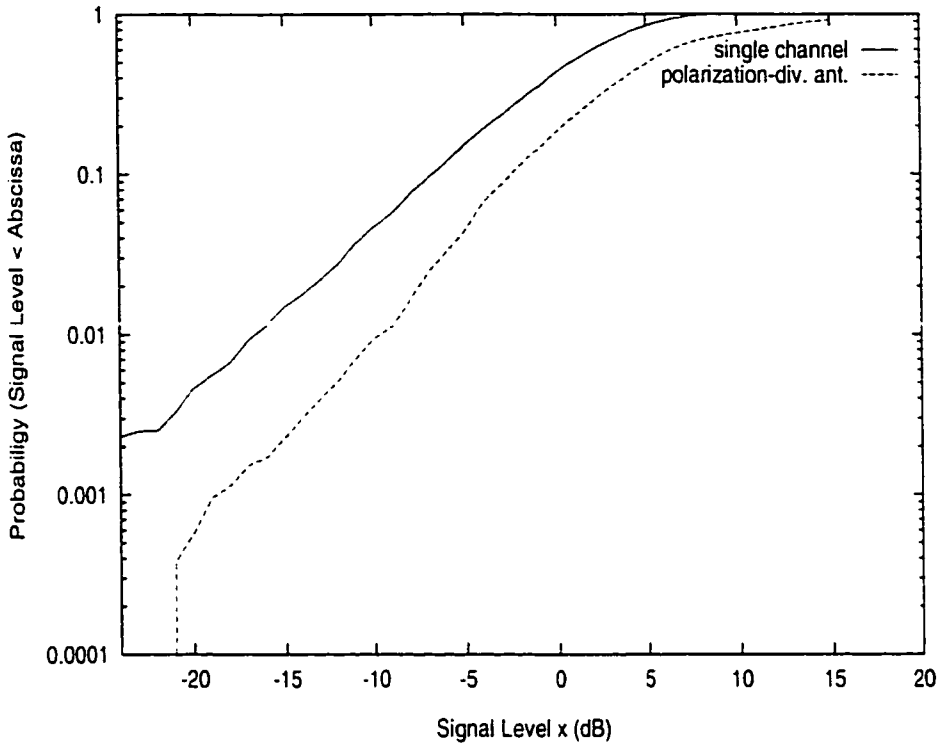

Fig. 5.9 Polarization diversity: signal received by two cross polarized antennas.

5.3 Doppler Spread

Due to the relative motion between the transmitter and the receiver, each multipath wave experiences an apparent shift in frequency, which gives rise to Doppler shifts. The width of the distribution of Doppler shifts is defined as the Doppler spread. It is a parameter that describes the time varying nature of the channel. The Doppler spread is important in determining the minimum signaling rate allowable for coherent demodulation and minimum adaptation rate for an adaptive receiver [How90]. For the indoor radio channel, the multipath characteristics are static at any one location until some movement occurs and causes Doppler spreading.

In this section, the developed channel modeling techniques will be used to simulate the temporal variation caused by human-induced motion of the communication equipment, on the otherwise static indoor radio channel. Simulation results will be compared with measurement results reported in [How90].

The measurement in [How90] was taken in an electronics laboratory at 910 MHz to study Doppler spread of the indoor radio channel caused by traffic and local movements of the communication equipment. For the latter case, measurements were taken with small cyclic movement of the communication equipment. To simulate these measurements, the building shown in Fig. 5.3 is used. Electric field distributions within the FDTD domain are known after using the hybrid technique to treat the indoor environment. Therefore, the time response can be readily found out when the receiver is moved at a given speed within the FDTD domain. Fig. 5.10 shows the time response of moving receiver at people's walking speed (1.33 m/s) within the shaded area located in the corridor in Fig. 5.3.

The measurements and simulations give the response $H(f_0;t)$ of the indoor radio channel to an unmodulated sine wave of frequency f_0. In the analysis of radar signals, the maximum Doppler shift is defined to be $2v_m f_0/c$[How90], where v_m is the velocity of movement. If we use this equation to approximate the Doppler spread of the indoor radio channel, a person walking at 1.33 m/s will produce a Doppler spread of 8 Hz when the transmission frequency is 910 MHz. However, the exact Doppler spreads are found out through the measured or simulated response $H(f_0;t)$. The Doppler power spectrum $V_F(\lambda)$ is the Fourier transform of the complex autocorrelation function of $H(f_0;t)$, i.e. $V_F(\lambda) = |H(f_0;\lambda)|^2$, where $H(f_0;\lambda) = \int H(f_0;t)\exp(-j2\pi\lambda t)dt$ [How90]. The Doppler spread is the range of frequencies λ over which the Doppler power spectrum $V_F(\lambda)$ is essentially nonzero.

The Doppler power spectrum of response in Fig. 5.10 is plotted in Fig. 5.11. The Doppler spread is then found to be 4.5 Hz, which is very close to the reported Doppler spread of 4.7-5.2 Hz in [How90].

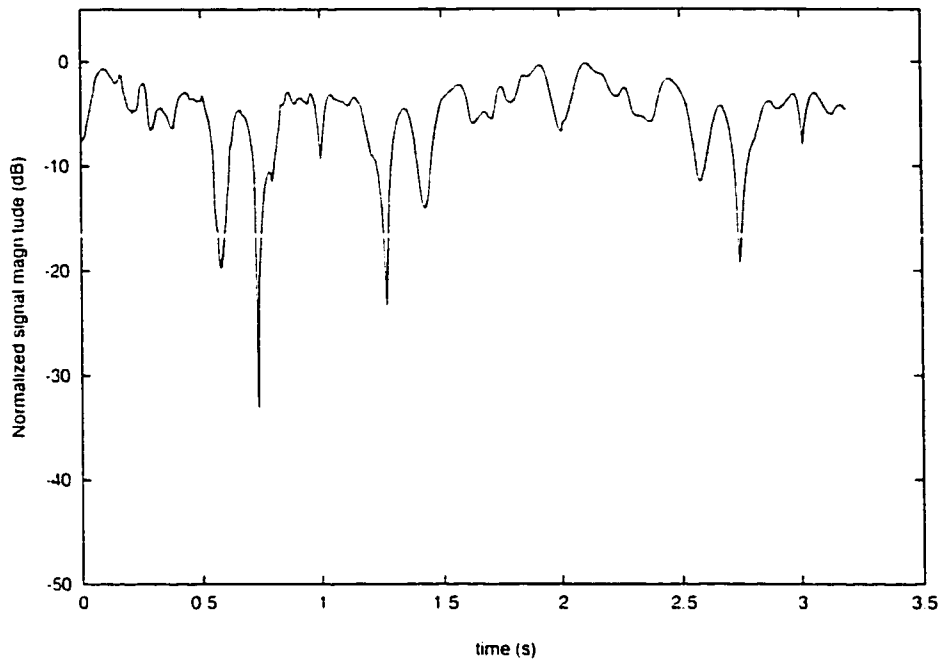

Fig. 5.10 Time response of moving receiver at 3 mile/h (1.33/s).

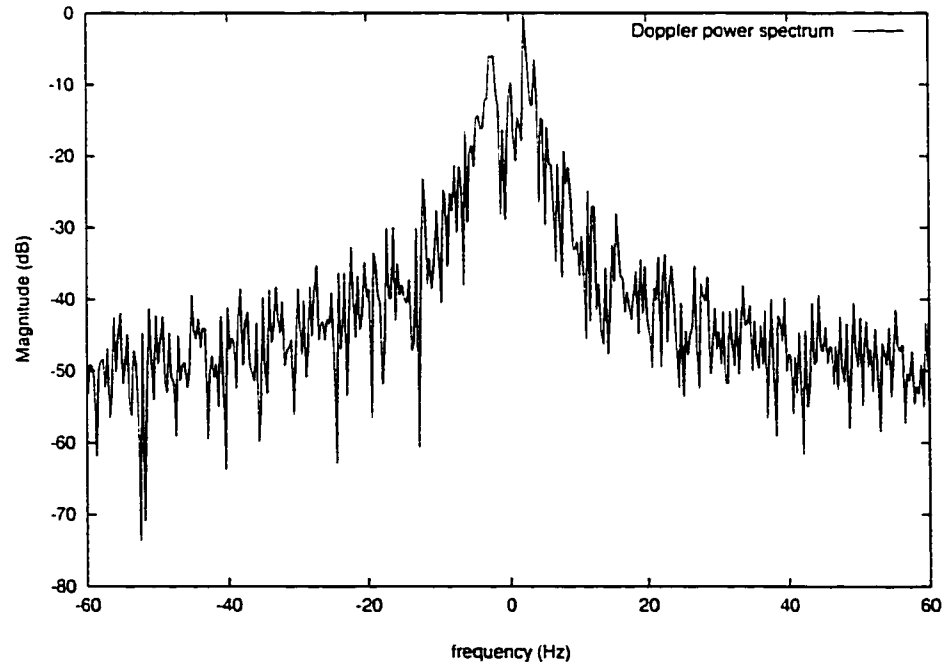

Fig. 5.11 Doppler power spectrum.

5.4 Impulse Response and Channel Parameters

The small-scale variations of a radio signal can be directly related to the impulse response of the radio channel. The impulse response is a wide band channel characterization and contains all information necessary to simulate or analyze any type of radio transmission through the channel. It may be used to predict and compare the performance of many different communication systems and transmission bandwidths for a particular mobile channel condition.

When measuring or predicting channel impulse response, a probing pulse $p(t)$ is sent out at the transmitter. The pulse response can be thought of as the sum of individual pulses arriving along ray paths with field amplitude a_k, phase shift θ_k and delay time τ_k. The received signal can therefore be written as [Kim96]

$$x(t) = \sum_{k=0} a_k p[t - \tau_k] e^{j[\theta_k(t) - \omega\tau_k]} e^{j\omega t} \tag{5.1}$$

where ω is the angular carrier frequency. Power delay profile $s(t)$ can then be obtained, since $s(t) = |x(t)|^2$.

Many multipath channel parameters are derived from the power delay profile. First, the time dispersive properties of wide band multipath channels are most commonly quantified by their mean excess delay ($\bar{\tau}$) and rms delay spread (σ), which can be determined from a power delay profile. The mean excess delay is defined as

$$\bar{\tau} = \frac{\int_{-\infty}^{\infty} t s(t) dt}{\int_{-\infty}^{\infty} s(t) dt} \tag{5.2}$$

With the expression for the mean excess delay, the rms delay spread is found from

$$\sigma^2 = \frac{\int_{-\infty}^{\infty} (t-\bar{\tau})^2 s(t)dt}{\int_{-\infty}^{\infty} s(t)dt} \tag{5.3}$$

The rms delay spread is a parameter used to determine data rates so as to avoid an intersymbol interference (ISI).

The power delay profile and magnitude frequency response of a radio channel are related through the Fourier transform. It is therefore possible to obtain an equivalent description of the channel in the frequency domain using its frequency response characteristics. Analogous to the delay spread parameters in the time domain, coherence bandwidth is used to characterize the channel in the frequency domain. It is a measure of the range of frequencies over which the channel passes all spectral components with approximately equal gain and linear phase. In other words, coherence bandwidth is the range of frequencies over which two frequency components have a strong potential for amplitude correlation. Two sinusoids with frequency separation greater than coherence bandwidth are affected quite differently by the channel. The rms delay spread and coherence bandwidth are inversely proportional to one another. However, an exact relationship between coherence bandwidth and rms delay spread does not exist. Their exact relationship is a function of the exact multipath structure. Following the definition given in [Kim96], the frequency auto correlation function is found from the local average power delay profile $\langle s(t) \rangle$ using the following relationship:

$$R_H(\Delta f) = \int_{-\infty}^{\infty} \langle s(t) \rangle e^{-j2\pi\Delta f t} dt \tag{5.4}$$

The coherence bandwidth is then defined as the full width of Δf at half the maximum of $R_H(\Delta f)$.

In this section, the developed deterministic models will be applied for wide band simulation. Examples will be used to demonstrate the approach of obtaining power delay profile and multipath channel parameters.

5.4.1 Wide band simulation using ray tracing

Prediction of channel impulse response with ray tracing is carried out in frequency domain. To this end, a probing pulse $p(t)$ modulated on the carrier frequency f_0 is sent out from the transmitter. $p(t)$ is assumed to be a Gaussian pulse with the envelope function of

$$p(t) = \exp\left(-\frac{t}{w}\right)^2$$

where w is the pulse-width parameter. Let $P(f)$ be the Fourier transform of $p(t)$, where $f=f_0 \pm n\Delta f$ (n=0,1, ..., N/2) and $N\Delta f$ is the simulation bandwidth. At each frequency $f=f_0+n\Delta f$, the received signal magnitude and phase are found using ray tracing. It is similar to the measurement of the channel impulse response in the frequency domain by scanning a particular frequency band centered on the carrier by stepping through discrete frequencies. Then, time response $x(t)$ or power delay profile $s(t)$ can be obtained through inverse Fourier transform of the frequency response of the radio channel. Note that the frequency step Δf needs to be small enough so that the time delay range $T=1/\Delta f$ is large enough to include all multipath components with substantial power. However, if Δf is too small or N is too large for a given bandwidth, the computation time increases subsequently.

After running ray tracing process at the center frequency, rays that intersect with the receiver will be stored. Therefore, it is not necessary to rerun the process at each frequency, which significantly reduces computation time.

To validate the method, comparison is made between simulation results and the measurement results reported by Kim, Bertoni and Stern [Kim96]. Impulse response measurements were made in an engineering building with typical office and laboratory areas. Fig. 5.12 shows the layout of the building whose size is 60.5m × 44 m. The ceiling is 2.9 m above the floor. The transmitter was located near center of the main cubicle area

at a height of 2.5 m. The receiving antenna height was 1.42 m above the floor, which is typical of handheld mobile radio units in a wireless LAN environment. The measurements employed a 2.4 GHz carrier that was modulated by repetitive pulses with 3 dB pulse duration of 3.2 ns. From measured data, the impulse response parameters were obtained and the coherence bandwidth was calculated from the power delay profiles.

Fig. 5.13(a) and (b) show the measured power delay profiles for the site "east1" in the building as shown in Fig. 5.12. The receiving antenna was located at a distance of 7.32 m from the transmitter for the measurement of Fig. 5.13(a). Then the receiver was moved two wavelengths along the straight line parallel to the direct line between the transmitter and receiver and the power delay profile in Fig. 5.13(b) was measured.

The simulation results by ray tracing are shown in Fig. 5.14(a) and (b). The pulse peak power has been normalized to the measured pulse power. A time shift in the simulation results can be observed. The reason is that the time origin of the measured power delay profile is taken to be at the rising edge of the first perceptible pulse, while the time origin of the simulation results represents the starting time of the transmitted pulse. Therefore, the first pulse arrives at delay time of 25 ns as seen in Fig. 5.14(a), which correctly predicts the time traveled by the direct ray from the transmitter to the receiver. The discrete lines in Fig. 5.14 represent each multipath component calculated at the center frequency. The first line is the direct path, the second one corresponds to the ceiling reflected paths, and the third is the floor reflected path.

A good agreement between the simulation and measurement results can be observed. In Fig. 5.13(a) and Fig. 5.14(a), the first dominant pulse appears to arise from the signal traveling over a single path. In fact, it is composed of four "subpaths", in stead of two "subpaths" as concluded in [Kim96], as can be seen from the discrete lines in Fig. 5.14(a). It splits into two pulses in Fig. 5.13(b) and Fig. 5.14(b) when the receiver is moved two wavelengths away. The strengths of the split pulses are weaker than that of the merged pulse in Fig. 5.13(a) and Fig. 5.14(a), implying the pulses from subpaths interfere constructively.

A third pulse, evident in Fig. 5.13(b) near 10 ns, is negligible in Fig. 5.13(a). Similar phenomenon is seen in the simulation results in Fig. 5.14, although the signal strength of this pulse is not as strong as the measured pulse. Conversely, the strong echo at 20 ns from the first pulse in Fig. 5.13(a) is weaker than other scattered pulses in Fig. 5.13(b), which agrees with results in Fig. 5.14. There results imply that even for a line of sight path to the transmitter, what appear to be individual pulses are actually composed of multipath signals so that the pulse amplitude strongly depends on the phase differences between subpaths, which change as a result of moving the receiver. As pointed out in [Kim96], this observation is contrary to the claim of reference [Rap89] that "multipath components fade very slightly with small movement of the receiver, granting that the first perceptible pulse seldom varies in regard to this small movement". This discrepancy in conclusions drawn from different measurement is a clear demonstration of the site-specific nature of indoor radio channel. The deterministic model gives insight to the mechanisms causing the fast fading phenomenon seen in the received signal.

From the power delay profiles, the impulse response parameters and the coherence bandwidth can be obtained. The average mean excess delay and rms delay spread at site "east1" calculated from measurement data are 29.90 ns and 44.27 ns, respectively [Kim96]. The simulation results are 32.08 ns and 39.32 ns, which agrees with the measurement results quite well.

The Fourier transforms of the measured and predicted average power delay profiles are plotted in Fig. 5.15 and Fig. 5.16. The predicted coherence bandwidth is then found at half the maximum of the frequency auto correlation curve in Fig. 5.16 to be 41 MHz, while the measurement result is 42.62 MHz in [Kim96].

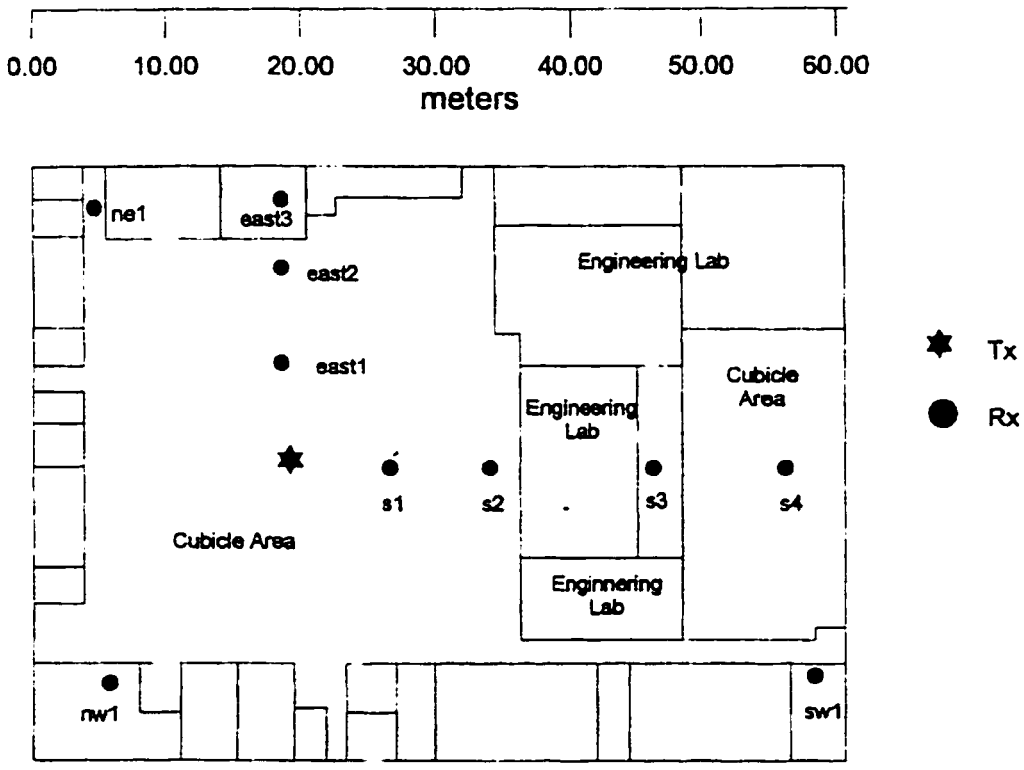

Fig. 5.12 Floor plan of the tested indoor environment [Kim96].

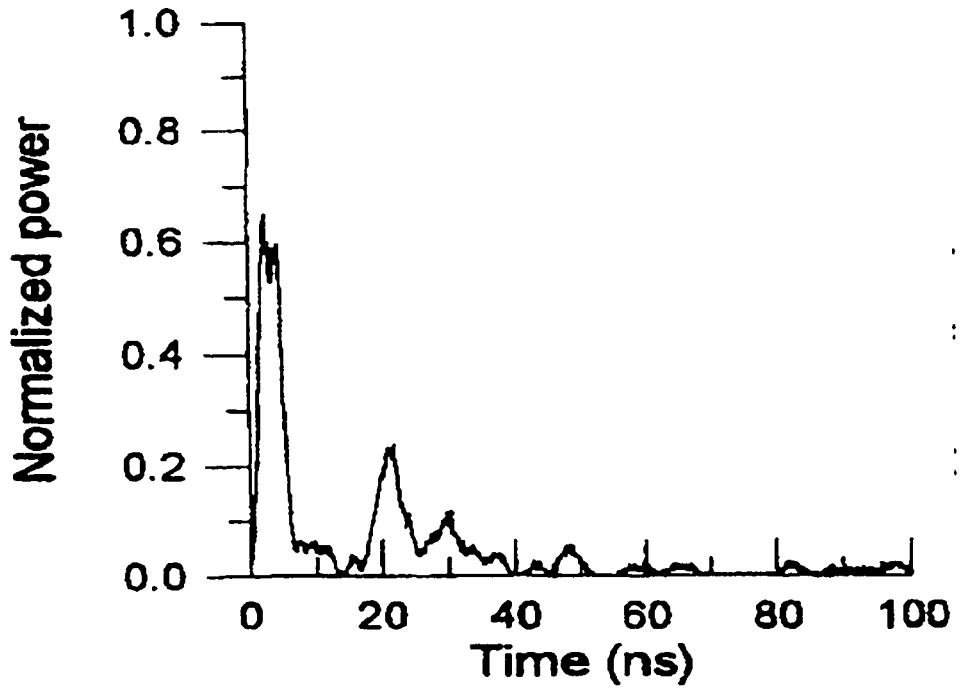

(a)

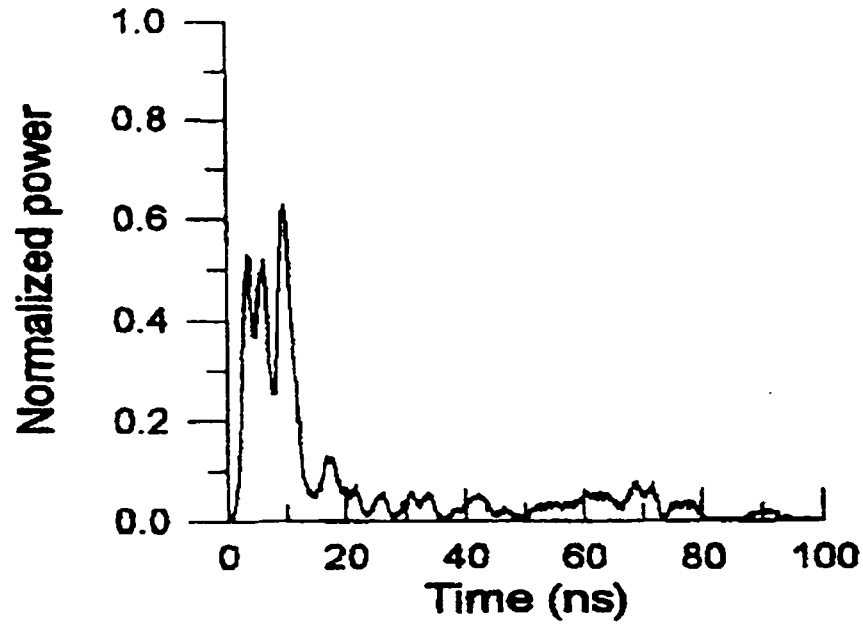

(b)

Fig. 5.13 The measured power delay profiles for the site "east1" in the building shown in Fig. 5.12 [Kim96].

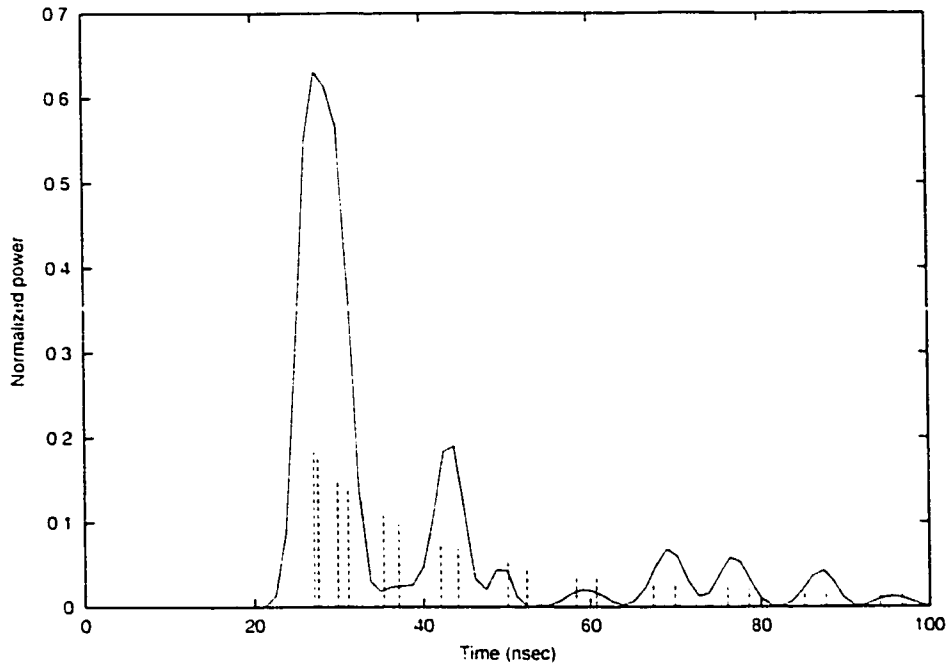

(a)

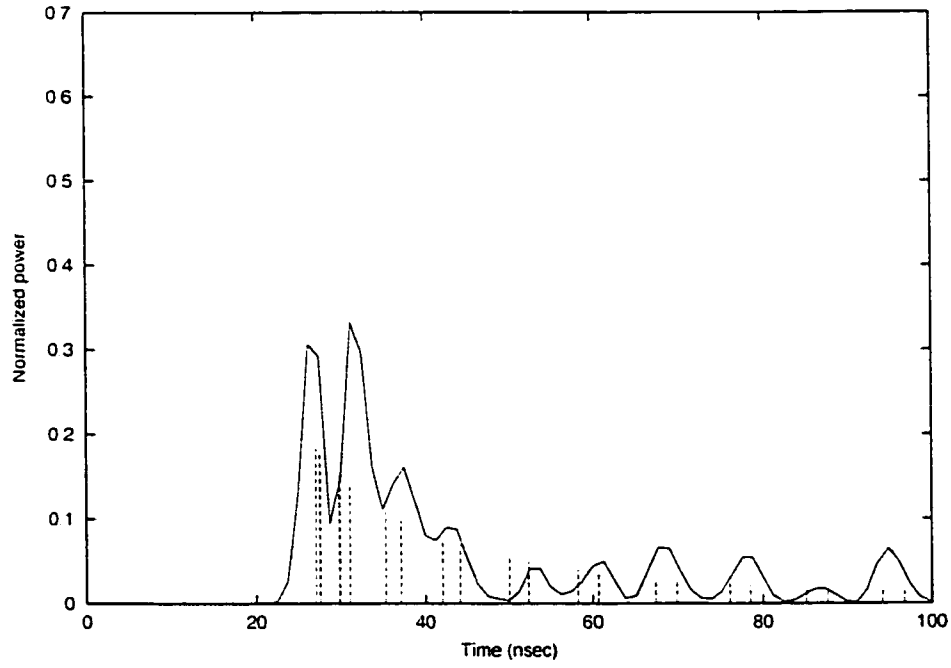

(b)

Fig. 5.14 The simulated power delay profiles for the site "east1" in the building shown in Fig. 5.12.

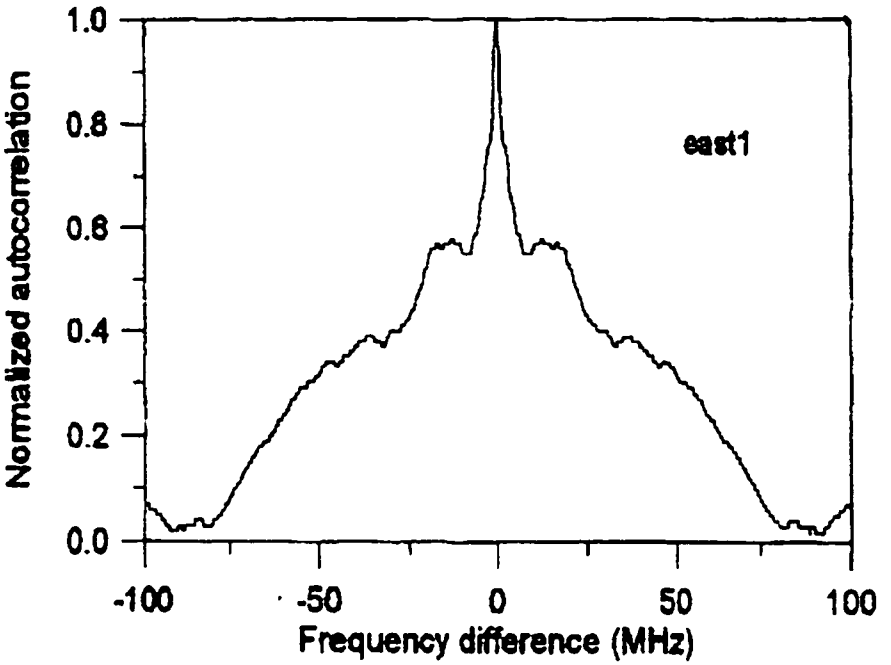

Fig. 5.15 Fourier transform of measured power delay profile [Kim96].

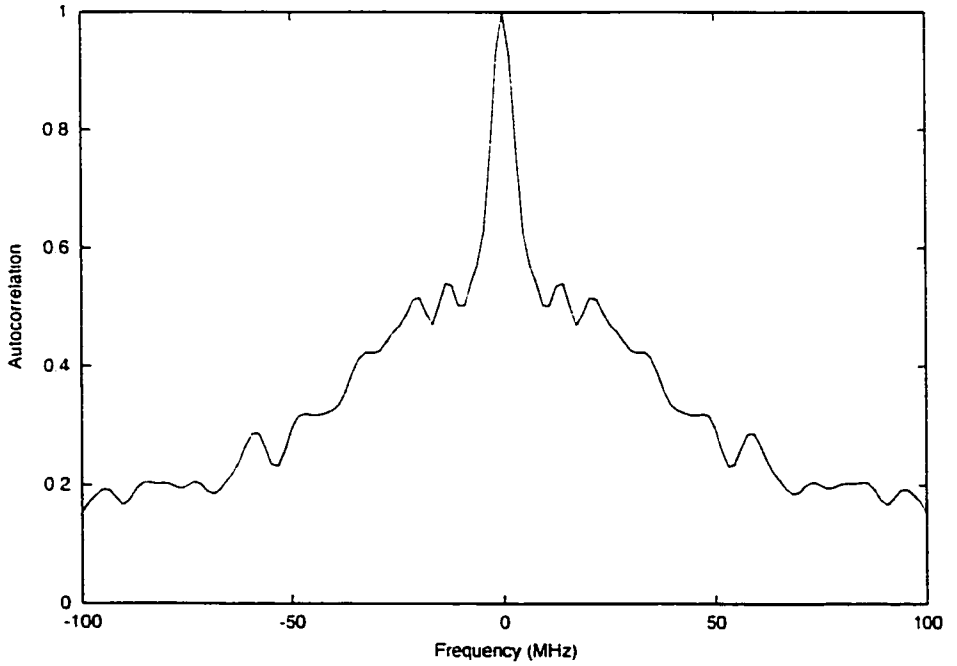

Fig. 5.16 Fourier transform of predicted power delay profile.

5.4.2 Wide band simulation using the hybrid technique

The example shown in Fig. 5.17 will be used to explain the approach of wide band simulation using the hybrid technique based on combining ray tracing and FDTD. The FDTD computation domain is enclosed in the box ABCD. First, the ray tracing method described in the previous section is used to send out the probing Gaussian pulse $p(t)$ modulated on the carrier frequency of f_0=2.4 GHz from the transmitter. After ray tracing process, incident signal envelopes are found at each point along the interface between ray tracing and FDTD computation domains. Fig. 5.18 and Fig. 5.19 show two examples of incident signal envelopes at I_1 and I_2 of Fig. 5.17.

These incident signal envelopes $x_{inc}(t)$ are then modulated on the carrier frequency f_0, i.e. the incident field can be written as $x_{inc}(n\Delta t)cos(nk_0c\Delta t)$ at each time step $n\Delta t$ of FDTD computation, and propagated into the area enclosed in ABCD by FDTD propagator. The time increment in the incident signal envelope, Δt_{inc}, in Fig. 5.18 or Fig. 5.19 is inversely proportional to the ray tracing simulation bandwidth $N\Delta f$, i.e. $\Delta t_{inc}=1/N\Delta f$. Δt_{inc} is usually much larger than the time increment Δt in FDTD computation. Therefore, incident field at $t=n\Delta t$, where $m\Delta t_{inc}<n\Delta t<(m+1)\Delta t_{inc}$ (m and n are integers), is decided by interpolation. The advantage is that the amount of memory required to store the incident wave envelope is largely reduced.

The FDTD computation does not start at t=0 ns time delay. The program detects the first perceptible pulse from all incident signals. For example, in Fig. 5.18 and Fig. 5.19, the first pulse arrives at 19 ns. Therefore FDTD computation starts at t=19 ns.

The resulting signal envelope at location R in Fig. 5.17 is shown in Fig. 5.20. The pulse-width parameter w of the probing Gaussian pulse $p(t)$ is 0.6 ns. The pulse peak power has been normalized to the peak power of the first perceptible pulse. For comparison, the simulation result by ray tracing is shown in Fig. 5.21. For the simple structure in Fig. 5.17, a very good agreement between the results by the two methods is observed.

Then the receiver R is moved two wavelengths in the x direction and the power delay profile predicted by the hybrid technique is shown in Fig. 5.22, which is quite similar to the curve in Fig. 5.20. However, there are still a few pulses shown large change in signal strength, e.g. the third pulse in Fig. 5.22 is much weaker in Fig. 5.20. Power delay profiles shown in Fig. 5. 23 and Fig. 5.24 are at the same locations as Fig. 5.20 and Fig. 5.22, respectively, except that the probing pulse width is 3 ns. The variation in the amplitude of the individual peaks is even more severe, especially after t=30 ns. The observation agrees with the measurement and simulation results in the building shown in Fig. 5.12, as analyzed in section 5.4.1. It can be explained as follows. From equation (5.1), the received signal envelope can be written as [Kim96]

$$|x(t)| = \left\{ \sum_k \sum_l \alpha_k \alpha_l \, p(t-\tau_k) p(t-\tau_l) e^{j(\theta_k - \theta_l - \omega\tau_k + \omega\tau_l)} \right\}^{1/2} \tag{5.5}$$

If no two pulses overlap in time,

$$|x(t)| = \sum_k \alpha_k \, p(t-\tau_k) \tag{5.6}$$

Under the assumption of nonoverlapping pulses, $|x(t)|$ will display only small time shifts as the receiver is moved on the order of a wavelength. However, if the pulses overlap, the phase change in (5.5) will cause the signal amplitude to vary. Since the pulse response exhibits large change in the amplitude of the individual peaks as the receiver position is changed, the conclusion is that many individual multipath components contributions overlap in time for the very short 3 ns, or even 0.6 ns.

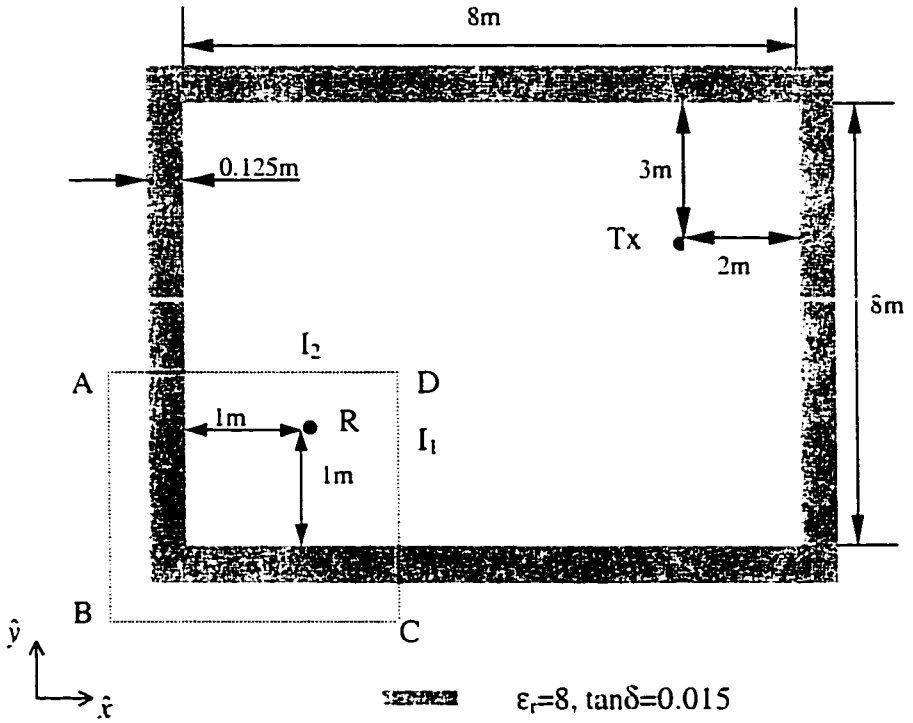

Fig. 5.17 An indoor environment for wide band simulation using the hybrid technique. The interested area is enclosed in ABCD and studied by FDTD.

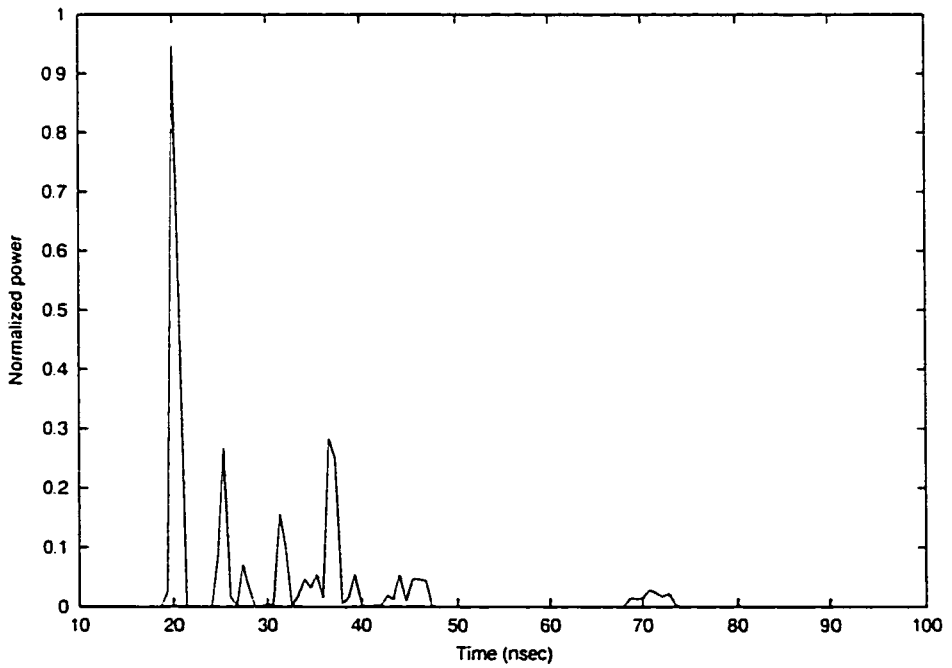

Fig. 5.18 Incident signal at I_1 along the interface between ray tracing and FDTD computation domains.

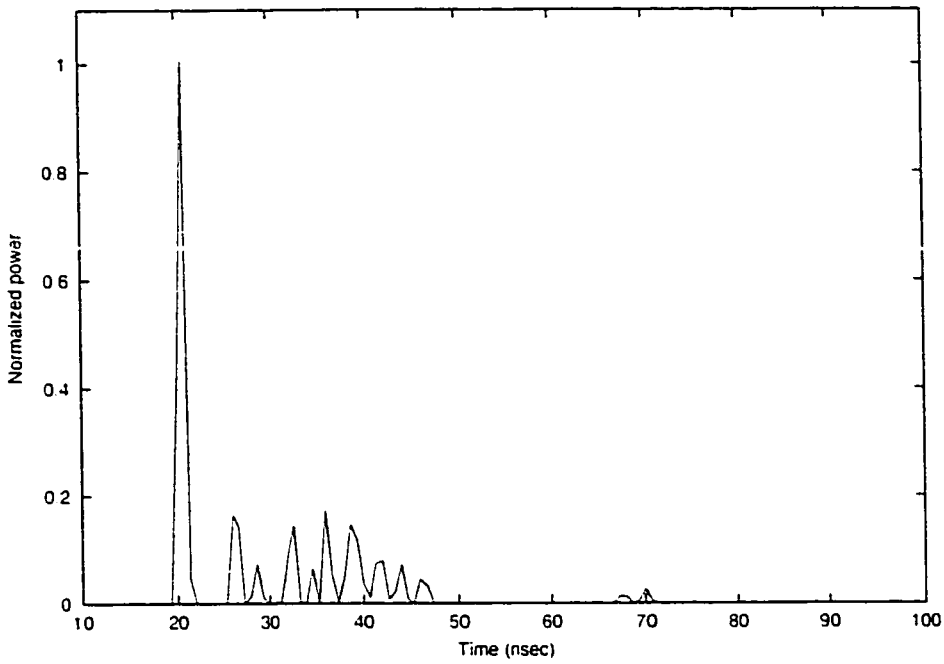

Fig. 5.19 Incident signal at I_2 along the interface between ray tracing and FDTD computation domains.

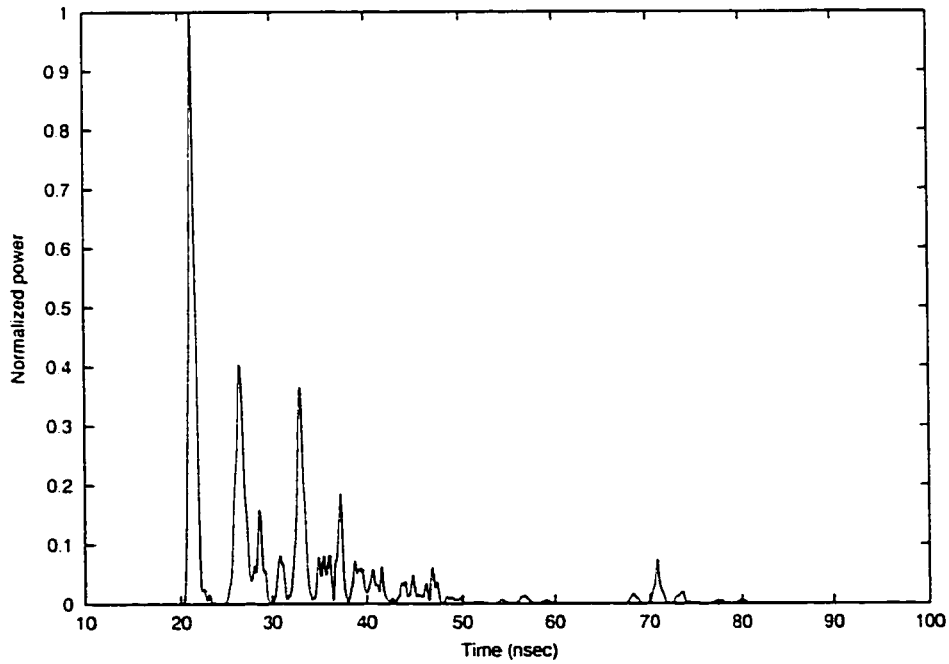

Fig. 5.20 Power delay profile at location *R* in Fig. 5. 17 calculated by the hybrid method.

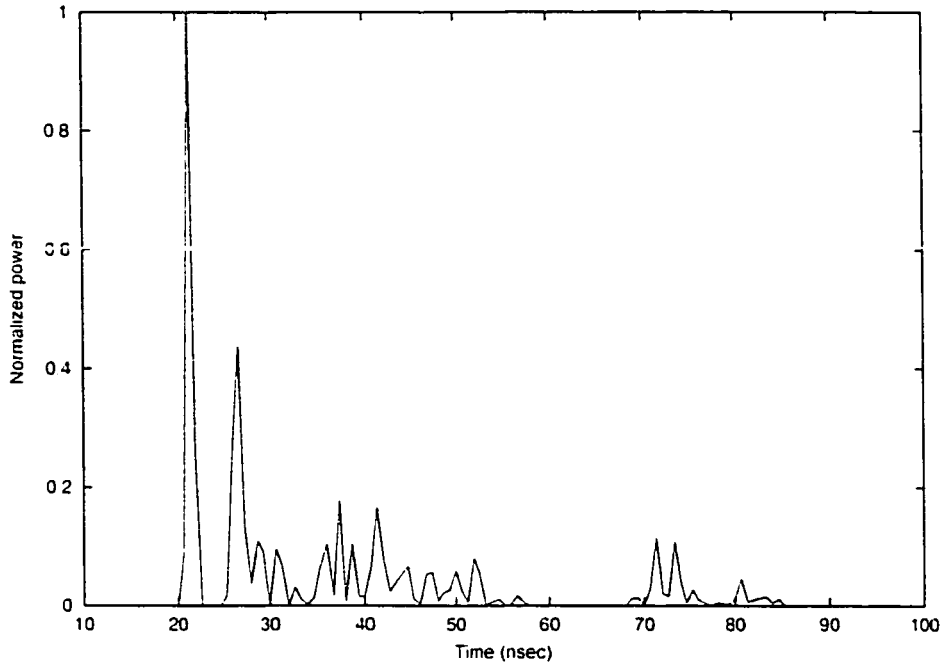

Fig. 5.21 Power delay profile at location *R* in Fig. 5. 17 calculated by ray tracing method.

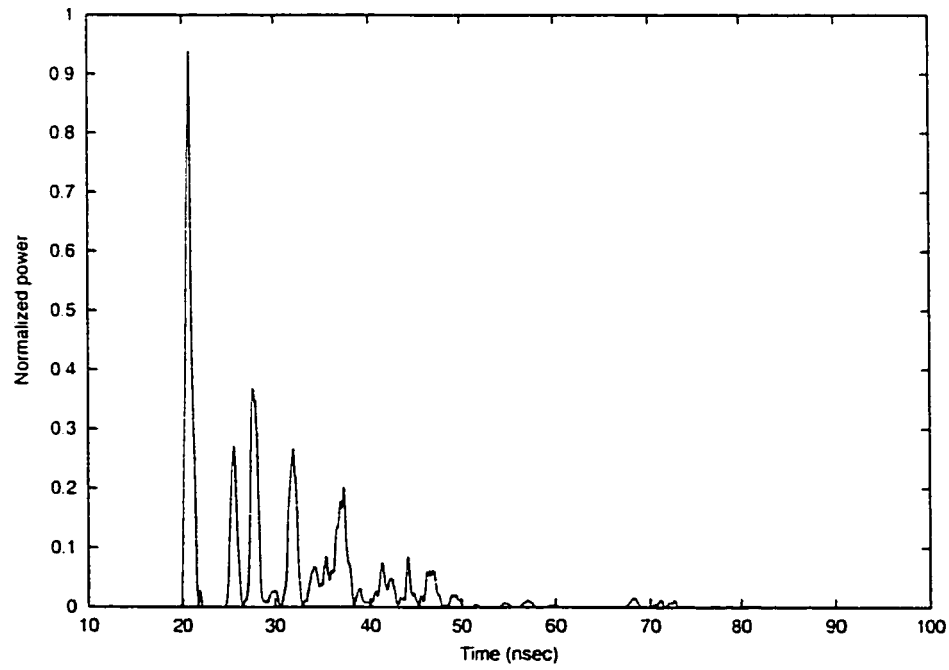

Fig. 5.22 Power delay profile at two wavelengths from location *R* in Fig. 5. 17 calculated by the hybrid method.

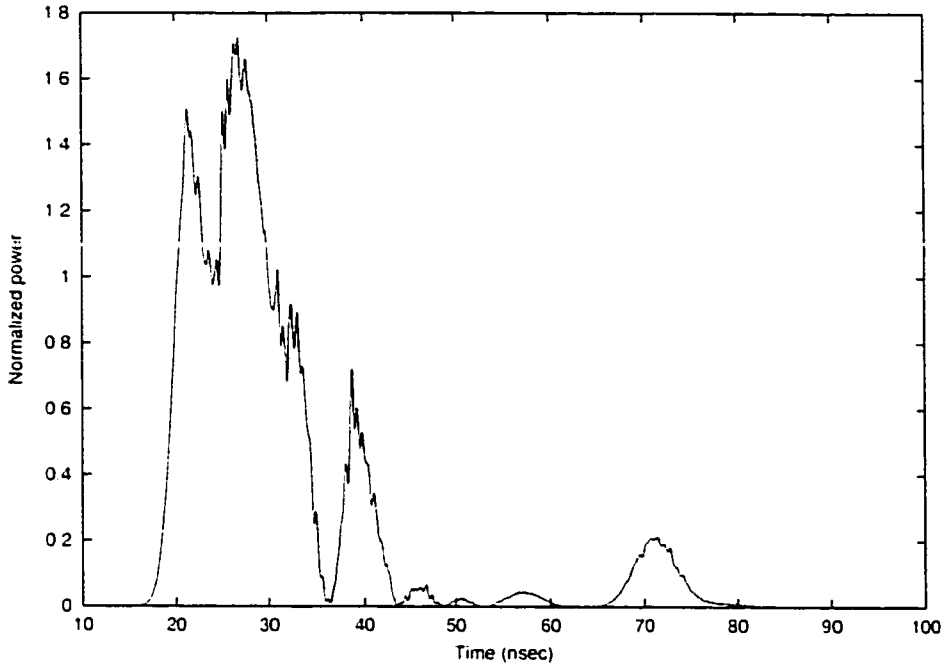

Fig. 5.23 Power delay profile at location *R* in Fig. 5. 17 when probing pulse width is 3 ns.

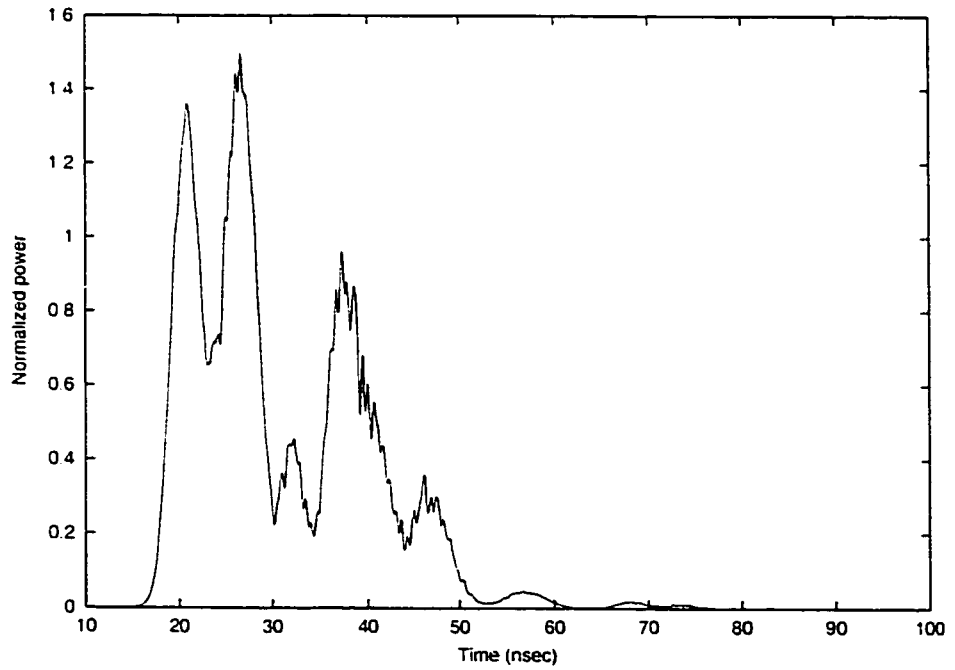

Fig. 5.24 Power delay profile at two wavelengths from location *R* when probing pulse width is 3 ns.

5.5 Summary

In this chapter we demonstrate the application of the developed deterministic models for analyzing small-scale fading effects created by multipath: fading in signal strength, Doppler spread and time dispersion.

Once field distribution in the interested local area has been found through the developed channel modeling techniques, probability distribution of field strength can obtained by statistical analysis. Performance of frequency, space and polarization diversity systems are then studied from statistical properties of radio wave propagation between a mobile and a base station.

From field distributions in the interested areas, the temporal variation caused by human-induced motion of the communication equipment can also be simulated, which leads to the detection of Doppler spread.

Next, impulse response of indoor radio channel is studies and power delay profile of received signal is obtained through wide band simulation using the developed deterministic models. After the power delay profile is correctly predicted, delay spread and coherence bandwidth are obtained.

To validate the simulation techniques, results have been compared with measurements reported by different researchers. From comparison between simulations and measurements, we can see that results by the channel models give insight into measurement observations and characteristics of the complicated indoor radio channel.

Chapter 6

Conclusions

In conclusion, the thesis's objective of constructing a reliable site-specific indoor radio channel model has been achieved through the development of the three-dimensional ray tracing algorithm and the proposed hybrid technique of combining ray tracing and FDTD methods.

The developed channel model provides solutions to both relatively simple environments and complicated structures encountered in indoor communication environment where no asymptotic solution is available. Where applicable, the developed channel model has been validated by comparing simulation results with measurement and with results from full wave simulations. Its accuracy, efficiency and flexibility have been demonstrated in this thesis. The model can generate very accurate and realistic simulated environment for predicting relevant performance and "quality-of-service" parameters for various system architectures.

Understandings of radio propagation in the complicated indoor environment obtained through the analysis in this thesis contribute to the growing area of research of indoor radio channel.

The major contributions of the thesis will be highlighted in the next section, followed by an outline of suggested directions for future work.

6.1 Summary of Contributions

A deterministic model with full propagation parameters for indoor radio propagation simulation has been developed in this thesis.

First, a refined ray tracing model has been developed. Reflection coefficients and transmission coefficients are given for TE wave incidence and TM wave incidence upon lossy dielectric slabs. Modified UTD is used for treatment of non-PEC wedge diffraction. Its accuracy and validity have been demonstrated through numerical experiments. Use of complex electric field vectors facilitates the incorporation of polarization characteristics and antenna effects. Measurements have been carried out in typical residential indoor communication environments. Path loss between a transmitter and receivers has been predicted with standard deviation of less than 5 dB over 60 locations in two different buildings.

Based on geometrical optics and augmented by modified UTD, the ray tracing algorithm's major drawback is that it can not correctly predict the scattered field by structures with complex discontinuities with characteristic dimension comparable to wavelength or smaller. Although such structures can be treated using FDTD, its high demand on computational resources prevents it from being applied to the whole communication environment. The problem is solved through the proposed hybrid technique that combines ray tracing method with FDTD method. The novel method uses ray tracing to analyze wide open areas and FDTD to treat areas close to complex discontinuities, where ray based solutions are not sufficiently accurate. Within the FDTD computation domain, the propagation characteristics are obtained from the spatial and temporal field distributions.

The proposed hybrid method enables the study of effects of generic indoor structural features, furniture, inhomogeneity inside walls, and any objects that may have significant effect on signal coverage and statistics inside buildings. Signal intensity and phase at all points can be obtained in the FDTD computation domain, which provides information of both long-term shadowing effect and short-term fading effect. Therefore, besides path loss caused by the structure studied, probability distributions of the field envelope can be derived, which is needed for reliable design of radio communication system. Numerical results show that while there are cases where predictions of electric field distribution obtained by ray tracing has accuracy comparable to those by the hybrid technique, there are situations that ray tracing results are erroneous and much improved accuracy is achieved through the hybrid method.

Furthermore, the thesis provides solution to the problem of outdoor-indoor signal coupling in the presence of inhomogeneous walls by using the ray tracing — FDTD — ray tracing approach. The method makes it possible to study the effect of inhomogeneity inside walls more accurately without adding much to computational complexity. Reduction in computation time is even more significant when the incident wave can be approximated to be plane wave and the wall structure is periodic. Numerical results have proven that significant amount of power can be scattered from walls made of concrete blocks in non-specular directions because of the periodic structure created by the web and void design of individual blocks inside the wall. In the cases when the specular signal is blocked by metallic structures, e.g. elevator shaft, metal wall, metal furniture, etc., the predicted signal intensities obtained by the ray tracing method are in average 11~18 dB less than those obtained by the proposed method. The reason lies in the fact that diffracted paths resulting from non-specular signals carry significant power to locations that might otherwise not be covered. Such effects can not be predicted by ray tracing method.

The ability of the developed method to analyze fading in signal strength, Doppler spread and time dispersion caused by multipath has also been demonstrated in this thesis,

which represents the first attempt to use site-specific models for simulation of small-scale fading effects.

From statistical analysis of the spatial field distributions in the interested local area, performance of different diversity techniques has been evaluated. We have shown that at 900 MHz in indoor environment, notable diversity gains can be obtained when signals are received by two antennas separated by $1/4\lambda$, or when the two signals are carried on two frequencies separated by more than 5 MHz, or by using polarization diversity antennas. These conclusions agree with reported experimental results. With given antenna patterns, we can evaluate performance of different designs of polarization diversity antennas.

The known spatial field distributions also facilitate the simulation of temporal variation in the received signal caused by motion of the communication equipment in the interested local area and the acquisition of Doppler spread.

While Doppler spread describes the time varying nature of the channel, delay spread and coherence bandwidth are parameters which describe the time dispersive nature of the radio channel in a local area. These channel parameters are obtained from the power delay profile through wide band simulation of the indoor radio channel. The approaches of wide band simulation using both ray tracing and the hybrid technique are presented in this thesis.

Besides improved accuracy and robustness, the hybrid method has the advantage of significant reduction of computation time compared to ray tracing method for the application of simulation of small-scale fading effects. The reason lies in the fact that in the hybrid method, the whole interested area is treated as one object and field distribution within the area is obtained by FDTD. However, if we only use ray tracing, any point within the area, which could be thousands in total, needs to be treated as one object and tested if ray intersection has occurred.

6.2 Future Research Directions

Suggestions on possible future research are summarized as follows.

First, in the ray tracing part, our method of defining objects is sufficient to make the ray tracing process efficient and to include as many as possible objects in the residential indoor environment. If the situation is much more complicated with much larger area, more efficient ray tracing acceleration techniques will be required to reduce CPU times and memory requirement. There are limited reports on application of ray tracing acceleration techniques in simulation of indoor radio wave propagation [Feu93] [Per96] [Mck91], and some of the reported methods have restricted application. Furthermore, each object in the building was defined manually, which is tedious and time consuming. Therefore, it is desirable to have software that can incorporate accurate site-specific building information into the propagation prediction tool.

The hybrid technique based on combing ray tracing and FDTD methods presented in this thesis has the ability to simulate two-dimensional structures. Extension of the hybrid method to three dimensions is straightforward, although the computational complexity will increase.

In the FDTD analysis part, more work needs to be done to reduce computation time and to improve accuracy of the numerical solution, such as employing other type of mesh, rather than the traditional rectangular mesh to reduce the mesh density. Also, alternative boundary conditions may be applied to reduce reflection from the boundaries and thereby increase the accuracy of computation.

In addition, exact building material properties are unknown and approximate values were assumed in simulations. More accurate characterization of these material properties will enhance the accuracy of propagation prediction. Until recently [Dal99][Hon94] [Lan96], little emphasis has been given to characterizing reflection and transmission

properties of building materials. The hybrid technique can be used as a tool to analyze reflection/transmission property by/through objects. Through comparison with measurement, material parameters, such as dielectric constant, can be extracted from simulation results. Furthermore, by using the developed technique to treat typical building materials and wall structures, database can be built for use by communication system designers in predicting system performance.

Bibliography

[Bal89] C. A. Balanis, *Advanced Engineering Electromagnetics*, John Wiley & Sons, Inc., 1989.

[Bha95] A. K. Bhattacharyya, *High-Frequency Electromagnetic Techniques: Recent Advances and Applications*, John Wiley & Sons, Inc., NY, 1995.

[Bur83] W. D. Burnside, and K. W. Burngener, "High frequency scattering by a thin lossless dielectric slab", *IEEE Trans. on Antennas and Propagation*, Vol. AP-31, No. 1, pp. 104-110, Jan. 1983.

[Cha91] C. H. Chan, S. H. Lou, L. Tsang, and J. A. Kong, "Electromagnetic scattering of waves by random rough surface: a finite-difference-time-domain approach", *Microwave and Optical Technology Letters*, Vol. 4, No. 9, pp. 355-359, 1991.

[Che97] S. Chen, and S. Jeng, "An SBR/image approach for radio wave propagation in indoor environments with metallic furniture", *IEEE Trans. on Antennas and Propagation*, Vol. 45, No. 1, pp. 98-106, Jan. 1997.

[Chu91] S. T. Chu, W. P. Huang, and S. K. Chaudhuri, "Simulation and analysis of waveguide based optical integrated circuits", *Computer Physics Communications*, Vol. 68, No. 1-3, pp. 451-484, Nov. 1991.

[Dal99] R. Dalke, C. L. Holloway and P. McKenna, "Reflection and transmission properties of reinforced concrete walls", *IEEE Antennas and Propagation Society International Symposium*, Orlando, FL, Vol. 3, pp. 1502-1505, July 1999.

[Feu93] M. J. Feuerstein, and T. S. Rappaport, *Wireless Personal Communications*, Kluwer Academic Publishers, 1993.

[Gla89] A. S. Glassner, *An Introduction to Ray Tracing*, Academic Press, 1989.

[Has93] H. Hashemi, "The indoor radio propagation channel", *Proceedings of the IEEE*, Vol. 81, No. 7, pp. 943-968, July 1993.

[Hip54] A. R. Von Hippel, Ed., *Dielectric Materials and Applications*, Cambridge, MA: MIT Press, 1954.

[Ho93] C. M. P. Ho, and T. S. Rappaport, "Wireless channel prediction in a modern office building using an image-based ray tracing method", *Proceedings of IEEE GLOBECOM '93*, Houston, TX, Vol. 2, pp. 1247-1251, Nov. 1993.

[Hon94] W. Honcharenko, and H. L. Bertoni, "Transmission and reflection characteristics at concrete block walls in the UHF bands proposed for future PCS", *IEEE Trans. on Antennas and Propagation*, Vol. 42, No. 2, pp. 232-239, Feb. 1994.

[Hor86] J. Horikoshi, K. Tanaka, and T. Morinaga, "1.2 GHz band wave propagation measurements in concrete building for indoor radio communications", *IEEE Trans. on Vehicular Technology*, Vol. VT-35, No. 4, pp. 146-152, Nov. 1986.

[How90] S. J. Howard, and K. Pahlavan, "Doppler spread measurements of indoor radio channel", *Electronics Letters*, Vol. 26, No. 2, pp. 107-108, Jan. 1990.

[Kel62] J. B. Keller, "Geometrical theory of diffraction", *Journal of the Optical Society of America*, Vol. 52, pp. 116-130, 1962.

[Kim96] S. Kim, H. L. Bertoni, and M. Stern, "Pulse propagation characteristics at 2.4 GHz inside buildings", *IEEE Trans. on Vehicular Technology*, Vol. 45, No. 3, pp. 579-592, Aug. 1996.

[Kou74] R. G. Kouyoumjian and P. H. Pathak, "A uniform geometrical theory of diffraction for an edge in a perfectly conducting surface", *Proceedings of the IEEE*, Vol. 62, No. 11, pp. 1448-1461, 1974.

[Lan96] O. Landron, M. L. Feuerstein, and T. S. Rappaport, "A comparison of theoretical and empirical reflection coefficients for typical exterior wall surfaces in a mobile radio

environment", *IEEE Trans. on Antennas and Propagation*, Vol. 44, No. 3, pp. 341-351, Jan. 1996.

[Lee98] J. W. H. Lee and A. K. Y. Lai, "FDTD analysis of indoor radio propagation", *IEEE Antennas and Propagation Society International Symposium*, Atlanta, GA, Vol. 3, pp. 1664-1667, June 1998.

[Lem91] J. Lemieux, M. S. El-Tanany, and H. M. Hafez, "Experimental evaluation of space/frequency/polarization diversity in the indoor wireless channel", *IEEE Trans. on Vehicular Technology*, Vol. 40, No. 3, pp. 569-574, Aug. 1991.

[Lue84] R. J. Luebbers, "Finite conductivity uniform GTD versus knife edge diffraction in prediction of propagation path loss", *IEEE Trans. on Antennas and Propagation*, Vol. AP-32, No. 1, pp. 70-76, Jan. 1984.

[McK91] J. W. McKown, and R. L. Hamilton, Jr., "Ray tracing as a design tool for radio networks", *IEEE Network Magazine*, Vol. 5, No. 6, pp. 27-30, Nov. 1991.

[Mur81] G. Mur, "Absorbing boundary conditions for the finite-difference approximation of the time-domain electromagnetic field equations", *IEEE Trans. on Electromagnetic Compatibility*, Vol. EMC-23, No. 4, pp. 377-382, Nov. 1981.

[Pah89] K. Pahlavan, and S. J. Howard, "Frequency domain measurements of indoor radio channels", *Electronic letters*, Vol. 25, pp. 1645-1647, 1989.

[Pah95] K. Pahlavan, and A. H. Levesque, *Wireless Information Networks*, Wiley Series in Telecommunications and Signal Processing, John Wiley & Sons, Inc., 1995.

[Par69] D. T. Paris, and F. K. Hurd, *Basic Electromagnetic Theory*, McGraw-Hill Physical and Quantum Electronics Series, MaGraw-Hill Book, Inc., 1969.

[Per96] J. Perez, L. Velarde, J. Gutierrez, and M. F. Catedra, "Efficient ray tracing algorithms for planning of picocellular systems in urban and indoor environments", *IEEE*

Antenna and Propagation Society International Symposium 1996, Vol. 1, pp. 21-26, Baltimore, MD, July 1996.

[Rap89] T. S. Rappaport, "Characterization of UHF multipath radio channel in factory buildings", *IEEE Trans. on Antennas and Propagation*, Vol. 37, No. 8, pp. 1058-1069, Aug. 1989.

[Rap96] T. S. Rappaport, *Wireless Communications: Principles and Practice*, Prentice Hall, 1996.

[Rod98] J. A. Roden, S. D. Gedney, M. P. Kesler, J. G. Maloney, and P. H. Harms, "Time-domain analysis of periodic structures at oblique incidence: orthogonal and nonorthogonal FDTD implementations", *IEEE Trans. on Microwave Theory and Techniques*, Vol. 46, No. 4, pp. 420-427, Apr. 1998.

[Rou97] J. F. Rouviere, N. Douchin and P. F. Combes, "Improvement of the UTD formulation for diffraction of an electromagnetic wave by a dielectric wedge", *Electronics Letters*, Vol. 33, No. 5, pp. 373-375, Feb. 1997.

[Ruc70] G. T. Ruck, D. E. Barrick, W. D. Stuart, and C. K. Krichbaum, *Radar Cross Section Handbook*, Plenum Press, NY, 1970.

[Rus91] A. J. Rustako, Jr., N. Amitay, G. J. Owens, and R. S. Roman, "Radio propagation at microwave frequencies for line-of-sight microcellular mobile and personal communications", *IEEE Trans. on Vehicular Technology*, Vol. 40, No. 1, Feb. 1991.

[Sch92] K. R. Schaubach, N. J. Davis, IV, and T. S. Rappaport, "A ray tracing method for predicting path loss and delay spread in microcellular environments", *42nd IEEE Vehicular Technology Conference*, Denver, pp. 932-935, May 1992.

[Sei94] S. Y. Seidel, and T. S. Rappaport, "Site-specific propagation prediction for wireless in-building personal communication system design", *IEEE Trans. on Vehicular Technology*, Vol. 43, No. 4, pp. 879-891, Nov. 1994.

[Str97] S. Stratis, V. Anantha, and A. Taflove, "Numerical calculation of diffraction coefficients of generic conduction and dielectric wedges using FDTD", *IEEE Trans. on Antennas and Propagation*, Vol. 45, No. 10, pp. 1525-1529, Oct. 1997.

[Stu81] W. L. Stutzman, and G. A. Thiele, *Antenna Theory and Design*, John Wiley & Sons, Inc., 1981.

[Taf95] A. Taflove, *Computational Electrodynamics: The Finite-Difference Time-Domain Method*, Artech House, Inc., 1995.

[Tar97] J. H. Tarng, W. R. Chang, and B. J. Hsu, "Three-dimensional modeling of 900-MHz and 2.44-GHz radio propagation in corridors", *IEEE Trans. on Vehicular Technology*, Vol. 46, No. 2, pp. 519-527, May 1997.

[Tay69] C. D. Taylor, D. H. Lam, and T. H. Shumpert, "Electromagnetic pulse scattering in time-varying inhomogeneous media", *IEEE Trans. on Antenna and Propagation*, Vol. 17, pp. 585, 1969.

[Tod92] S. R. Todd, M. S. El-Tanany, and S. A. Mahmoud, "Space and frequency diversity measurements of 1.7 GHz indoor radio channel using a four-branch receiver", *IEEE Trans. on Vehicular Technology*, Vol. 41, No. 3, pp. 312-320, Aug. 1992.

[Tur72] G. L. Turin, et al., "A statistical modal of urban multipath propagation", *IEEE Trans. on Vehicular Technology*, Vol. VT-21, pp. 1-9, Feb. 1972.

[Uma82] K. R. Umashankar, and A. Taflove, "A novel method to analyze electromagnetic scattering of complex objects", *IEEE Trans. on Electromagnetic Compatibility*, Vol. 24, pp. 397, 1982.

[Vey93] M. E. Veysoglu, R. T. Shin and J. A. Kong, "A finite-difference time-domain analysis of wave scattering from periodic surfaces: oblique incidence case", *Journal of Electromagnetic Waves and Applications*, Vol. 7, No. 12, pp. 1595-1607, 1993.

[Wan98a] Y. Wang, S. Safavi-Naeini, and S. K. Chaudhuri, "A combined ray tracing and FDTD method for modeling indoor radio wave propagation", *IEEE Antennas and Propagation Society International Symposium*, Atlanta, GA, Vol. 3, pp. 1668-1671, June 1998.

[Wan98b] Y. Wang, S. Safavi-Naeini, and S. K. Chaudhuri, "Site-specific modeling of indoor radio wave propagation", *ANTEM'98 - Symposium on Antenna Technology and Applied Electromagnetics*, Ottawa, ON, pp. 17-20, Aug. 1998.

[Wan99] Y. Wang, S. Safavi-Naeini, and S. K. Chaudhuri, "Comparative study of lossy dielectric wedge diffraction for radio wave propagation modeling using UTD and FDTD", *IEEE Antennas and Propagation Society International Symposium*, Orlando, FL, Vol. 4, pp. 2826-2829, July 1999.

[Wan00a] Y. Wang, S. Safavi-Naeini, and S. K. Chaudhuri, "A hybrid technique based on combining ray tracing and FDTD methods for site-specific modeling of indoor radio wave propagation", *IEEE Trans. on Antennas and Propagation*, Vol. 48, pp. 743-754, May 2000.

[Wan00b] Y. Wang, S. K. Chaudhuri, and S. Safavi-Naeini, "A novel method of studying wave penetration through inhomogeneous walls using FDTD and ray tracing", *IEEE Antennas and Propagation Society International Symposium*, Salt Lake City, UT, Vol. 2, pp. 1126-1129, July 2000.

[Wen79] M. J. Wenninger, *Spherical Models*, New York: Cambridge Univ. Press, 1979.

[Yan93] G. Yang, K. Pahlavan, and J. F. Lee, "A 3D propagation model with polarization characteristics in indoor radio channels", *Proceedings of IEEE GLOBECOM '93*, Houston, TX, Vol. 2, pp. 1252-1256, Nov. 1993.

[Yan98] C. Yang, B. Wu, and C. Ko, "A ray-tracing method for modeling indoor wave propagation and penetration", *IEEE Trans. on Antennas and Propagation*, Vol. 46, No. 6, pp. 907-919, June 1998.

[Yee66] K. S. Yee, " Numerical solution of initial boundary value problems involving maxwell's equations in isotropic media", *IEEE Trans. on Antennas and Propagation*, Vol. AP-14, pp. 302-307, May 1966.

[Zag91] H. Zaghloul, G. Morrison, and M. Fatouche, " Frequency response and path loss measurements of indoor channel", *Electronics Letters*, Vol. 27, No. 12, pp. 1021-1022, June 1991.

Appendix 1

Reflection and Transmission Coefficients

We will present derivation of the reflection coefficients and transmission coefficients for TE wave incidence and TM wave incidence upon lossy dielectric slabs in this section.

A.1 Perpendicular Polarization (TE wave)

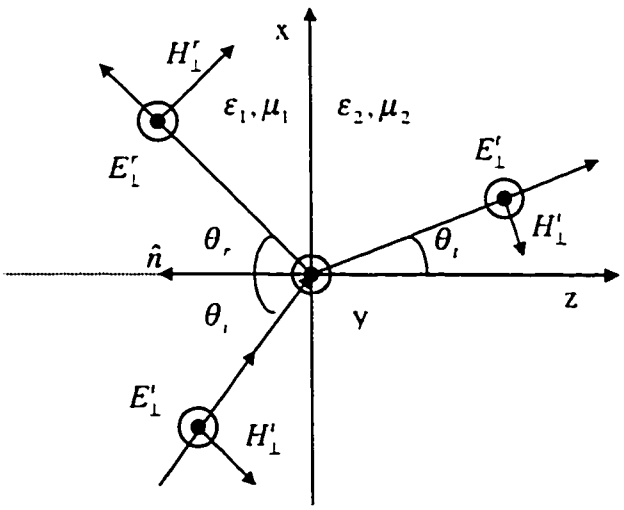

Fig. A.1 Perpendicular polarized plane wave (TE wave) incidence at an oblique angle on an interface.

The perpendicular polarized plane wave incidence at an oblique angle on an interface is shown in Fig. A.1, which is applicable to both the boundary between region 1 and region 2 (boundary 1-2) and the boundary between region 2 and region 3 (boundary 2-3)

in Fig. 2.3. Actually when the conductivity σ at region 2 is not zero, θ_2 is a complex angle.

From Snell's laws [Par69], we have $\frac{\sin\theta_2}{\sin\theta_1} = \frac{\gamma_1}{\gamma_2}$, where γ_1 and γ_2 are the propagation factors in free space and in the slab, respectively, and can be written as

$$\gamma_1 = j\beta_1 = j\omega\sqrt{\mu_0\varepsilon_0}$$

$$\gamma_2 = \alpha_2 + j\beta_2 = \omega\sqrt{\mu_0\varepsilon}\left[\left(\frac{1}{2}\left(\sqrt{1+\left(\frac{\sigma}{\omega\varepsilon}\right)^2}-1\right)\right)^{\frac{1}{2}} + j\left(\frac{1}{2}\left(\sqrt{1+\left(\frac{\sigma}{\omega\varepsilon}\right)^2}+1\right)\right)^{\frac{1}{2}}\right]$$

Therefore, we have

$$\cos\theta_2 = \sqrt{1-\sin^2\theta_2} = \sqrt{1-\left(\frac{j\beta_1}{\alpha_2+j\beta_2}\right)^2\sin^2\theta_1}$$

Electric field can be represented by $\vec{E} = \vec{E}_0 e^{-\gamma \vec{n}_0 \cdot \vec{r}}$, where $\vec{n}_0$ is a unit vector in the direction of propagation, $\vec{E}_0$ is the complex vector magnitude of $\vec{E}$ and $\vec{r}$ is the position vector. For a plane wave, the expression for $\vec{H}$ field is

$$\vec{H} = \frac{\vec{n}_0 \times \vec{E}}{\eta} e^{-\gamma \vec{n}_0 \cdot \vec{r}}$$

where η is the characteristic impedance of the medium.

Now consider the situation depicted in Fig. 2.3, at boundary 2-3, the tangential $\vec{E}$ field and $\vec{H}$ field are continuous. Therefore, we have the following equations,

$$\begin{cases} E_{2i} + E_{2r} = E_t & (E-field) \\ \dfrac{E_{2i}}{\eta_2}\cos\theta_2 - \dfrac{E_{2r}}{\eta_2}\cos\theta_2 = \dfrac{E_t\cos\theta_3}{\eta_3} & (H-field) \end{cases} \tag{A.1}$$

Similarly, boundary conditions at boundary 1-2 are expressed by

$$\begin{cases} E_{2i}e^{\varphi_2} + E_{2r}e^{-\varphi_2} = E_{1i} + E_{1r} \\ \dfrac{E_{2i}}{\eta_2}\cos\theta_2 e^{\varphi_2} - \dfrac{E_{2r}}{\eta_2}\cos\theta_2 e^{-\varphi_2} = \dfrac{E_{1i}}{\eta_1}\cos\theta_1 - \dfrac{E_{1r}}{\eta_1}\cos\theta_1 \end{cases} \tag{A.2}$$

where $\eta_1 = \eta_3 = \sqrt{\dfrac{\mu_0}{\varepsilon_0}}$, $\eta_2 = \sqrt{\dfrac{j\omega\mu_0}{\sigma + j\omega\varepsilon}}$, and $\varphi_2 = \gamma_2 d\cos\theta_2$.

According to our definition, the reflection coefficient and transmission coefficient for TE wave incidence are derived from equation (A.1) and (A.2) and can be written as

$$\begin{cases} \Gamma_\perp = \dfrac{E_{1r}}{E_{1i}} = \dfrac{(1+\dfrac{\eta_1}{\eta_2}\dfrac{\cos\theta_2}{\cos\theta_1})(1-\dfrac{\eta_2}{\eta_3}\dfrac{\cos\theta_3}{\cos\theta_2})e^{-\varphi_2} + (1-\dfrac{\eta_1}{\eta_2}\dfrac{\cos\theta_2}{\cos\theta_1})(1+\dfrac{\eta_2}{\eta_3}\dfrac{\cos\theta_3}{\cos\theta_2})e^{\varphi_2}}{(1-\dfrac{\eta_1}{\eta_2}\dfrac{\cos\theta_2}{\cos\theta_1})(1-\dfrac{\eta_2}{\eta_3}\dfrac{\cos\theta_3}{\cos\theta_2})e^{-\varphi_2} + (1+\dfrac{\eta_1}{\eta_2}\dfrac{\cos\theta_2}{\cos\theta_1})(1+\dfrac{\eta_2}{\eta_3}\dfrac{\cos\theta_3}{\cos\theta_2})e^{\varphi_2}} \\ T_\perp = \dfrac{E_t}{E_{1i}} = \dfrac{4}{(1-\dfrac{\eta_1}{\eta_2}\dfrac{\cos\theta_2}{\cos\theta_1})(1-\dfrac{\eta_2}{\eta_3}\dfrac{\cos\theta_3}{\cos\theta_2})e^{-\varphi_2} + (1+\dfrac{\eta_1}{\eta_2}\dfrac{\cos\theta_2}{\cos\theta_1})(1+\dfrac{\eta_2}{\eta_3}\dfrac{\cos\theta_3}{\cos\theta_2})e^{\varphi_2}} \end{cases} \tag{A.3}$$

A.2 Parallel Polarization (TM wave)

Similarly, the parallel polarized plane wave incidence at an oblique angle on an interface is shown in Fig. A.2, which is applicable to both boundary 1-2 and boundary 2-3.

Continuity of tangential field at the boundaries is expressed by the following equations.

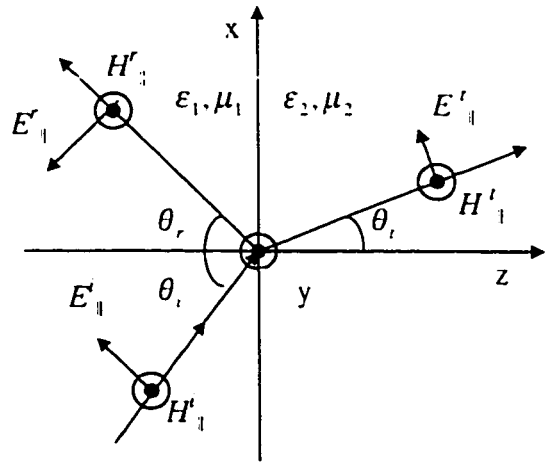

Fig. A.2 Parallel polarized plane wave (TM wave) incidence at an oblique angle on an interface.

$$\text{At Boundary 2-3: } \begin{cases} E_{2i}\cos\theta_2 - E_{2r}\cos\theta_2 = E_t\cos\theta_3 \\ \dfrac{E_{2i}}{\eta_2} + \dfrac{E_{2r}}{\eta_2} = \dfrac{E_t}{\eta_3} \end{cases} \tag{A.4}$$

$$\text{At Boundary 1-2: } \begin{cases} E_{2i}\cos\theta_2 e^{\varphi_2} - E_{2r}\cos\theta_2 e^{-\varphi_2} = E_{1i}\cos\theta_1 - E_{1r}\cos\theta_1 \\ \dfrac{E_{2i}}{\eta_2}e^{\varphi_2} + \dfrac{E_{2r}}{\eta_2}e^{-\varphi_2} = \dfrac{E_{1i}}{\eta_1} + \dfrac{E_{1r}}{\eta_1} \end{cases} \tag{A.5}$$

From equation (A.4) and (A.5), the reflection coefficient and transmission coefficient for TM wave incidence can be written as

$$\begin{cases} \Gamma_{11} = \dfrac{E_{1r}}{E_{1i}} = \dfrac{(\dfrac{\eta_2}{\eta_3} + \dfrac{\cos\theta_3}{\cos\theta_2})(\dfrac{\eta_1}{\eta_2} - \dfrac{\cos\theta_2}{\cos\theta_1})e^{\varphi_2} + (\dfrac{\eta_2}{\eta_3} - \dfrac{\cos\theta_3}{\cos\theta_2})(\dfrac{\eta_1}{\eta_2} + \dfrac{\cos\theta_2}{\cos\theta_1})e^{-\varphi_2}}{(\dfrac{\eta_2}{\eta_3} + \dfrac{\cos\theta_3}{\cos\theta_2})(\dfrac{\eta_1}{\eta_2} + \dfrac{\cos\theta_2}{\cos\theta_1})e^{\varphi_2} + (\dfrac{\eta_2}{\eta_3} - \dfrac{\cos\theta_3}{\cos\theta_2})(\dfrac{\eta_1}{\eta_2} - \dfrac{\cos\theta_2}{\cos\theta_1})e^{-\varphi_2}} \\ T_{11} = \dfrac{E_t}{E_{1i}} = \dfrac{4}{(\dfrac{\eta_2}{\eta_3} + \dfrac{\cos\theta_3}{\cos\theta_2})(\dfrac{\eta_1}{\eta_2} + \dfrac{\cos\theta_2}{\cos\theta_1})e^{\varphi_2} + (\dfrac{\eta_2}{\eta_3} - \dfrac{\cos\theta_3}{\cos\theta_2})(\dfrac{\eta_1}{\eta_2} - \dfrac{\cos\theta_2}{\cos\theta_1})e^{-\varphi_2}} \end{cases} \quad \text{(A.6)}$$